RESEARCH ARTICLE SUMMARY

NEUROSCIENCE

Head-direction cells as a neural compass in bats navigating outdoors on a remote oceanic island

Shaked Palgi†, Saikat Ray†, Shir R. Maimon†, Yuval Waserman, Liron Ben-Ari, Tamir Eliav, Avishag Tuval, Chen Cohen, Julius D. Keyyu, Abdalla I. Ali, Henrik Mouritsen, Liora Las*, Nachum Ulanovsky*

Full article and list of author affiliations: https://doi.org/10.1126/science.adw6202

INTRODUCTION: Animals and humans live in large and rich environments and need to navigate to find their way. Navigation behavior outdoors has been studied extensively by ecologists and ethologists. By contrast, the neural mechanisms of navigation have almost exclusively been studied indoors, in small laboratory settings, which are much smaller and contain poorer sensory information than real-world outdoor environments. This leaves a major gap in our understanding of the neural basis of navigation: How does the brain's "navigation circuit" operate in real-world conditions? In this study, we focused on head-direction cells—neurons that change their activity depending on an animal's orientation and are often called "neural compasses." These neurons are well characterized in small environments but had not previously been studied in natural environments outdoors.

RATIONALE: We set out to study head-direction cells in the wild by releasing Egyptian fruit bats to fly freely and navigate unconstrained on a small island near Zanzibar in East Africa. We developed a miniaturized wireless recording device—a "neural logger"—that allowed tracking of the bats' position and direction using a precise GPS and simultaneously recording the activity of multiple individual neurons. We conducted neural recordings in brain regions that are well known to contain head-direction cells. We sought to differentiate between two competing hypotheses: the "mosaic hypothesis," which predicts that each neuron will show different directional tuning in different areas of the island, depending on local sensory cues, and the "global compass hypothesis," which predicts that each neuron will exhibit the same directional tuning across the entire geographical extent of the island. Additionally, manipulating distant visual cues in laboratory experiments causes head-direction tuning to rotate, leading to a potential conundrum: Do head-direction cells rotate their tuning outdoors upon movement of the Moon and stars, which are the most prominent distant visual cues outdoors? If so, then these neurons would form a highly unreliable neural compass for real-world navigation.

RESULTS: We discovered head-direction cells in bats navigating on the island, which had similar functional properties to classical indoor head-direction cells. These neurons maintained their directional tuning over a large geographical scale, consistent with the global compass hypothesis. In contrast, there was no compelling evidence for the mosaic hypothesis. We further showed that head-direction cells remained stable both when the Moon was below the horizon and when the Moon and stars were occluded by clouds, which implies that the geographically stable tuning did not depend on the availability of these distant visual cues. We also ruled out a magnetic field–based origin of the neural compass. Finally, we found that the head-direction code stabilized slowly over several nights, suggesting a process during which bats gradually learned the layout of their environment, including the landmarks and geometry of the island.

CONCLUSION: Our results suggest that head-direction cells represent direction stably across geographical scales and irrespective of celestial dynamics and can therefore serve as the brain's neural compass. This study emphasizes the need to investigate the neural mechanisms of navigation in the wild. More generally, we call for broadening the scope of brain research toward neuroscience in the real world. □

*Corresponding author. Email: nachum.ulanovsky@weizmann.ac.il (N.U.); liora.las@weizmann.ac.il (L.L.) †These authors contributed equally to this work. **Cite this article as** S. Palgi *et al.*, *Science* **390**, eadw6202 (2025). DOI: 10.1126/science.adw6202

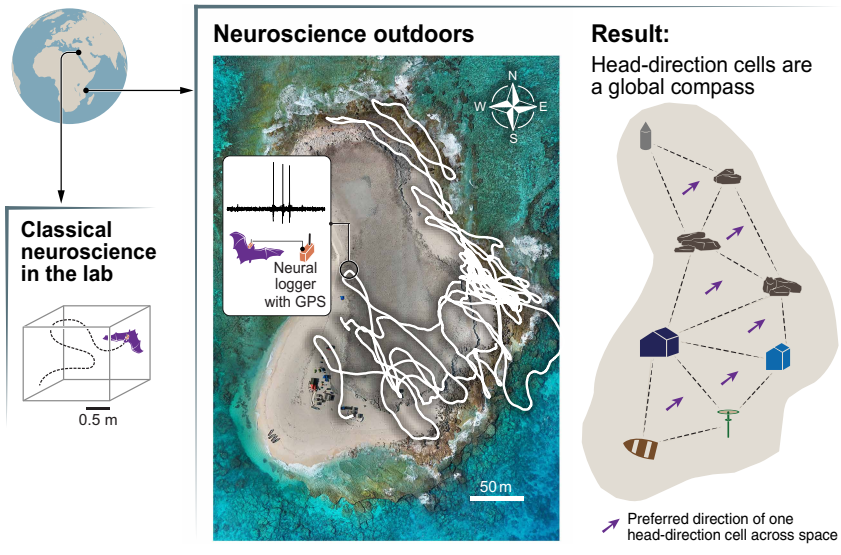

Head-direction cells recorded outdoors form a reliable neural compass for real-world navigation. We performed single-unit neural recordings in animals navigating unconstrained in the wild—in bats flying outdoors on a remote oceanic island—and discovered that head-direction cells stably encode the animals' orientation across the entire island, irrespective of the dynamics of the Moon and stars. [Illustration: Genia Brodsky; Photograph: Shaked Palgi]

NEUROSCIENCE

Head-direction cells as a neural compass in bats navigating outdoors on a remote oceanic island

Shaked Palgi[1]†, Saikat Ray[1]†, Shir R. Maimon[1]†, Yuval Waserman[1], Liron Ben-Ari[1], Tamir Eliav[1]‡, Avishag Tuval[1], Chen Cohen[1], Julius D. Keyyu[2], Abdalla I. Ali[3], Henrik Mouritsen[4], Liora Las[1]*, Nachum Ulanovsky[1]*

Animals and humans rely on their navigation skills to survive. However, spatial neurons in the brain's "navigation circuit" had not previously been studied under real-world conditions. We conducted an electrophysiological study of spatial neurons in the wild: We recorded head-direction cells from the presubiculum of bats flying unconstrained and navigating outdoors on a remote oceanic island. These neurons represented the bats' orientation stably across the island's entire geographical scale and irrespective of the dynamics of the Moon and the Milky Way. The directional tuning stabilized over several nights from the first exploration of the island. These results imply that head-direction cells can serve as a learned, reliable neural compass for real-world navigation—highlighting the power of taking neuroscience out into the wild.

Navigation is crucial for animals and humans. Historically, studies of navigation followed two very different approaches: Ethologists and ecologists tracked animals in the wild, focusing on navigational strategies and sensory mechanisms in real-world environments (*1*–*6*). Sensory mechanisms were also investigated behaviorally in laboratory settings (*7*–*9*). In parallel, neuroscientists recorded neural activity from animals navigating indoors in small laboratory enclosures and discovered place cells (*10*, *11*), grid cells (*12*, *13*), and head-direction cells (*14*–*22*)—neurons that are considered to be important for navigation. However, the assumption that the brain's navigation circuit behaves the same in the lab and in the wild is challenged by an increasing body of literature demonstrating that the use of naturalistic stimuli often yields unexpected findings about brain function (*23*). In nature, animals navigate in large open environments with multiple sets of cues, and the landmarks visible to them change as they traverse through space (*24*), which is very different from the typical laboratory setups in which navigation-related neurons are usually recorded (*25*, *26*). These neurons had never been recorded during real-world navigation outdoors, leaving a major gap in our current understanding of the neural mechanisms of navigation: Are these spatial neurons relevant to the real world? We thus studied neurons in the brain's navigation circuit during outdoor navigation—in bats flying freely on an island—focusing on the head-direction circuit.

Head-direction cells are neurons that are tuned to the animal's orientation. In laboratory experiments, these cells were shown in some cases to rotate their tuning after manipulation of the surrounding environment (*16*, *17*, *27*–*30*) and in other cases to remain stable despite such manipulation (*30*–*33*)—depending on the details of the experiment. It thus remains unknown how head-direction cells function in natural environments: Do they encode direction locally, by having a mosaic of several representations anchored to different landmarks at different locations [fig. S1, left; see also (*34*)]? Or do they remain stable and encode direction over regional or global scales, maintaining the same preferred direction across large geographical areas (fig. S1, right)?

Outdoors, some of the most prominent distal visual cues are celestial cues, such as the Sun and the Moon, which are used for navigation by many animals (*35*–*41*). However, these are not stable directional cues, because they appear, disappear, and move in the sky. How do head-direction cells deal with this instability? In laboratory experiments, head-direction tuning rotates when distal cues are rotated (*17*, *27*). On the basis of these studies, we may expect that head-direction tuning outdoors shifts with the daily movement of the celestial cues. This presents a conundrum: Can head-direction cells serve as a reliable neural compass for outdoor navigation? If not, how do animals maintain a stable representation of direction during real-world navigation?

To tackle this challenge, we developed a new recording system that combines wireless neural logging and GPS tracking and conducted single-cell neural recordings in bats flying outdoors. We asked three questions: (i) Do head-direction cells exist over geographical scales outdoors? (ii) Are they local or global compasses over such spatial scales? (iii) Are these neural compasses stable and robust to the movement of celestial cues? We recorded head-direction cells from the dorsal presubiculum of Egyptian fruit bats (*Rousettus aegyptiacus*) as the bats navigated outdoors on Latham Island, a small island near East Africa. We focused on the dorsal presubiculum because head-direction cells in this region have been studied extensively in rodents and bats (*15*, *16*, *22*, *25*). Experiments on an island allowed us to overcome two major obstacles for unconstrained neural recordings outdoors: how to recapture the bats, and how to obtain good behavioral coverage to allow reliable estimation of neuronal tuning.

Conducting single-unit neural recordings in the presubiculum of bats flying outdoors

First, we developed a miniaturized neural logger, which includes a high-precision GPS module together with additional sensors (Fig. 1A). This allowed us to combine precise localization outdoors (Fig. 1, B and C; positional localization accuracy, SD = 71 cm; directional accuracy, SD = 3.3°) with single-cell neural recordings in the bat presubiculum (Fig. 1, D and E, and fig. S2A).

We captured wild bats (n = 6) in mainland Tanzania (Fig. 1F) (*42*) and implanted them with a 16-tetrode microdrive. We then sailed with the implanted animals to Latham Island (Fig. 1, F to H; figs. S3, A and B, and S4, A to C; and Movie 1)—a barren and uninhabited remote island, ~350 m by 250 m in size—where we stayed for 3 to 4 weeks. On the island, we first accustomed the bats to the environment for a few days (inside a cage and a flight tent) and then started nightly recordings during which we released the bats one by one to fly outdoors (the bats were recaptured at the end of each session). The bats were released primarily from two platforms, where food was available (Fig. 1I and green dots in Fig. 1G) (*42*).

During the sessions, which typically lasted ~30 to 50 min (Fig. 1J, top), the bats flew fast (Fig. 1K), at an altitude of several meters (Fig. 1L), and exhibited complex trajectories (Fig. 1G and fig. S2B), allowing them to cover a large area each night (Fig. 1M and fig. S3C; median area covered per session = 5751 m^2; see fig. S5 for additional behavioral parameters). Because of occlusions from obstacles such as cliffs, boulders, and tents, the bats could see only a fraction of the island at any given moment (Fig. 1N and fig. S6). The bats performed many turns (Fig. 1O), resulting in full coverage of the azimuthal (horizontal) axis of heading direction (Fig. 1, P and Q, and fig. S2C). Head direction and heading (flight) direction were highly correlated (Fig. 1R,

[1]Department of Brain Sciences, Weizmann Institute of Science, Rehovot, Israel. [2]Tanzania Wildlife Research Institute, Arusha, Tanzania. [3]Department of Natural Sciences, The State University of Zanzibar, Zanzibar, Tanzania [4]Research Centre for Neurosensory Sciences, and Institut für Biologie und Umweltwissenschaften, Carl-von-Ossietzky Universität Oldenburg, Oldenburg, Germany. ***Corresponding author. Email: nachum.ulanovsky@weizmann.ac.il (N.U.); liora.las@weizmann.ac.il (L.L.)** †These authors contributed equally to this work. ‡Present address: Max Planck Institute for Biological Intelligence, Seewiesen, Germany.

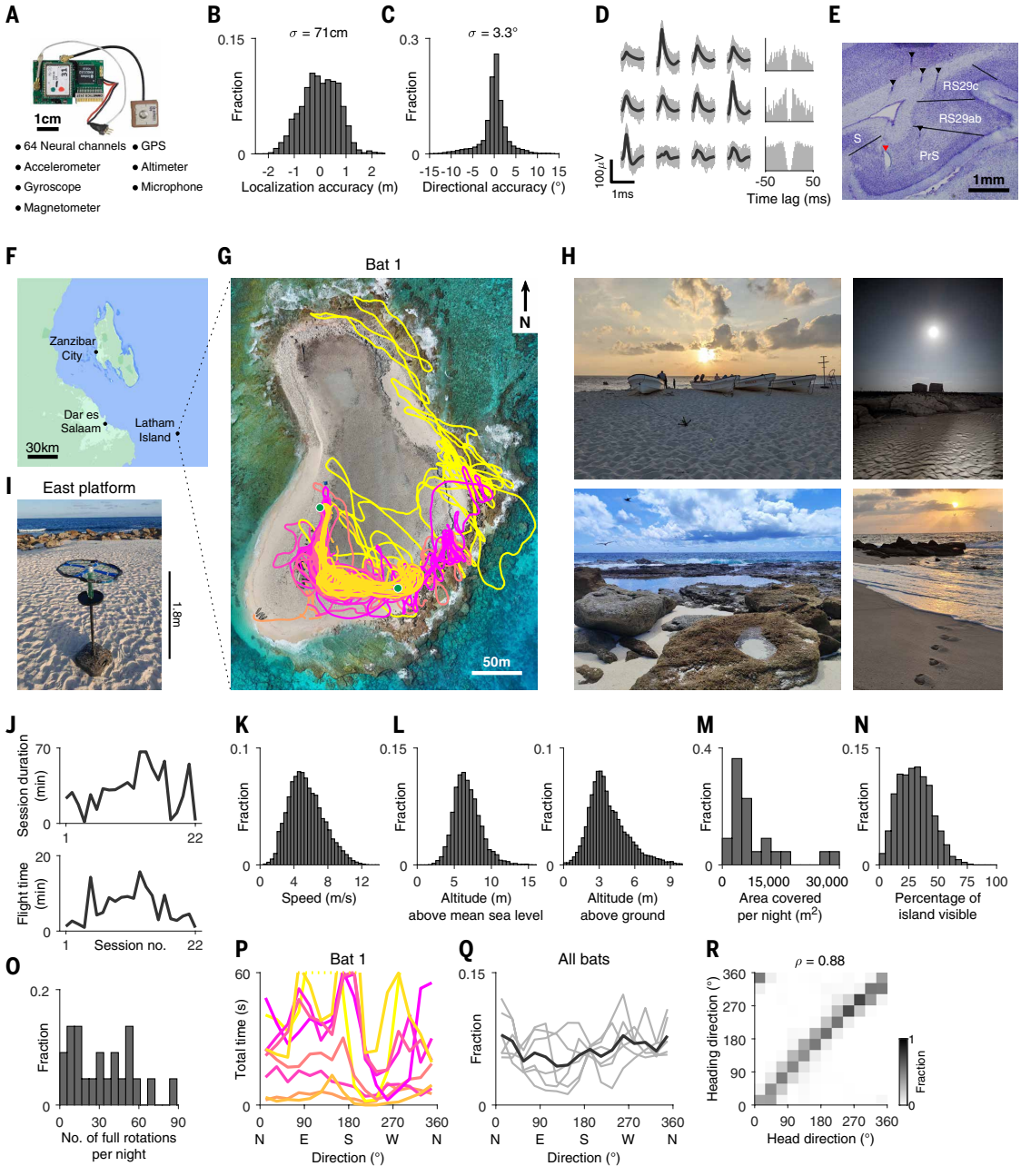

Fig. 1. Conducting single-unit neural recordings in the presubiculum of bats flying outdoors. (**A**) Photograph of the neural logger with GPS, and a list of the onboard sensors. (**B**) GPS localization accuracy, measured in a separate calibration procedure [$n = 26{,}416$ samples (*42*)]; σ, standard deviation = 71 cm. (**C**) GPS directional accuracy [same as (B)]; $\sigma = 3.3°$. (**D**) Three well-isolated neurons (rows) recorded outdoors on one tetrode. (Left) The four channels of the tetrode (columns), showing mean waveforms (black) and 100 random waveforms per neuron (gray). (Right) Spike time autocorrelations, demonstrating clear refractory periods. (**E**) Nissl-stained coronal section of bat 1, showing tetrode tracks toward the dorsal presubiculum (black arrowheads) and an electrolytic lesion in the presubiculum (red arrowhead). PrS, presubiculum; RS, retrosplenial cortex; S, subiculum. Anatomical delineations are based on (*73*). (**F**) Shoreline of Tanzania and Zanzibar in East Africa, with Latham Island. (**G**) Drone photo of Latham Island, together with all flight trajectories of bat 1. Different colors denote different sessions; green dots denote the two platform locations. Scale bar, 50 m. (**H**) Photos taken on the island, depicting some of the landmarks that the bats may have used for navigation. See also fig. S4A. [Photos: (Top) Shaked Palgi; (Bottom) Chen Cohen] (**I**) Photograph of a landing platform [the east green dot in (G)]. Platform height, 1.8 m. [Photo: Nachum Ulanovsky] (**J**) Session duration (top) and total flight time (bottom) for each of the 22 outdoor sessions from the six bats. (**K** to **O**) Histograms of behavioral data from flight epochs only, pooled over all the outdoor sessions. (K) Flight speed (low speeds indicate moments when the bat turned sharply) ($n = 208{,}278$ GPS samples). (L) Flight altitude. (Left) Altitude above mean sea level, based on the altimeter. (Right) Altitude above ground [the ground level was taken from a drone-based digital elevation map, as in fig. S3E, and was subtracted from the flight altitude (*42*)]. Maximal altitudes reached >20 m but were clipped here for display purposes. (M) Area covered by the bats in each experimental session ($n = 22$ sessions). (N) Percentage of the island that was visible to the bat during flight at each moment [$n = 8252$ time points (1-s intervals); see also fig. S6]. (O) Number of accumulated full rotations (360°) per session, calculated by integrating the absolute values of the bat's turning angles ($n = 22$ sessions). (**P**) Angular coverage per session, for bat 1 [each line represents one session and shows the total flight time in each directional bin; *y* axis clipped at 60 s for clarity (dotted line marks the clipping)]. Same sessions and colors as in (G). (**Q**) Angular coverage per bat, averaged across all the sessions of each bat (gray, $n = 6$ bats), and grand average (black). N, north; E, east; S, south; W, west. (**R**) Comparison of heading direction versus head direction. Shown is the distribution of heading direction (*y* axis) for each head direction (*x* axis), pooled over all 17 sessions with magnetometer data (*42*). Head direction and heading direction were highly correlated (circular-circular correlation: $\rho = 0.88$).

Movie 1. Drone video footage of Latham Island. Drone video of the island taken during both experimental seasons. This video highlights the visual richness of the island with many available landmarks; we propose that these landmarks were used by the bats to align their neural compass. This video footage was taken during the day, whereas the experiments were conducted at night—but we note that these bats are highly visual (*52*,*62*) and could therefore see these visual features even on overcast nights or when the Moon was below the horizon. The bats could also sense these landmarks using other sensory systems, such as echolocation. Finally, we note that the birds visible in this footage were asleep during the night hours when we conducted our experiments, and therefore they did not interfere with the experiments. [Video: Shaked Palgi]

$\rho = 0.88$); and because the measurements of heading direction were more reliable (*42*), we subsequently used the heading direction to construct directional tuning curves.

Head-direction cells exist outdoors and have similar characteristics to those recorded indoors

We first asked whether head-direction coding exists in bats flying outdoors and whether it shows similar properties to directional coding in indoor situations. We focused here on azimuthal directional tuning because neuronal tuning to pitch (vertical) direction could not be computed, as the bats exhibited a very restricted range of pitch angles in-flight (fig. S5C). A total of 406 well-isolated neurons passed our inclusion criteria based on behavioral coverage and minimum spikes [we moved our tetrodes daily to allow the recording of new neurons (*42*)]. Of these, 97 neurons (24%) were classified as significant head-direction cells on the basis of their unimodal directional tuning compared with spike shuffles [Fig. 2, A to C; for detailed criteria see (*42*)]. These 97 head-direction cells were the focus of the analyses below. The head-direction cells were recorded in the dorsal presubiculum (59/97) and in the retrosplenial cortex (38/97). We pooled together the data from both brain regions because we did not find major differences between the two (fig. S7). This percentage of head-direction cells is consistent with previous reports from laboratory-based studies of these brain areas in rats and bats (*15*, *21*, *22*, *25*, *43*) [but see (*44*, *45*)]. The directional tuning of these neurons was stable over time within the session (Fig. 2. A and B, bottom-right raster; Fig. 2D; median stability score: Pearson correlation coefficient $r = 0.81$). The cells exhibited strong unimodal tuning (fig. S8, A to C), with a typical tuning width of $117 \pm 35°$ (mean ± SD, tuning width at half-height; fig. S8D)—slightly wider than reported in the presubiculum of rodents (*15*, *46*). Head-direction cells remained stable when comparing flight and stationary nonflight periods (Fig. 2, E and F, and fig. S9), as reported for head-direction cells in laboratory setups (*22*, *25*).

The two most prominent directional cues available outdoors at night are the Moon and the wind. We did not find any overrepresentation of these two variables (Moon, fig. S8, E and F; wind, fig. S8, G to I). Rather, the preferred directions of head-direction cells outdoors covered uniformly all possible directions (Fig. 2, G and H; Kuiper's test for uniformity: $P = 0.67$), similar to studies indoors (*15*, *22*). We controlled for nonuniform behavioral coverage (Fig. 1, P and Q): There was no association between the behavioral-coverage distribution and the tuning curves of the neurons (fig. S8, J and K).

We also examined the neural code for head direction at the population level. First, we trained a Bayesian decoder to decode the bat's direction from the neural activity of simultaneously recorded neurons [$n = 10$ sessions with ≥10 cells, out of which ≥5 were significant head-direction cells; we used 10-fold cross-validation (*42*)]. The decoding was successful, with a median decoding error of 30° (Fig. 2, I and J), indicating that the population of presubiculum neurons carries reliable directional information. Second, we used the uniform manifold approximation and projection (UMAP) dimensionality-reduction algorithm to plot the low-dimensional neural manifold of the population activity of head-direction cells. Our analysis revealed a ring-shaped structure (Fig. 2K), consistent with recent findings in rodents and flies (*47*–*50*).

Overall, we conclude that head-direction cells exist outdoors and have basic characteristics similar to those of the "classical" head-direction cells recorded indoors. This allowed us to further test their coding properties outdoors.

Head-direction tuning remained stable over the geographical scale of the island, consistent with a global compass

We next addressed our second main question, the stability of the directional tuning over the geographical scale of the island. The bats never had a complete view of the island, owing to occlusions from cliffs, boulders, and tents (Fig. 1N and fig. S6), and hence the set of sensory cues available to them at each location was different. One hypothesis would therefore be that head-direction cells represent orientation in a local mosaic manner, with each neuron exhibiting different preferred directions at different locations (fig. S1, left). Another hypothesis is that head-direction cells might represent orientation in a global fashion, with each neuron showing the same preferred direction across space (fig. S1, right).

We first examined the stability of the head-direction tuning across space by splitting the data into two equal parts on the basis of location and calculating the head-direction tuning separately for each half (Fig. 3A). The head-direction tuning was highly stable between the two halves (Fig. 3A, bottom, and Fig. 3B, left). We also examined whether the island's shore, a prominent elongated landmark, anchors the head-direction tuning. This was tested by splitting the data on the basis of the bat's proximity to the west shore or the south shore, which are ~90° from each other (fig. S3D)—if the shoreline aligned the directional tuning, we would expect ~90° rotation of the head-direction tuning between these two areas. However, the directional tuning showed high similarity between the regions (Fig. 3, B to D: median differences of <30°, or <22% of the cells' tuning width). The stability of the tuning was also maintained across additional spatial bisections that we performed (figs. S10 and S11) as well as when we split the data according to other behavioral variables, such as altitude, speed, and angular velocity (fig. S12). This high stability was robust to various choices of thresholds (figs. S11, G and H, and S13, C to G) and was confirmed using a cross-decoding analysis (fig. S13B).

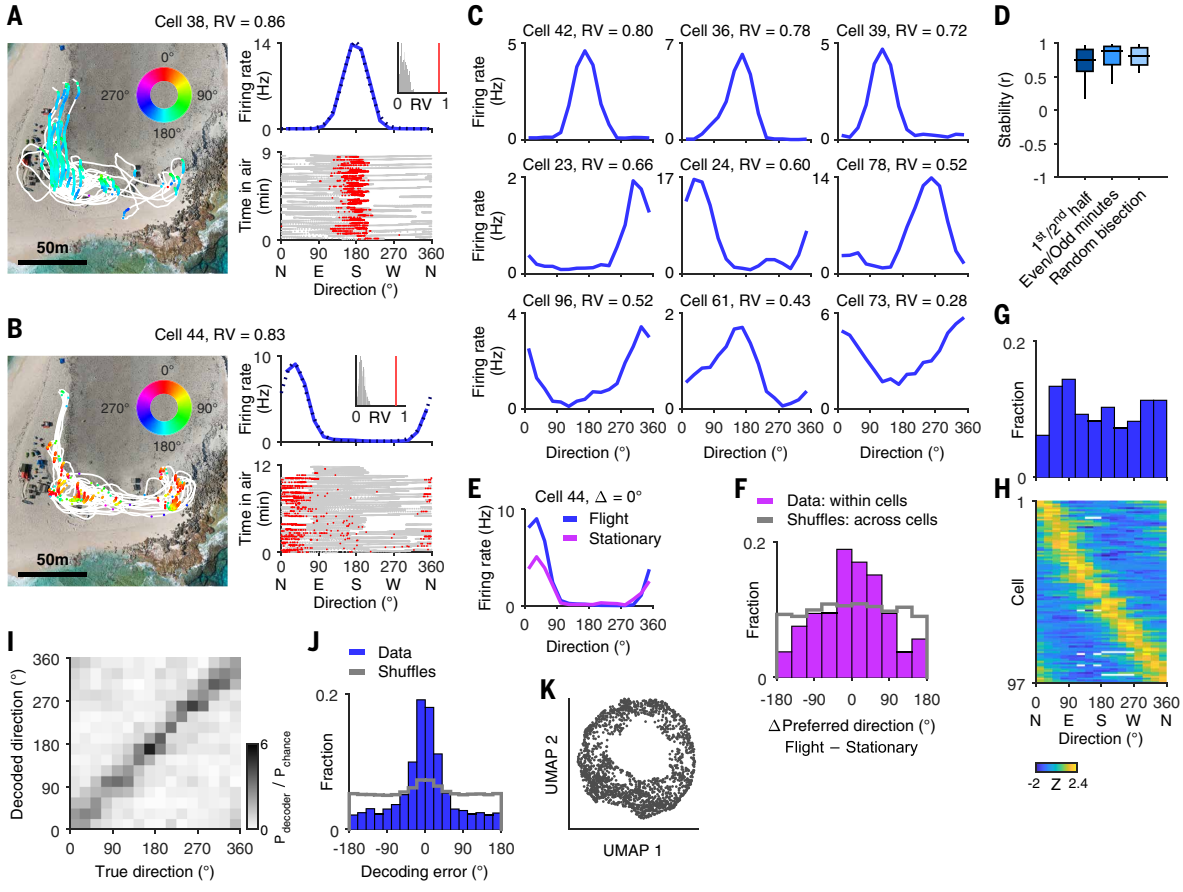

Fig. 2. Head-direction cells recorded outdoors. (**A**) Neuron with significant directional tuning. (Left) Flight trajectories (white) and spikes (colored dots), plotted on top of a drone photo of the island. Spike colors correspond to the bat's direction at the moment of firing; see circular color scale. (Top right) Directional tuning curve (blue), with fitted von Mises function (circular Gaussian; dotted line). (Bottom right) Bat's heading direction versus time (light gray), together with a spike raster (red dots). Time in air is the net flight time of the bat, from the session start to its end. (Inset) Rayleigh vector (RV) length of the cell's directional tuning curve (red line, RV = 0.86), and RV distribution for 1000 rigid spike-shuffles (gray). The RV of the data was larger than all 1000 shuffles. (**B**) Another head-direction cell (RV = 0.83); plotted as in (A). (**C**) Nine additional head-direction cells from five bats, showing their directional tuning curves. (**D**) Stability of directional tuning across the population of head-direction cells. The three boxplots show three different stability scores: Pearson correlation coefficient *r* for first half versus second half of the session ($n = 97$ cells), even versus odd minutes ($n = 82$ cells recorded for >2 min in air), and random bisections [$n = 97$ cells (*42*)]. Horizontal lines denote medians, boxes denote 25th–75th percentiles, and whiskers denote 10th–90th percentiles. (**E**) Head-direction tuning for a neuron recorded during flight (blue) and stationary nonflight (purple). Δ, absolute difference in preferred direction. (**F**) Histogram of ΔPreferred direction, calculated within cells (data: purple) and across cells (shuffles: gray). The differences in preferred direction were distributed around 0° (Rayleigh test for uniformity: $P = 0.0004$; $n = 53$ cells) (*42*). (**G**) Histogram of cells' preferred direction. Kuiper's test for uniformity: $P = 0.67$, indicating a uniform distribution. (**H**) Directional tuning for all the significant head-direction cells (rows, $n = 97$), sorted by the neuron's preferred direction. Tuning is *z*-scored (see color bar). (**I**) Decoding confusion matrix, pooled over the 10 sessions with enough neurons (*42*): the probability of decoded direction (*y* axis) for each true direction (*x* axis), normalized by the uniform chance probability $P_{chance} = 1/n_{bins}$ (see color bar). (**J**) Histogram of decoding errors (blue), pooled over the same 10 sessions as in (I). Median absolute error = 30°. Gray: decoding using rigid spike shuffles. Rayleigh test for uniformity: $P < 10^{-300}$, indicating highly nonuniform distribution; Wilcoxon rank-sum test comparing per-session median absolute error for data versus shuffle: $P = 0.002$. (**K**) UMAP dimensionality-reduction of the neuronal population activity in-flight, from a single experimental session, projected onto two UMAP components [using $n = 7$ simultaneously recorded head-direction cells; dots represent individual time points: 200-ms bins (*42*)], showing a ring-shaped neuronal manifold.

We next conducted a more systematic and fine-grained analysis of the head-direction tuning across space (Fig. 3, E to O). For each neuron, we binned the island into 40-by-40-m spatial bins (with a sliding-window step of 5 m) and computed the local directional tuning within each bin, generating two types of maps: (i) A preferred-direction map: the map of preferred directions across space (Fig. 3, G and J). (ii) A tuning correlation map: the map of Pearson correlations between the directional tuning computed within each bin and the tuning based on all the data outside that bin (Fig. 3, H and K). To quantify the degree of uniformity of these maps, we defined two indices of directional stability across space: (i) RV_{map}: the Rayleigh vector length of the distribution of preferred directions across space (computed from the preferred-direction maps; Fig. 3L) (*51*) and (ii) median correlation (computed from the tuning-correlation maps; Fig. 3M). We repeated these analyses using smaller bin sizes of 30-by-30 and 20-by-20 m (*42*). Overall, the neurons' preferred-direction maps were highly uniform (Fig. 3, G and J), corresponding to high values of RV_{map} (Fig. 3L, blue; median $RV_{map} = 0.66$ to 0.73 for the three spatial bin sizes)—very different from what is obtained using two types of shuffles [Fig. 3L, gray; here, we used both spike shuffles (dark gray) and cell shuffles (light gray), where we shuffled spatial bins across cells (*42*); 69 to 76% of the neurons were above the 95th percentile of both shuffles (significant cells)]. Similarly, the tuning correlation showed very high values across space (Fig. 3, H and K; Fig. 3M, blue; population median correlation: $r = 0.74$ to 0.75)—also very different from both types of shuffles (Fig. 3M, gray; 81 to 82% significant cells). The results were robust to the choice

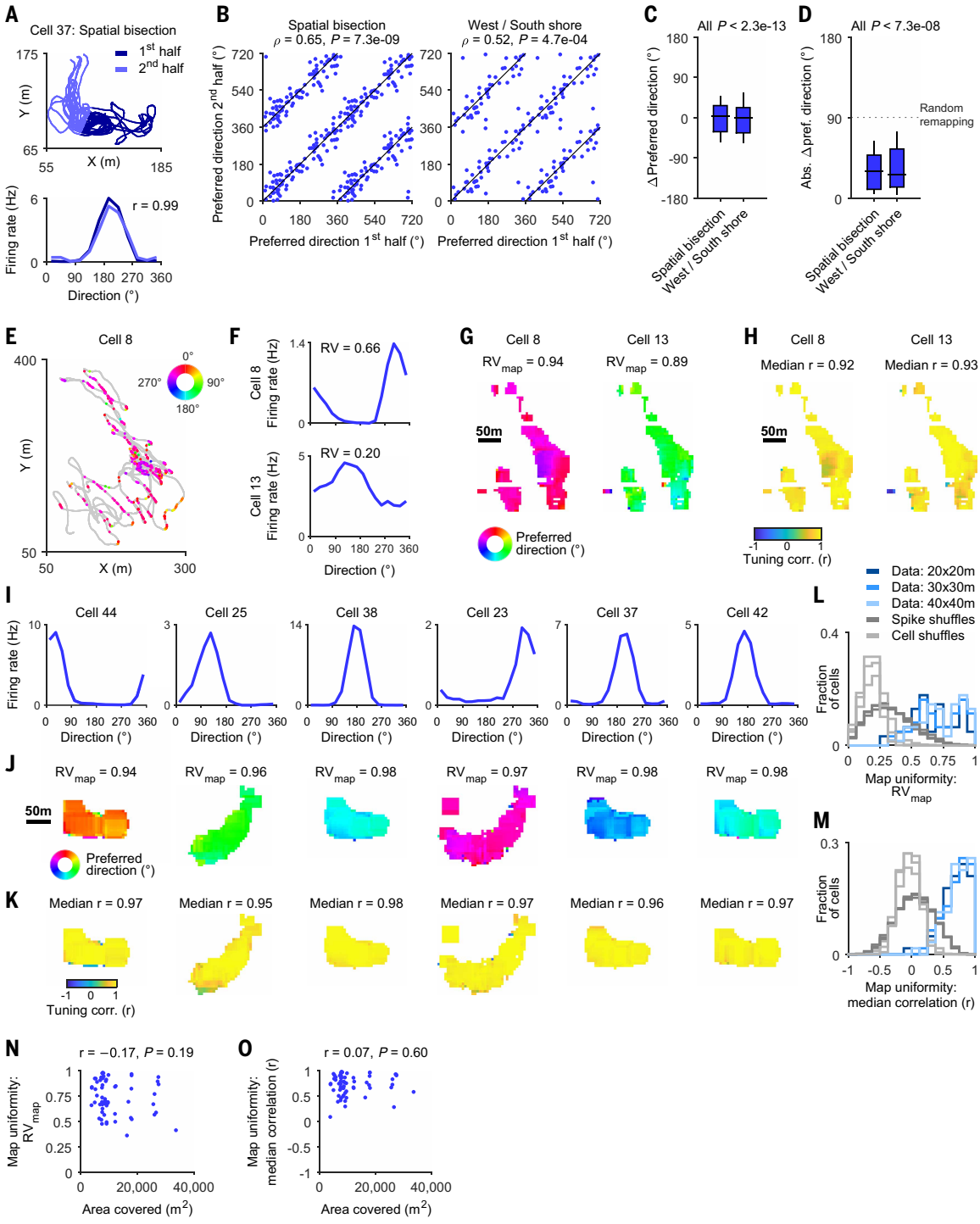

Fig. 3. Head-direction tuning remained stable across the geographical scale of the island. (**A**) Neuron showing stable tuning to spatial bisection of the bat's behavior. Trajectories (top) and directional tuning curves (bottom), plotted separately for the two halves of the data (light and dark blue). Note the high similarity of the two tuning curves (Pearson $r = 0.99$). (**B**) Preferred direction in the second half versus first half, for two types of spatial bisections: bisection along the long axis of the behavior (left) and separating the data on the basis of proximity to the west shore versus south shore (right) (*42*). Dots are neurons: $n = 85$ cells (left) and 50 cells (right) with enough data in each half. In each scatter, data are plotted twice from 0° to 360° and 360° to 720°, for display purposes; black lines, identity lines. Circular-circular correlation coefficients and P values are indicated. (**C**) Difference in preferred direction between the two halves (ΔPreferred direction; Rayleigh test for uniformity: All $P < 2.3 \times 10^{-13}$, indicating highly nonuniform distribution of differences). (**D**) Absolute value of ΔPreferred direction (Wilcoxon signed-rank test versus 90°: All $P < 7.3 \times 10^{-8}$). In all boxplots, horizontal lines denote medians, boxes denote 25th–75th percentiles, and whiskers denote 10th–90th percentiles. P values in (C) and (D) were Bonferroni-corrected for $n = 2$ comparisons; similar P values were obtained when comparing to cell shuffles. (**E** to **H**) Two simultaneously recorded head-direction cells. (E) Flight trajectories (gray curve) with overlayed spikes from one neuron (dots), colored by the bat's heading direction at the moment of firing (see circular color scale). (F) Directional tuning curves of the two neurons. RV: Rayleigh vector length of the tuning curve. (G) Preferred-direction maps. Each pixel's color represents the preferred direction of the directional tuning curve at that spatial bin. RV_{map}: Rayleigh vector length of the preferred-direction map (computed over all spatial bins). All maps were plotted using 40-m bins with 5-m steps (sliding window). (H) Tuning correlation

maps. Each pixel's color represents the Pearson correlation coefficient *r* between the directional tuning inside that spatial bin and the tuning computed using all the data outside this spatial bin. Median *r*: median tuning correlation across all spatial bins. (**I** to **K**) Six additional head-direction cells, showing (I) directional tuning curves, (J) preferred-direction maps, and (K) tuning correlation maps. Note the uniform preferred directions in (J) and high tuning correlations in (K), indicating high spatial stability of the head-direction tuning. (**L** and **M**) Population analysis quantifying the spatial stability of head-direction tuning curves using two different indices for map uniformity [computed for $n = 62$ cells with enough data (*42*)]. We repeated the calculation using three spatial bin sizes (20-by-20–, 30-by-30–, and 40-by-40–m bins; results plotted in different shades of blue) and using two types of shuffles: spike shuffles (dark gray) and cell shuffles (light gray). Note the higher values for the data compared with shuffles. (L) RV_{map}: Population medians = 0.66 to 0.73 (range across the three spatial bins); 69 to 76% significant cells compared with both shuffles. (M) Median tuning correlation: Population medians = 0.74 to 0.75; 81 to 82% significant cells. (**N**) No correlation between RV_{map} and the area covered by the bat [defined using the flight hull of the bat's spatial coverage (*42*); Pearson $r = -0.17$, $P = 0.19$; $n = 62$ cells]. (**O**) Same as (N), for the median tuning correlation versus area covered ($r = 0.07$, $P = 0.60$).

of spatial bin size (Fig. 3, L and M) and to the details of the shuffling procedure (fig. S14) and did not depend on the total area covered by the bats (Fig. 3, N and O).

Lastly, we explicitly searched for "mosaic cells," neurons that exhibit strong local head-direction tuning but only weak global tuning (figs. S1, left, and S15, A to H). To this end, we calculated a third type of map, where for each spatial bin we quantified the sharpness of the local directional tuning through its Rayleigh vector length (fig. S15D). We identified neurons with significant local tuning using shuffling, as before (*42*). This procedure yielded 32/213 (15%) putative mosaic neurons (fig. S15E). Notably, these putative mosaic neurons did not exhibit sharp local tuning (fig. S15F, red dots)—their local tuning was much less sharp than the local tuning of head-direction cells (fig. S15H). In fact, we found no compelling evidence for true mosaic neurons, as there were almost no neurons with strong local but weak global tuning (fig. S15F: no neurons in the top-left corner; and see fig. S15, A to D, for some of the most sharply tuned mosaic cells). Thus, these cells are possibly a separate weakly tuned functional class of neurons, rather than head-direction cells that remap across space.

Together, these analyses suggest that head-direction cells recorded outdoors encode orientation in a global manner over a large geographical region, which supports the global compass hypothesis (fig. S1, right) and argues against the local mosaic hypothesis (fig. S1, left).

Head-direction tuning remained stable despite dynamics of the Moon

We next addressed our third main question of whether the head-direction neural compass remains stable despite the movement of celestial cues. Because Egyptian fruit bats are nocturnal and highly visual animals (*4*, *52*–*54*), we sought to determine whether their neural compass anchors to the Moon.

In some of the sessions, we recorded head-direction cells before moonrise, waited for a few hours, and then recorded the same neurons again when the Moon had become visible (Fig. 4, A to C). The directional tuning of head-direction cells was highly stable when comparing flights with or without the Moon (Fig. 4, B and C; population: Fig. 4, D to G, light blue).

Stars and the Milky Way are also often visible in natural environments (*55*), and these cues were shown to aid animal navigation (*41*, *56*, *57*). Therefore, we compared the directional tuning of neurons when the Moon and stars were visible against periods of cloud coverage (which transiently obscured both the Moon and the stars). Again, the directional tuning of head-direction cells was highly stable when comparing flights with Moon and stars visible versus cloud coverage (Fig. 4, D to G, dark blue).

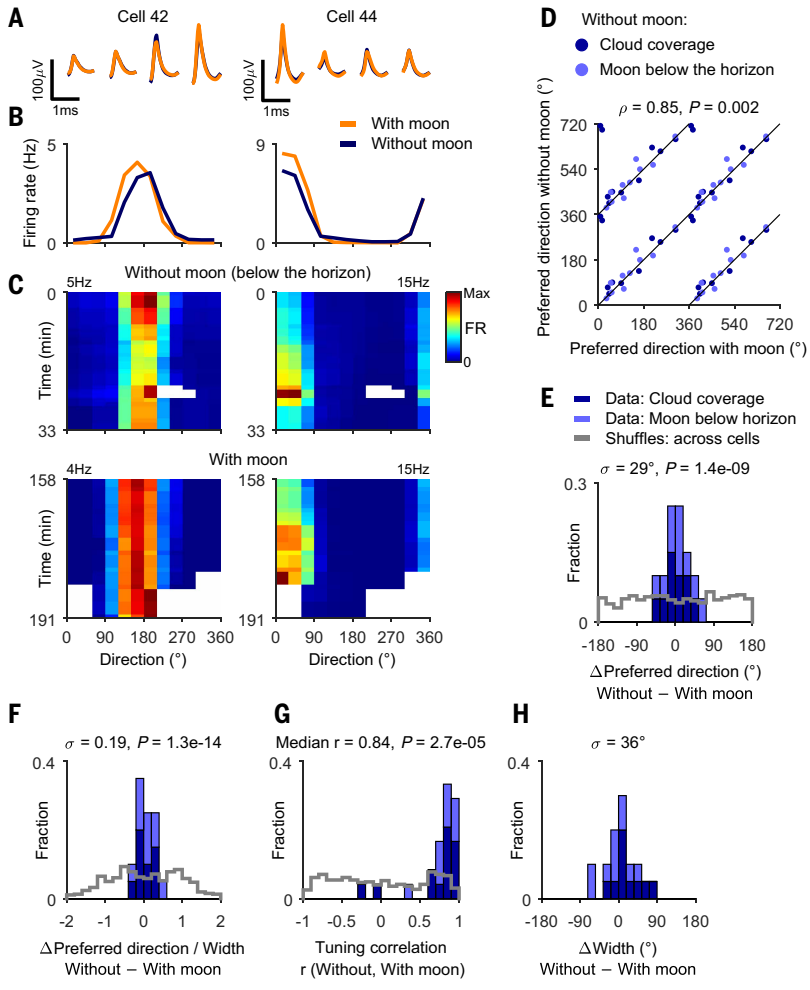

Fig. 4. Head-direction tuning remained stable despite dynamics of celestial cues. (**A** to **C**) Two neurons recorded simultaneously on different tetrodes. (A) Mean spike waveforms, plotted separately for the two parts of the recording session (dark blue: without Moon, orange: with Moon; the four lines correspond to the four channels of the tetrode). (B) Directional tuning curves, computed separately for the two parts of the session [same colors as in (A)]. (C) Firing rate (FR) as a function of direction (*x* axis) and time (*y* axis), for the two parts of the session: without Moon (top) and with Moon (bottom). White indicates bins without sufficient behavioral data. (**D** to **H**) Population analyses of cells recorded with and without Moon. In total, $n = 20$ neurons from four bats had enough data in both conditions (*42*); "Without moon" consists of cases when the Moon was below the horizon (light blue; $n = 10$ cells) or when the Moon was behind cloud coverage (dark blue; $n = 10$ cells). (D) Preferred direction without Moon versus preferred direction with Moon. Data are plotted twice from 0° to 360° and 360° to 720°, for display purposes; black lines are the identity lines; circular-circular correlation: $\rho = 0.85$, $P = 0.002$. (E) Stacked histograms of ΔPreferred direction (°), without Moon minus with Moon (blue), and the population cell shuffles (gray); σ, standard deviation. Rayleigh test for uniformity: $P = 1.4 \times 10^{-9}$. (F) Same as (E), with each cell normalized by its overall tuning width. Rayleigh test for uniformity: $P = 1.3 \times 10^{-14}$. (G) Histogram of tuning correlation (Pearson *r*) of the tuning curves with versus without Moon. Population median correlation: $r = 0.84$. Wilcoxon signed-rank test versus 0: $P = 2.7 \times 10^{-5}$. (H) Histogram of ΔWidth (°), Without–With Moon. Wilcoxon signed-rank test versus 0°: $P = 0.30$.

Thus, we observed exceptional stability of the head-direction tuning under both types of comparisons: (i) Moon visible versus Moon below the horizon, and (ii) Moon and stars visible versus cloud coverage. In both cases, we did not observe changes in the head-direction tuning—as manifested by the stability of the neurons' preferred direction (Fig. 4D, circular-circular correlation: $\rho = 0.85$, $P = 0.002$; Fig. 4, E and F, Rayleigh test for uniformity: $P = 1.4 \times 10^{-9}$ and $P = 1.3 \times 10^{-14}$), their high tuning correlations (Fig. 4G; median correlation: $r = 0.84$; Wilcoxon signed-rank test versus 0: $P = 2.7 \times 10^{-5}$), and their stable tuning width (Fig. 4H; Wilcoxon signed-rank test versus 0°: $P = 0.30$). A decoding analysis further confirmed that the Moon's presence does not contribute to the directional coding of head-direction cells (fig. S16, B to D).

Head-direction tuning stabilized over several nights of exploring a novel real-world environment

This was the first-ever exposure of these bats to this environment, which presented an opportunity to study the ontogeny of the head-direction signal in a new natural environment. We examined the dynamics of the head-direction tuning across multiple nights, in search of signatures of learning. Because our neural-recording method does not allow tracking the same individual neurons over consecutive nights, we examined whether there are population-level differences in the stability of the head-direction tuning between neurons that were recorded during the first nights outdoors and neurons recorded on later nights. Although the cells were generally very stable (Figs. 2D and 3M), we hypothesized that cells recorded in earlier nights might be less stable.

For each neuron, we examined the prevalence of rapid within-session dynamics. We used the data from the first 10 min of the session and compared the tuning in the first 5 min (minutes 0 to 5) with the tuning in the next 5 min (minutes 5 to 10). Some of the neurons recorded over the first few nights exhibited large changes in the first 10 min of the session—changes that were not observed in neurons recorded on later nights (Fig. 5, A and B; population: Fig. 5C, left). Similar results were found when repeating this calculation using the last 10 min of the sessions (Fig. 5C, right). Thus, we observed transient dynamics of the head-direction tuning in the first few nights of flight outdoors, which slowly stabilized as the bats explored the island on consecutive nights [Fig. 5C; Spearman correlations: session start (first 10 min): $\rho = -0.38$, $P = 0.002$; session end (last 10 min): $\rho = -0.50$, $P = 0.0005$]. We also calculated the head-direction tuning along the session in time windows of 15 min and fitted a circular-linear regression to the preferred direction of each neuron as a function of time within the session (*42*). We observed faster drift of the preferred direction (steeper regression slopes) in early nights than in later nights (Fig. 5D; $\rho = -0.60$, $P = 10^{-8}$), which is consistent with a gradual stabilization of the directional code. The directional coding reached high stability on later nights, as indicated by very small changes of the preferred direction during the session (Fig. 5D, nights 3 to 6).

To examine potential changes in the spatial stability of directional tuning across nights, we tested whether neurons' median correlation index (as in Fig. 3, K and M) varied as a function of their recording night. Neurons became more spatially stable as the bats flew more nights outdoors (Fig. 5E; $\rho = 0.31$, $P = 0.015$).

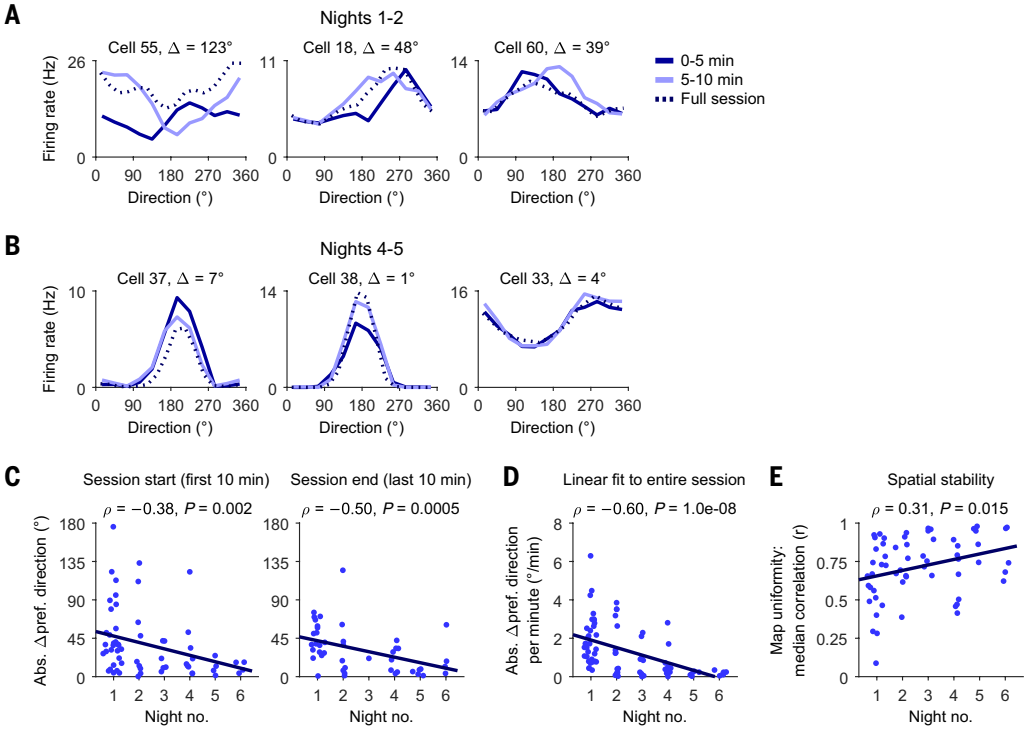

Fig. 5. Head-direction tuning stabilized across nights. (**A** and **B**) Neurons recorded on different nights. (A) Three neurons recorded on nights 1 and 2. Tuning was calculated separately for the first 5 min of the session (dark blue), for the next 5 min (light blue), and for the overall session (dashed lines). The neuronal tuning changed between these 5-min segments; Δ indicates the absolute ΔPreferred direction. (B) Three different neurons, recorded on nights 4 and 5; plotted as in (A). (**C**) Directional-tuning changes across nights. (Left) Absolute difference between the preferred direction calculated during the first 5 min and the next 5 min, plotted as a function of night of recording ($n = 62$ neurons with enough data; dark blue line, regression line; Spearman correlation: $\rho = -0.38$, $P = 0.002$). (Right) As in left panel, but comparing the last 5 min to the penultimate 5 min ($n = 45$ neurons; Spearman correlation: $\rho = -0.50$, $P = 0.0005$). (**D**) Slopes of within-session linear fits to the preferred direction of each neuron; the slopes are plotted here against night number, as in (C) ($n = 77$ neurons with enough data; Spearman correlation: $\rho = -0.60$, $P = 10^{-8}$). (**E**) Spatial stability across nights. Median tuning correlation (same index plotted in Fig. 3M) as a function of the night of recording ($n = 60$ neurons with enough data; Spearman correlation: $\rho = 0.31$, $P = 0.015$); plotted as in (C). The dots in (C) to (E) were slightly jittered horizontally, for display purposes only.

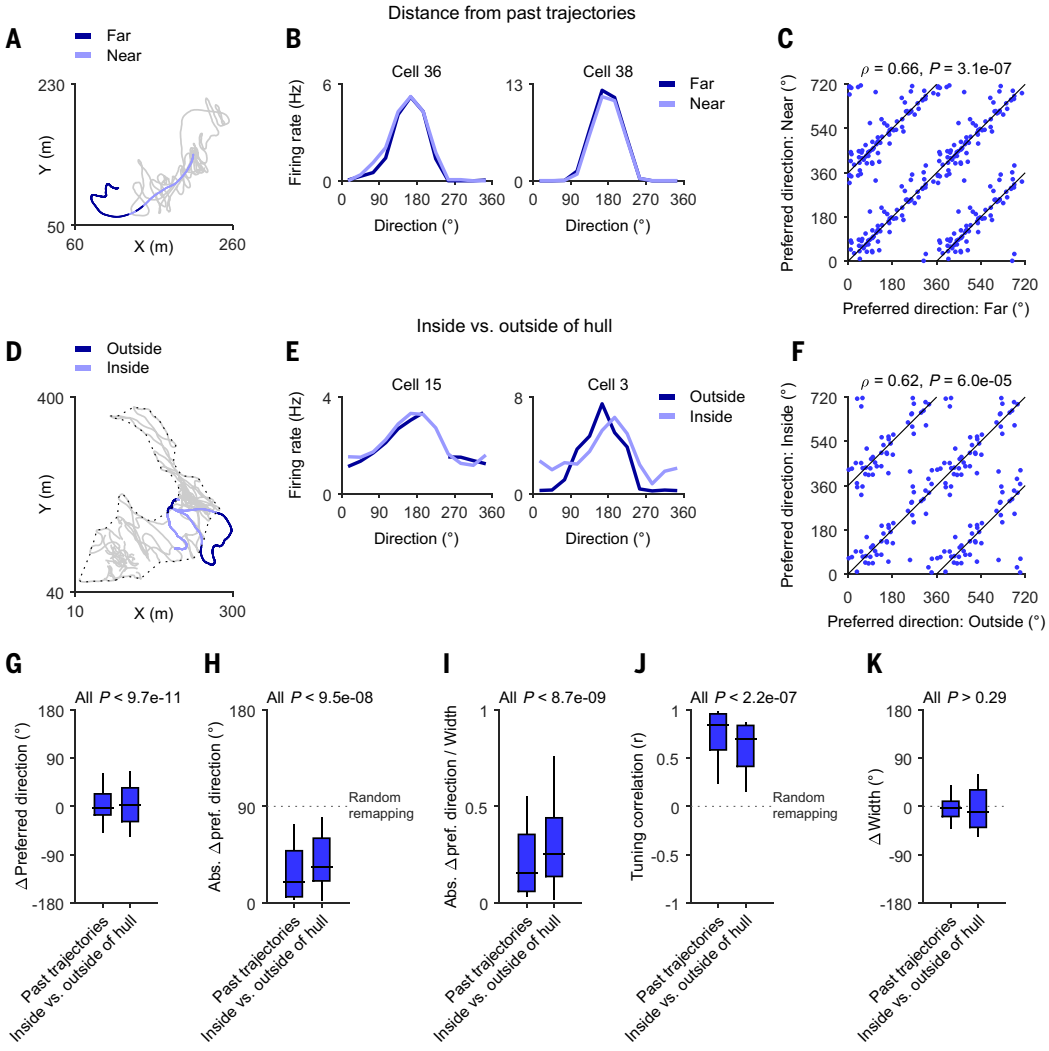

Fig. 6. Head-direction tuning remained stable during novel trajectories. (**A** to **C**) Bisection of the data by the distance to the past trajectories of the bat in the same session. (A) Example flight trajectory, colored by the distance to the past flight trajectories in this session (light blue, near; dark blue, far). Gray trace represents all the past trajectories in this session (the set of past trajectories was dynamically updated on a flight-by-flight basis). The "far" portion of this flight had a duration of 21 s. (B) Two neurons with enough data for this bisection (recorded simultaneously on different tetrodes). For each cell, two directional tuning curves are plotted, computed from all the flights in the two halves of the data [same colors as in (A)]. (C) Population scatterplot of the preferred direction in the second half (near) versus first half (far), plotted as in Fig. 3B (circular-circular correlation: $\rho = 0.66$, $P = 3.1 \times 10^{-7}$; $n = 76$ head-direction cells with enough data in both halves). (**D** to **F**) Split of the data by the dynamic flight hull, which is based on the entire history of the bat across all sessions. (D) Example flight, plotted as in (A) (light blue, inside the flight hull; dark blue, outside the flight hull; gray, past flights in all the previous sessions; dashed line, dynamic flight hull). The "outside hull" portion of this flight had a duration of 36 s. (E) Two neurons, with the two colors indicating the two splits of the data [same colors as in (D)]. (F) Population scatterplot for this bisection, plotted as in (C) ($\rho = 0.62$, $P = 6 \times 10^{-5}$; $n = 47$ cells). (**G** to **K**) Population boxplots for both types of bisections. Horizontal lines in boxplots denote medians, boxes denote 25th–75th percentiles, whiskers denote 10th–90th percentiles. (G) Difference in preferred direction between the two halves (ΔPreferred direction; Rayleigh test for uniformity: all $P < 9.7 \times 10^{-11}$). (H) Absolute value of ΔPreferred direction (Wilcoxon signed-rank test versus 90°: all $P < 9.5 \times 10^{-8}$). (I) Absolute value of ΔPreferred direction, normalized by each cell's overall tuning width (Kolmogorov-Smirnov test versus cell shuffles: all $P < 8.7 \times 10^{-9}$. (J) Tuning correlation (Pearson r) between the first half and second half (Wilcoxon signed-rank test versus 0: all $P < 2.2 \times 10^{-7}$). (K) Differences in tuning width between the first half and second half (Wilcoxon signed-rank test versus 0°: all $P > 0.29$). All P values in (G) to (K) were Bonferroni-corrected for the $n = 2$ comparisons; we note that similar P values were obtained when comparing with cell shuffles.

These dynamics of the head-direction code across nights could not be explained by changes in behavior (fig. S17, P to U), changes in spike-sorting quality (fig. S17, J to O), or differences in anatomical recording areas (fig. S17, A to I).

Head-direction tuning remained stable during flights outside a bat's familiar area

Is the head-direction tuning stable when a bat flies for the first time over a new region of the island? We first bisected the data on the basis of its spatial distance from all the previous flights in the same session (Fig. 6A) (*42*). This analysis showed stable directional tuning when comparing moments when the bat was near versus far away from previous flights of the same session (Fig. 6, B and C; near versus far: $\rho = 0.66$, $P = 3.1 \times 10^{-7}$). We then defined for each bat a behavioral "flight hull," which encompassed the region of the island that this bat had already explored during this session and previous sessions (*42*). This allowed us to compare moments when the bat flew over a region of the island that it had already explored ("inside hull") against flights over regions it had never visited before ("outside hull"; Fig. 6D, example), which again showed stable directional tuning for familiar versus novel trajectories (Fig. 6, E and F; inside versus outside hull: $\rho = 0.62$, $P = 6.0 \times 10^{-5}$). Both types of analyses showed high stability of the

directional tuning compared with random remapping (random rotation) of the tuning curve (Fig. 6, G to J), with no significant changes in tuning width (Fig. 6K; see also fig. S18, A and B, for varying distance thresholds from past trajectories and from the flight hull).

Even though these bats generally avoid prolonged flights over water, we observed two cases where bats flew far away from the island, toward the ocean (fig. S18C; see also fig. S2B, bats 3 and 6; flight durations = 38 and 104 s, respectively; maximal distance from shore = 118 and 282 m, respectively). Our fast boat waited in the water at night and safely captured these bats in both cases. Thus, we could compare the head-direction tuning above land to the tuning above the ocean. Although only a small number of head-direction cells were recorded during these two extreme flights, these few neurons showed stability of their directional tuning over land and over the ocean (fig. S18D).

Discussion

Here we have reported single-unit neural recordings conducted on a remote island where fruit bats navigated freely (Fig. 1). We identified head-direction cells that showed similar properties to classical head-direction cells (Fig. 2), supporting the relevance of head-direction cells for outdoor navigation. These neurons exhibited highly stable directional tuning across the island's geography (Fig. 3), suggesting a global representation of direction in the head-direction network (fig. S1, right), rather than a mosaic representation (fig. S1, left), at least on the scale of the island. The stable head-direction tuning was also robust to the dynamics of celestial cues, such as the movement of the Moon and stars (Fig. 4). Together, these results suggest that head-direction cells can serve as a stable and reliable neural compass for real-world navigation outdoors.

A potential limitation of this study is that we computed tuning curves to heading direction rather than head direction, because heading-direction measurements (Fig. 1C) were more precise and more technically reliable in our data. We note that head direction and heading direction are highly correlated in Egyptian fruit bats (Fig. 1R, $\rho = 0.88$). However, they can sometimes differ, potentially yielding better coding for head direction during these rare moments of mismatch (*58*). This subtle difference could potentially explain why we observed slightly wider tuning during high-flight-curvature moments (fig. S12F), which are the only moments when head direction and heading direction are expected to differ (*59*).

What are the sensory cues that the bats used to generate their stable neuronal sense of direction? For short timescales of several seconds, the bats may have used internal sensory cues via path-integration mechanisms. However, path integration accumulates errors over the course of multiple turns (*60*, *61*), and it is therefore unreliable over longer timescales of minutes. As the bats performed dozens of angular turns per session (Fig. 1O), they must have also used external cues to orient themselves. Egyptian fruit bats have excellent olfaction, hearing, and vision (*53*, *62*), so potentially all these sensory modalities can be used to anchor their compass. There are two categories of sensory cues that can be used for directional orientation: (i) Global directional cues, whose angles relative to the animal do not depend on its position, allowing for easy computation of head direction; these cues include the direction of Earth's magnetic field, the direction of the wind, the sound of breaking waves, and the angle of celestial cues. (ii) Local landmarks (including the geometry of the environment), perceived through vision, olfaction, or echolocation. It is likely that, on the island, the bats used local landmarks more than global cues, for the following reasons.

1) Magnetoreception: The use of magnetoreception by our bats is inconsistent with the dynamics observed in the neural code across nights (Fig. 5), because Earth's magnetic field is constantly present and therefore was available to the bats from the first moment. It is also inconsistent with results of additional experiments that we conducted inside a flight tent on the island: We found that the head-direction tuning rotated between indoor flight and outdoor flight (fig. S19), which is inconsistent with magnetic alignment, because Earth's magnetic field is identical indoors and outdoors. The use of magnetoreception is also unlikely given a separate laboratory magnetic-manipulation experiment that we conducted: See supplementary results in the supplementary materials and fig. S20. Finally, we note that there is no compelling evidence to date for magnetoreception in any nonmigratory bat species, Egyptian fruit bats included.

2) Olfaction and wind direction: For olfaction to be a reliable global directional cue, the wind direction needs to be stable, which is not the case in most natural environments, including in our recordings (fig. S8G). Furthermore, we could not find any correlation between the variability in wind direction and the variability in the neuronal preferred direction (fig. S8I). This argues against the notion that the head-direction tuning was anchored by smelling wind-carried odorants or by sensing the wind direction itself (through somatosensation).

3) Hearing: The sounds of the breaking sea waves are unlikely to be a useful global cue for bats, as waves can appear from multiple directions and also because most of the acoustic energy of breaking waves is at low frequencies (*63*), below the minimum frequency that these bats can hear (*64*). We also did not find stable directional tuning inside the tent compared with outdoors (fig. S19, D and E), although the sound of waves was available in both conditions.

4) Vision: The main global visual directional cues are distant celestial cues (Moon, stars) or gradients of light across the sky (from the Moon below the horizon, or from distant human activity). However, their sole use was unlikely, because head-direction cells exhibited almost identical directional tuning both with and without the presence of the Moon and also during overcast nights with cloud coverage, when none of the distant celestial or anthropogenic visual cues were available (Fig. 4, B to G). Nevertheless, it is possible that when the Moon and stars are visible, bats are able to maintain a sense of direction by compensating for the dynamics of these celestial cues, similar to the ability of some species to compensate for movements of the Sun (*2*, *35*, *36*). However, this hypothesis seems unlikely because the dynamics of the Moon are much harder to predict and compensate for than the dynamics of the Sun (*40*) and because the moonrise–moonset cycle is decorrelated from nighttime. Nevertheless, it may be that when celestial cues and wind were available, the bats used them to transiently anchor their compass.

This leaves us with the second main possibility, namely, that the head-direction tuning is computed by learning a configuration of local landmarks (including the island's geometrical features). Landmark-based navigation is a viable strategy outdoors because natural environments are highly structured and contain extremely rich landmark information, across modalities (*5*, *65*) (see Fig. 1H and fig. S4 for the high visual richness of the island). These landmarks can be perceived by any available modality, such as vision, olfaction, or echolocation, or through their multisensory combination (*5*, *52*, *62*, *66*, *67*). We believe that vision is the dominant modality for sensing landmarks in our experiments, because Egyptian fruit bats have excellent vision (*4*, *52*, *53*, *62*, *68*) and because vision has a longer range than the other senses. We propose that using local landmarks is the main strategy used by bats in real-world, cue-rich environments.

Regardless of the sensory modality, bats need to learn a set of multiple landmarks. They cannot rely on a single landmark, for two reasons: (i) In such large environments, not all landmarks are visible from all locations (Fig. 1N and fig. S6). (ii) If a single landmark had been used, the angle to it would change continuously as the bat moves through space, creating a "pinwheel" representation, wherein the preferred direction rotates around the focal landmark. However, this is not what we found; instead, we discovered a highly stable representation of direction throughout the space of the island (Fig. 3). This implies that a non-trivial computation must be performed to combine information from multiple landmarks to extract the bat's direction. Such computations were investigated previously in several theoretical studies, which suggested algorithmic solutions for generating stable head-direction coding from a set of landmarks (*69*, *70*). This computation was proposed to involve a number of brain regions, including the hippocampus, presubiculum, and retrosplenial cortex (*69*). As this computation relies on learning the

spatial arrangement of multiple landmarks, this learning process would need some time to take place and to stabilize in a completely new environment such as the island in our study (*67*, *69*, *71*). Indeed, we found here that the head-direction representation was less stable in the first two nights of exposure to the island and stabilized over the course of a few nights (Fig. 5). Notably, these models also allow the network to ignore unreliable dynamic cues [see also (*71*, *72*)]. This might explain why in our outdoor experiments, the head-direction cells seemed to ignore the easier-to-compute, but unreliable, dynamic celestial cues. Instead, the cells relied on the more computationally demanding but highly reliable information provided by multiple static landmarks.

Another possibility is that bats use a combination of global cues and local landmarks, wherein celestial cues participate in the initial binding of the set of landmarks into a global compass. For five of the six bats, the first night outdoors was a night with visible Moon and stars. We therefore hypothesize that on the first night, these bats could potentially anchor their compass using the clearly visible celestial cues, such as the Moon and Milky Way. This initial anchoring could accelerate the learning process by providing ground-truth directional information, and it can also explain the existence of a subpopulation of neurons already stably tuned on the first night (Fig. 5, C to E). Subsequently, on later nights, after the bats learned the landmark configuration on the island, their neural compass became independent of the celestial cues, and then they could use the landmarks to navigate on moonless nights (Fig. 4).

Overall, the results of this study imply that head-direction cells can indeed serve as a neural compass. Our study emphasizes the need to investigate the neurobiology of navigation in the wild. More generally, we call for broadening the scope of brain research toward neuroscience in the real world.

Materials and methods summary

We conducted wireless tetrode recordings in the dorsal presubiculum and retrosplenial cortex of bats that flew unconstrained over a remote oceanic island near East Africa. We caught adult Egyptian fruit bats (*R. aegyptiacus*) on the mainland, implanted them with a 16-tetrode microdrive, and then sailed to the island, where we conducted nightly recordings, one bat at a time. On the island, we kept moving the tetrodes to allow the recording of different neurons every night. We recorded single-unit neuronal activity together with behavioral measurements collected by onboard sensors: precise localization and flight direction (using GPS), kinematics (using an accelerometer and magnetometer), and altitude (using a pressure-based altimeter). We used a drone to obtain a 10-cm-resolution elevation map of the island and calibrated it with the GPS and altimeter. We also measured the wind direction using a portable weather station and logged Moon visibility online; Moon direction was calculated offline from astronomical databases. We identified head-direction cells on the basis of the Rayleigh vector length of their tuning curves compared with shuffles, and we tested their spatial stability by calculating the local directional tuning across the island. On some nights, we recorded both when the Moon and stars were visible in the sky and when they were occluded by heavy clouds or when the Moon was below the horizon, allowing us to compare these conditions. For some of the bats, we also recorded the same neurons inside a flight tent, comparing directional tuning indoors and outdoors. Finally, we conducted an experiment in our flight tunnel in Israel, where we recorded neurons in dorsal hippocampus area CA1 (cornu ammonis 1) using similar methods while transiently manipulating the magnetic field inside the tunnel. Further details are found in the supplementary materials and methods (*42*).

REFERENCES AND NOTES

1. R. Kays, M. C. Crofoot, W. Jetz, M. Wikelski, Terrestrial animal tracking as an eye on life and planet. *Science* **348**, aaa2478 (2015). doi: 10.1126/science.aaa2478; pmid: 26068858
2. H. G. Wallraff, *Avian Navigation: Pigeon Homing as a Paradigm* (Springer, 2005).
3. R. Wehner, *Desert Navigator: The Journey of an Ant* (Harvard Univ. Press, 2020).
4. A. Tsoar *et al.*, Large-scale navigational map in a mammal. *Proc. Natl. Acad. Sci. U.S.A.* **108**, E718–E724 (2011). doi: 10.1073/pnas.1107365108; pmid: 21844350
5. A. Goldshtein *et al.*, Acoustic cognitive map-based navigation in echolocating bats. *Science* **386**, 561–567 (2024). doi: 10.1126/science.adn6269; pmid: 39480949
6. O. Lindecke, A. Elksne, R. A. Holland, G. Pētersons, C. C. Voigt, Experienced migratory bats integrate the sun's position at dusk for navigation at night. *Curr. Biol.* **29**, 1369–1373.e3 (2019). doi: 10.1016/j.cub.2019.03.002; pmid: 30955934
7. S. Engels *et al.*, Anthropogenic electromagnetic noise disrupts magnetic compass orientation in a migratory bird. *Nature* **509**, 353–356 (2014). doi: 10.1038/nature13290; pmid: 24805233
8. W. Wiltschko, R. Wiltschko, Magnetic compass of European robins. *Science* **176**, 62–64 (1972). doi: 10.1126/science.176.4030.62; pmid: 17784420
9. M. Zapka *et al.*, Visual but not trigeminal mediation of magnetic compass information in a migratory bird. *Nature* **461**, 1274–1277 (2009). doi: 10.1038/nature08528; pmid: 19865170
10. J. O'Keefe, J. Dostrovsky, The hippocampus as a spatial map. Preliminary evidence from unit activity in the freely-moving rat. *Brain Res.* **34**, 171–175 (1971). doi: 10.1016/0006-8993(71)90358-1; pmid: 5124915
11. J. O'Keefe, Place units in the hippocampus of the freely moving rat. *Exp. Neurol.* **51**, 78–109 (1976). doi: 10.1016/0014-4886(76)90055-8; pmid: 1261644
12. M. Fyhn, S. Molden, M. P. Witter, E. I. Moser, M.-B. Moser, Spatial representation in the entorhinal cortex. *Science* **305**, 1258–1264 (2004). doi: 10.1126/science.1099901; pmid: 15333832
13. T. Hafting, M. Fyhn, S. Molden, M.-B. Moser, E. I. Moser, Microstructure of a spatial map in the entorhinal cortex. *Nature* **436**, 801–806 (2005). doi: 10.1038/nature03721; pmid: 15965463
14. J. B. Ranck Jr., "Head direction cells in the deep cell layer of dorsal presubiculum in freely moving rats" in *Electrical Activity of the Archicortex*, G. Buzsáki, C. H. Vanderwolf, Eds. (Akademiai Kiado, 1985), pp. 217–220.
15. J. S. Taube, R. U. Muller, J. B. Ranck Jr., Head-direction cells recorded from the postsubiculum in freely moving rats. I. Description and quantitative analysis. *J. Neurosci.* **10**, 420–435 (1990). doi: 10.1523/JNEUROSCI.10-02-00420.1990; pmid: 2303851
16. J. S. Taube, R. U. Muller, J. B. Ranck Jr., Head-direction cells recorded from the postsubiculum in freely moving rats. II. Effects of environmental manipulations. *J. Neurosci.* **10**, 436–447 (1990). doi: 10.1523/JNEUROSCI.10-02-00436.1990; pmid: 2303852
17. D. Yoganarasimha, X. Yu, J. J. Knierim, Head direction cell representations maintain internal coherence during conflicting proximal and distal cue rotations: Comparison with hippocampal place cells. *J. Neurosci.* **26**, 622–631 (2006). doi: 10.1523/JNEUROSCI.3885-05.2006; pmid: 16407560
18. M. P. Brandon, A. R. Bogaard, N. W. Schultheiss, M. E. Hasselmo, Segregation of cortical head direction cell assemblies on alternating theta cycles. *Nat. Neurosci.* **16**, 739–748 (2013). doi: 10.1038/nn.3383; pmid: 23603709
19. L. M. Giocomo *et al.*, Topography of head direction cells in medial entorhinal cortex. *Curr. Biol.* **24**, 252–262 (2014). doi: 10.1016/j.cub.2013.12.002; pmid: 24440398
20. A. Peyrache, M. M. Lacroix, P. C. Petersen, G. Buzsáki, Internally organized mechanisms of the head direction sense. *Nat. Neurosci.* **18**, 569–575 (2015). doi: 10.1038/nn.3968; pmid: 25730672
21. D. E. Angelaki *et al.*, A gravity-based three-dimensional compass in the mouse brain. *Nat. Commun.* **11**, 1855 (2020). doi: 10.1038/s41467-020-15566-5; pmid: 32296057
22. A. Finkelstein *et al.*, Three-dimensional head-direction coding in the bat brain. *Nature* **517**, 159–164 (2015). doi: 10.1038/nature14031; pmid: 25470055
23. N. Ulanovsky, *Natural Neuroscience: Toward a Systems Neuroscience of Natural Behaviors* (MIT Press, 2025). doi: 10.7551/mitpress/10813.001.0001
24. T. Wolbers, J. M. Wiener, Challenges for identifying the neural mechanisms that support spatial navigation: The impact of spatial scale. *Front. Hum. Neurosci.* **8**, 571 (2014). doi: 10.3389/fnhum.2014.00571; pmid: 25140139
25. J. S. Taube, The head direction signal: Origins and sensory-motor integration. *Annu. Rev. Neurosci.* **30**, 181–207 (2007). doi: 10.1146/annurev.neuro.29.051605.112854; pmid: 17341158
26. E. I. Moser, M.-B. Moser, B. L. McNaughton, Spatial representation in the hippocampal formation: A history. *Nat. Neurosci.* **20**, 1448–1464 (2017). doi: 10.1038/nn.4653; pmid: 29073644
27. M. B. Zugaro, A. Berthoz, S. I. Wiener, Background, but not foreground, spatial cues are taken as references for head direction responses by rat anterodorsal thalamus neurons. *J. Neurosci.* **21**, RC154 (2001). doi: 10.1523/JNEUROSCI.21-14-j0001.2001; pmid: 11425881
28. J. P. Goodridge, J. S. Taube, Preferential use of the landmark navigational system by head direction cells in rats. *Behav. Neurosci.* **109**, 49–61 (1995). doi: 10.1037/0735-7044.109.1.49; pmid: 7734080
29. R. W. Stackman, E. J. Golob, J. P. Bassett, J. S. Taube, Passive transport disrupts directional path integration by rat head direction cells. *J. Neurophysiol.* **90**, 2862–2874 (2003). doi: 10.1152/jn.00346.2003; pmid: 12890795
30. P. A. Dudchenko, L. E. Zinyuk, The formation of cognitive maps of adjacent environments: Evidence from the head direction cell system. *Behav. Neurosci.* **119**, 1511–1523 (2005). doi: 10.1037/0735-7044.119.6.1511; pmid: 16420155
31. J. S. Taube, H. L. Burton, Head direction cell activity monitored in a novel environment and during a cue conflict situation. *J. Neurophysiol.* **74**, 1953–1971 (1995). doi: 10.1152/jn.1995.74.5.1953; pmid: 8592189
32. R. M. Yoder *et al.*, Both visual and idiothetic cues contribute to head direction cell stability during navigation along complex routes. *J. Neurophysiol.* **105**, 2989–3001 (2011). doi: 10.1152/jn.01041.2010; pmid: 21451060

33. A. E. Smith, E. R. Wood, P. A. Dudchenko, The stimulus control of local enclosures and barriers over head direction and place cell spatial firing. *Brain Behav.* **11**, e02070 (2021). doi: 10.1002/brb3.2070; pmid: 33606361
34. K. J. Jeffery, The mosaic structure of the mammalian cognitive map. *Learn. Behav.* **52**, 19–34 (2024). doi: 10.3758/s13420-023-00618-9; pmid: 38231426
35. T. W. Cronin, S. Johnsen, N. J. Marshall, E. J. Warrant, "Visual orientation and navigation" in *Visual Ecology* (Princeton Univ. Press, 2014), pp. 289–312.
36. J. L. Gould, Sensory bases of navigation. *Curr. Biol.* **8**, R731–R738 (1998). doi: 10.1016/S0960-9822(98)70461-0; pmid: 9778524
37. A. Rozhok, *Orientation and Navigation in Vertebrates* (Springer, 2008).
38. B. el Jundi *et al.*, Neural coding underlying the cue preference for celestial orientation. *Proc. Natl. Acad. Sci. U.S.A.* **112**, 11395–11400 (2015). doi: 10.1073/pnas.1501272112; pmid: 26305929
39. H. Mouritsen, Long-distance navigation and magnetoreception in migratory animals. *Nature* **558**, 50–59 (2018). doi: 10.1038/s41586-018-0176-1; pmid: 29875486
40. J. E. Huth, *The Lost Art of Finding Our Way* (Harvard Univ. Press, 2013).
41. D. Dreyer *et al.*, Bogong moths use a stellar compass for long-distance navigation at night. *Nature* **643**, 994–1000 (2025). doi: 10.1038/s41586-025-09135-3; pmid: 40533549
42. Materials and methods are available as supplementary materials.
43. P. A. LaChance, M. E. Hasselmo, Distinct codes for environment structure and symmetry in postrhinal and retrosplenial cortices. *Nat. Commun.* **15**, 8025 (2024). doi: 10.1038/s41467-024-52315-4; pmid: 39271679
44. A. S. Alexander *et al.*, Egocentric boundary vector tuning of the retrosplenial cortex. *Sci. Adv.* **6**, eaaz2322 (2020). doi: 10.1126/sciadv.aaz2322; pmid: 32128423
45. P.-Y. Jacob *et al.*, An independent, landmark-dominated head-direction signal in dysgranular retrosplenial cortex. *Nat. Neurosci.* **20**, 173–175 (2017). doi: 10.1038/nn.4465; pmid: 27991898
46. C. N. Boccara *et al.*, Grid cells in pre- and parasubiculum. *Nat. Neurosci.* **13**, 987–994 (2010). doi: 10.1038/nn.2602; pmid: 20657591
47. R. Chaudhuri, B. Gerçek, B. Pandey, A. Peyrache, I. Fiete, The intrinsic attractor manifold and population dynamics of a canonical cognitive circuit across waking and sleep. *Nat. Neurosci.* **22**, 1512–1520 (2019). doi: 10.1038/s41593-019-0460-x; pmid: 31406365
48. A. Rubin *et al.*, Revealing neural correlates of behavior without behavioral measurements. *Nat. Commun.* **10**, 4745 (2019). doi: 10.1038/s41467-019-12724-2; pmid: 31628322
49. Z. Ajabi, A. T. Keinath, X.-X. Wei, M. P. Brandon, Population dynamics of head-direction neurons during drift and reorientation. *Nature* **615**, 892–899 (2023). doi: 10.1038/s41586-023-05813-2; pmid: 36949190
50. J. D. Seelig, V. Jayaraman, Neural dynamics for landmark orientation and angular path integration. *Nature* **521**, 186–191 (2015). doi: 10.1038/nature14446; pmid: 25971509
51. A. Rubin, M. M. Yartsev, N. Ulanovsky, Encoding of head direction by hippocampal place cells in bats. *J. Neurosci.* **34**, 1067–1080 (2014). doi: 10.1523/JNEUROSCI.5393-12.2014; pmid: 24431464
52. S. Danilovich, Y. Yovel, Integrating vision and echolocation for navigation and perception in bats. *Sci. Adv.* **5**, eaaw6503 (2019). doi: 10.1126/sciadv.aaw6503; pmid: 31249874
53. G. G. Kwiecinski, T. A. Griffiths, Rousettus egyptiacus. *Mamm. Species* **199**, 1–9 (1999). doi: 10.2307/3504411
54. L. Las, N. Ulanovsky, Bats. *Nat. Methods* **21**, 1135–1137 (2024). doi: 10.1038/s41592-024-02330-6; pmid: 38997589
55. S. B. Childs, E. R. Buchler, Perception of simulated stars by *Eptesicus fuscus* (Vespertilionidae): A potential navigational mechanism. *Anim. Behav.* **29**, 1028–1035 (1981). doi: 10.1016/S0003-3472(81)80056-5
56. H. Mouritsen, O. N. Larsen, Migrating songbirds tested in computer-controlled Emlen funnels use stellar cues for a time-independent compass. *J. Exp. Biol.* **204**, 3855–3865 (2001). doi: 10.1242/jeb.204.22.3855; pmid: 11807103
57. M. Dacke, E. Baird, M. Byrne, C. H. Scholtz, E. J. Warrant, Dung beetles use the Milky Way for orientation. *Curr. Biol.* **23**, 298–300 (2013). doi: 10.1016/j.cub.2012.12.034; pmid: 23352694
58. F. Raudies, M. P. Brandon, G. W. Chapman, M. E. Hasselmo, Head direction is coded more strongly than movement direction in a population of entorhinal neurons. *Brain Res.* **1621**, 355–367 (2015). doi: 10.1016/j.brainres.2014.10.053; pmid: 25451111
59. Y. Yovel, M. Geva-Sagiv, N. Ulanovsky, Click-based echolocation in bats: Not so primitive after all. *J. Comp. Physiol. A Neuroethol. Sens. Neural Behav. Physiol.* **197**, 515–530 (2011). doi: 10.1007/s00359-011-0639-4; pmid: 21465138
60. A. S. Etienne, K. J. Jeffery, Path integration in mammals. *Hippocampus* **14**, 180–192 (2004). doi: 10.1002/hipo.10173; pmid: 15098724
61. A. Cheung, S. Zhang, C. Stricker, M. V. Srinivasan, Animal navigation: The difficulty of moving in a straight line. *Biol. Cybern.* **97**, 47–61 (2007). doi: 10.1007/s00422-007-0158-0; pmid: 17520273
62. M. Geva-Sagiv, L. Las, Y. Yovel, N. Ulanovsky, Spatial cognition in bats and rats: From sensory acquisition to multiscale maps and navigation. *Nat. Rev. Neurosci.* **16**, 94–108 (2015). doi: 10.1038/nrn3888; pmid: 25601780
63. M. R. Loewen, "Laboratory measurements of the sound generated by breaking waves," thesis, Massachusetts Institute of Technology and Woods Hole Oceanographic Institution (1991).
64. G. Koay, R. S. Heffner, H. E. Heffner, Hearing in a megachiropteran fruit bat (*Rousettus aegyptiacus*). *J. Comp. Psychol.* **112**, 371–382 (1998). doi: 10.1037/0735-7036.112.4.371; pmid: 9861710
65. J. Zeil, Visual navigation: Properties, acquisition and use of views. *J. Comp. Physiol. A Neuroethol. Sens. Neural Behav. Physiol.* **209**, 499–514 (2023). doi: 10.1007/s00359-022-01599-2; pmid: 36515743
66. K. Asumbisa, A. Peyrache, S. Trenholm, Flexible cue anchoring strategies enable stable head direction coding in both sighted and blind animals. *Nat. Commun.* **13**, 5483 (2022). doi: 10.1038/s41467-022-33204-0; pmid: 36123333
67. J. P. Goodridge, P. A. Dudchenko, K. A. Worboys, E. J. Golob, J. S. Taube, Cue control and head direction cells. *Behav. Neurosci.* **112**, 749–761 (1998). doi: 10.1037/0735-7044.112.4.749; pmid: 9733184
68. R. S. Heffner, G. Koay, H. E. Heffner, Sound localization in an Old-World fruit bat (*Rousettus aegyptiacus*): Acuity, use of binaural cues, and relationship to vision. *J. Comp. Psychol.* **113**, 297–306 (1999). doi: 10.1037/0735-7036.113.3.297; pmid: 10497795
69. A. Bicanski, N. Burgess, Environmental anchoring of head direction in a computational model of retrosplenial cortex. *J. Neurosci.* **36**, 11601–11618 (2016). doi: 10.1523/JNEUROSCI.0516-16.2016; pmid: 27852770
70. Y. Yan, N. Burgess, A. Bicanski, A model of head direction and landmark coding in complex environments. *PLOS Comput. Biol.* **17**, e1009434 (2021). doi: 10.1371/journal.pcbi.1009434; pmid: 34570749
71. J. J. Knierim, H. S. Kudrimoti, B. L. McNaughton, Place cells, head direction cells, and the learning of landmark stability. *J. Neurosci.* **15**, 1648–1659 (1995). doi: 10.1523/JNEUROSCI.15-03-01648.1995; pmid: 7891125
72. R. Knight *et al.*, Weighted cue integration in the rodent head direction system. *Philos. Trans. R. Soc. London Ser. B* **369**, 20120512 (2013). doi: 10.1098/rstb.2012.0512; pmid: 24366127
73. R. Eilam-Altstädter, L. Las, M. P. Witter, N. Ulanovsky, *Stereotaxic Brain Atlas of the Egyptian Fruit Bat* (Academic Press, 2021).
74. S. Palgi *et al.*, Data for: Head-direction cells as a neural compass in bats navigating outdoors on a remote oceanic island, Zenodo (2025); https://doi.org/10.5281/zenodo.15646845.

ACKNOWLEDGMENTS

We thank D. Derdikman, A. Finkelstein, Y. Ziv, A. Rubin, M. Kirschhock, R. Yerushalmi, and E. Farber for comments on the manuscript; S. Zikankuba, M. Mwanzalila, A. Massa, K. Kingojo, C. Haule, L. Rufino, M. Martinengo, J. Alexiou, G. Ginosar, M. Weinberg, K. Krivoruchko, M. Guggenberger, S. Forer, G. Omarch, S. Stephen, F. Essajee, H. Essajee, E. Kopf, S. Molcho, and S. Mazaki for assistance in the fieldwork, boat transportation to the island, work at TVLA, and logistical support; A. Shalev, N. Tzuri, M. Brezins, A. Pilewski, and G. Cohen for help in bat training and assistance in Israel; B. Pasmantirer, G. Ankaoua, and A. Jahanfard for mechanical designs and manufacturing; R. Tumasus, C. Ra'anan, and R. Eilam for histology; M. P. Witter for advice on histological delineation of dorsal presubiculum and retrosplenial cortex; and G. Brodsky for graphics. **Funding:** N.U. is the incumbent of the Barbara and Morris Levinson Professorial Chair in Brain Research. This study was supported in part by research grants to N.U. from the European Research Council (ERC-Advanced NEURO_OUTDOORS and ERC-Consolidator NATURAL_BAT_NAV); by research grants to N.U. and L.L. from the National Institutes of Health (NIH R01 – NS121413), CRCNS NSF-BSF (BSF 2020806), and the Israel Science Foundation (ISF 1829/23); by research grants to N.U. from the Weizmann Center for the Development of Innovative Neurotechnologies, Zuckerman Center for Learning Memory & Cognition, Center for Research on Perception and Action, Dr. Lou Siminovitch Laboratory for Research in Neurobiology, Dorraine S. Schwartz, Debra and Paul Sagues, and Yehuda and Judith Bronicki; by a research grant to H.M. from the European Research Council (ERC-SyG–Quantum Birds); a Deutsche Forschungsgemeinschaft collaborative grant to N.U. and H.M. (DFG no. 395940726, SFB 1372 "Magnetoreception and navigation in vertebrates"); and by the André Deloro Prize for Scientific Research and the Kimmel Award for Innovative Investigation to N.U. S.P. was supported by an Azrieli Brain Science fellowship for excellent PhD students; and S.R. was supported by postdoctoral fellowships from the European Molecular Biology Organization (ALTF 853-2017) and the Human Frontier Science Program (LT000365-2018L). **Author contributions:** N.U. conceived of this study in 2018 while scuba diving on a remote oceanic island. S.P., S.R., S.R.M., L.L., and N.U. designed the experiments. S.P., S.R., S.R.M., T.E., L.L., and N.U. developed technology, set up experimental systems, and conducted technical preparations for the island experiments. J.D.K. and A.I.A. obtained research permits and assisted with logistics. S.P., S.R., A.T., C.C., L.L., and N.U. performed preparations on the mainland and conducted the experiments on the island. S.P. performed the data analysis of the island experiments, and S.R., Y.W., and L.B.-A. contributed to the data analysis. S.R.M. and H.M. conducted the magnetic manipulation experiments in the tunnel, and S.R.M. analyzed the data from these experiments. N.U. guided all the data analysis, with major input from L.L. S.P and N.U. wrote the first draft of the manuscript, with major input from S.R., S.R.M., and L.L. All authors participated in writing and editing the manuscript. N.U. supervised the project. **Competing interests:** The authors declare that they have no competing interests. **Data and materials availability:** The data and code that support the conclusions of this study are freely accessible online at Zenodo (74). This research was funded in whole or in part by the European Research Council (ERC-Advanced NEURO_OUTDOORS, ERC-Consolidator NATURAL_BAT_NAV, and ERC-SyG–Quantum Birds); as required the author will make the Author Accepted Manuscript (AAM) version available under a CC BY public copyright license.

SUPPLEMENTARY MATERIALS

science.org/doi/10.1126/science.adw6202
Materials and Methods; Supplementary Results; Figs. S1 to S20; References (75–99); MDAR Reproducibility Checklist

Submitted 10 February 2025; accepted 22 August 2025

10.1126/science.adw6202

Science
AAAS

Supplementary Materials for

Head-direction cells as a neural compass in bats navigating outdoors on a remote oceanic island

Shaked Palgi *et al*.

Corresponding authors: Liora Las, liora.las@weizmann.ac.il; Nachum Ulanovsky, nachum.ulanovsky@weizmann.ac.il

Science **390**, eadw6202 (2025)
DOI: 10.1126/science.adw6202

The PDF file includes:

Other Supplementary Material for this manuscript includes the following:

Materials and Methods

Subjects and behavioral setup

Subjects. Eight adult male Egyptian fruit bats, *Rousettus aegyptiacus*, were included in this study as subjects for electrophysiological recordings (weights 149–182 gr) – six bats for experiments on the island in Tanzania, and two bats for experiments in Israel. All eight bats were caught as adults in the wild. The six bats that were used for recordings on the island were caught in the Dar es Salaam region, in East Africa (Fig. 1F). Five of the 6 bats were captured at a sea cave, located right on the seashore of the Indian ocean: as this cave is partially flooded during high tides, these bats were used to living close to the sea, and were accustomed to the sounds and odors of sea-waves and sea birds (the sixth bat was captured in the Dar es Salaam city center, less than 2 km from the seashore). All experimental procedures were approved by the institutional animal care and use committee (IACUC) of the Weizmann Institute of Science (IACUC approvals no. 09371222-2 and 00720124-2), as well as by research permits from the Tanzania Commission for Science and Technology (COSTECH permits no. 2022-195-NA-2022-095 and 2023-790-NA-2022-095) and the Zanzibar Research Committee (permits no. 6347BFFA86F61 and 200171024928054725 1255). Two additional bats were caught in Israel and were used in the tunnel experiment in Israel (IACUC approval no. 05500622-2), described below in the section "Magnetic field manipulation in the flight-tunnel", as well as in the Supplementary Results, and in fig. S20. All other sections below describe the methods that were used for the island experiments and analysis.

Training. Bats were minimally trained for ~1 week to get used to handling by humans, and to recognize specific feeding-platforms as a source for food. Further training was done post-surgery, to accustom the bats to the implant. Initial training (before surgery and a few days after surgery) was performed in a large flight room (size 5.1 × 3.6 m) on the mainland (at the Tanzania Veterinary Laboratory Agency [TVLA] in Dar es Salaam). Later, upon arriving to the island, the training continued in a large tent (fig. S19A, size 5.0 × 3.5 m). The walls of this flight-tent were

netted, allowing the bats to experience the natural environment of the island – including sounds, odors, and wind – prior to the bats' release outdoors on the island. Bats were fed with fresh fruits *ad lib* in their roost, which consisted of several large soft cages (size 90 × 75 × 40 cm for each cage; 3–4 bats per cage); on the island we placed these cages inside an air-conditioned tent (size 2.5 × 2.5 m), where the bats spent most of the day and night, except for training and the experimental recording periods.

Setup. To successfully record bats outdoors, we created conditions which discouraged the bats from escaping. Therefore, we chose a remote island in the Indian Ocean – Latham Island – located ~50 km from the closest shore of mainland Africa and ~70 km from the closest shore of Zanzibar. This island is completely barren, without any trees or natural food sources for these fruit bats – which encouraged the bats to remain close to their known environment (e.g. their roost) in order to get food. This island is not a natural reserve or a protected area, and is visited occasionally by local fishermen who camp there for short periods. The main local animals on the island are a few species of sea birds, which are used to the occasional human presence. Importantly, these birds are all diurnal, and therefore they were inactive at night when the experiments were conducted. Due to weather limitations, we had a short window of 3–4 weeks every year to conduct recordings on the island. We released 1–2 bats each night, and each bat was recorded for several nights, with recordings starting from their first exploration of the island. The data in this manuscript were collected during two experimental seasons in two consecutive years. To prevent cases of bats escaping from the island, we positioned a small fast boat on the water during the experiments, which allowed capturing bats that landed on the water surface – as these bats are excellent swimmers, and floated on the water after landing there (this happened twice during the experiment; after these escape attempts we stopped releasing those two specific bats). This boat did not have any lights, and was invisible from the island, and thus could not serve as a directional cue. Light levels outdoors at night were measured using a high-end portable light meter (Gigahertz Optik P-9710-1, with VL-

3707-2 light detector), and ranged between 0.001 and 0.15 lux, depending on moon state: we note that bats of this family have excellent vision, and can see well down to light levels of 10^{-5} lux (*62*). The weather on the island was clear, without fog or haze, although there was cloud coverage on some of the nights, which transiently masked the moon and the stars. In addition to the bats' roost and human camp (i.e. tents), we added two feeding platforms (Fig. 1I, height = 180 cm). The platform locations remained fixed for most of the experiment, with one exception during the second experimental season: one platform had to be relocated after a few days, due to changes in the location of the sand bank. We note that apart from the release moment, the human experimenters typically did *not* stand near the platforms, but rather stayed > 20 meters away from them.

Behavior – Outdoor flight. Bats were encouraged to fly outdoors from multiple release locations. No other type of behavior or task was explicitly encouraged by the experimenters. As a result, we observed a variety of flight behaviors, ranging from long exploratory flights over a large area, to more directed flights – with many flights covering long distances, but also with many short local flights. Overall, the median flight distance was 99.7 m (interquartile range [25–75%] of flight distance: 39.1–210.3 m; n = 301 flights in 6 bats; see details below on flight-segmentation). This variability in exploratory behavior was seen both across different animals and within individual animals (i.e. across different sessions). In total we conducted in this study n = 22 recording sessions from 6 bats. The vast majority of the data were recorded during night sessions (n = 18 night sessions, from all 6 bats). In these sessions, we mostly released the bat from two platforms, which remained stationary throughout the session. In some of the night-sessions we also released the bat from the experimenters' hand after walking to a random location. In cases when a bat landed not on a platform, we carried it back to one of the platforms, or to a new random location. Sessions lasted typically ~30–50 min and included multiple flights. On some nights (n = 5), we performed another session after a gap of a few hours, allowing us to record the same neurons across different environmental conditions – with moon vs. without moon (these double-sessions were counted as one

session in the overall counting of n = 18 night-sessions). In two bats, we also conducted a few daytime sessions, as an early pilot study (n = 4 daytime sessions; these sessions were shorter than the night sessions, and did not have platforms at fixed locations). Overall, during these 22 recording sessions outdoors, the 6 bats flew a total of 301 flights.

Behavior – Indoor flight. In 4 bats, we added indoor recording sessions, which were conducted in the same tent used for training (fig. S19A). These indoor sessions (n = 7) were conducted immediately before the main outdoor flight sessions. The tent was illuminated inside (illuminance level ~ 1 lux), and it contained multiple objects (electrical cables, lamps, etc.); and in addition we placed two landing-platforms of the same type as used outdoors: the platforms were placed in the two opposite corners of the tent. The tent was built from cloth and was therefore transparent to GPS signals; hence we could use the same recording devices to extract the animal location both indoors and outdoors. In the indoor sessions, the bat was released from one of two landing platforms, or from random locations on the tent perimeter (in order to increase angular coverage). No attempts were made to disorient the bat. The indoor sessions lasted ~15 minutes. After these indoor sessions, the bat was allowed to rest in a small carrying cage for ~5 minutes, and was then transported inside this cage to the release location outdoors – where the outdoor session started after a short delay of a few minutes.

Neural and behavioral recordings using the neural logger

All recordings were done using a recently developed new type of neural logger (Deuteron Technologies, Israel), which allows conducting wireless recordings of neural signals, together with measurements from additional on-board behavioral sensors, including GPS and altimeter (Fig. 1A). All the sensors were synchronized on-board to each other and to the neural recordings, at a microsecond temporal precision, and were later resampled to match the GPS sampling rate. The GPS was used here for horizontal (XY) localization and for computing heading-direction; the

altimeter was used for vertical (Z) localization; the GPS, accelerometer, and altimeter were used together to classify behavior into behavioral modes; and the magnetometer and accelerometer were used together to extract head-direction during stationary non-flight periods. See further details below on the use of these sensors.

Neural recordings. Data from the neural logger's 64 channels were amplified (×200), bandpass filtered (1 – 7,000 Hz), and then sampled continuously at 32 kHz per channel and stored on board the logger. We later applied a high-pass filter with a cutoff frequency of 600-Hz, creating a bandwidth of 600 – 7,000 Hz for spikes.

GPS. We used a high-end global navigation satellite system module (on-board chip: NEO-M9N, u-blox, Switzerland), which sent data directly to the logger for storage. This modern chip utilizes the signals received from four different global navigation satellite systems (GNSS; these 4 systems are: GPS – United States, Galileo – European Union, BeiDou – China, and GLONASS – Russia). This allows for a high number of visible satellites, yielding high localization accuracy (see below). Moreover, this chip allows a very high sampling rate of 25 Hz. We only analyzed data with ≥5 visible satellites, but often observed 12–16 satellites. For consistency with laboratory-based experiments, we converted the GPS latitude and longitude values into meters, using a local reference frame (X = east, Y = north, Z = up). The origin coordinate (X,Y)=(0,0) [labeled as a yellow '+' in fig. S3A-B] was taken as the western-most and southern-most points that any of the bats visited during flights outdoors (excluding two long flights above the sea). We used here only the X,Y coordinates of the GPS; for the Z data we used altimeter measurements, which are more precise than GPS (see below). We validated our GPS accuracy via a calibration procedure: we compared the GPS readings to a local ultra-wideband radio-based localization system in our laboratory in Israel, which yields a high accuracy of 5 cm. The comparison was done by driving an electric scooter in complex trajectories, while carrying both the ultra-wideband radio-frequency tag

– which served as ground-truth – and the neural logger with GPS; this comparison yielded positional errors with an SD of 71 cm (Fig. 1B), and angular errors with an SD of 3.3° (Fig. 1C).

Accelerometer. We used a 3-axis accelerometer (part of an on-board 9-axis motion sensor: Invensense MPU-9250, 1-kHz sampling rate) as an additional sensor for classifying behavior. Specifically, we utilized the fact that as bats fly, their wingbeats create a periodic acceleration signal along the Z axis (see below).

Magnetometer. We used the on-board magnetometer to extract head-direction during non-flight stationary periods, when the GPS cannot provide directional information (in Fig. 1R we also used the magnetometer for comparing head- to heading-direction in flight). We recorded the Earth's magnetic field using a 3-axis magnetometer (part of the same chip as the accelerometer), at a sampling rate of 1 kHz. We first applied a low-pass filter with a cutoff frequency of 10 Hz to the data from each of the 3 axes, and calibrated them using a standard magnetic calibration algorithm (Matlab's *magcal*; calibration was performed in windows of 15 minutes). To extract the head-direction from the magnetic field, we used a standard algorithm (Matlab's *ecompass*), which integrates the readings from the 3-axis accelerometer (which senses the Earth's gravity) and the 3-axis magnetometer (which senses the Earth's magnetic field) – and produces a rotation matrix that reflects the orientation of the bat's head relative to the Earth's surface and the Earth's magnetic north. The resulting rotation-matrix was smoothed using the SLERP algorithm (*75*), applied in forward and reverse to avoid filter lag. The bat's head-direction was then calculated from the smoothed rotation matrices (using Matlab's *eulerd*). We did not apply any correction to the magnetometer data, which points to the magnetic north and not to the geographic north – because on Latham Island, the difference between the magnetic and geographic north (termed the magnetic declination) is only 2° (*76*), which is within our angular error range.

Altimeter. We recorded the ambient atmospheric pressure around the bat using a high-end miniaturized altimeter (ST LPS22HB), at a sampling rate of 77 Hz. The pressure measurements were later converted into meters above mean sea-level (altitude, or height) using pressure-altitude

equations. Since the pressure signal changes with the dynamic atmospheric conditions, we calibrated the altitude separately for every flight, by subtracting the baseline at the beginning of each flight. This baseline was defined as the median height during up to 10 seconds preceding each takeoff, in which the behavior was strictly stationary (speed < 0.5 m/s). We then converted it to the bat's altitude above mean sea-level, by adding the ground-level at the release-location, which was taken from the digital elevation map of the island (measured from the drone photos, see below). We validated the accuracy of the altimeter measurements via a calibration procedure: we compared the height-readings to precisely known heights at the Weizmann Institute in Israel (using a tape measurement for small-scale calibration, and an elevator for large-scale calibration of the altimeter in a building with precisely-known floor heights). We found the error to be within 10 cm precision over 30 seconds. Since most of the bats' flights lasted no more than 30 seconds (the 50th percentile of flight-duration was 19 seconds, and the 90th percentile of flight-duration was 56 seconds), we estimate that the precision of our altitude measurement was typically between 10 and 20 cm, and almost always better than 30 cm.

Environmental measurements

Wind. Wind speed and direction were logged by a small meteorological station (Kestrel 5500, Nielsen-Kellerman, USA), at intervals of 10 seconds (n = 16 sessions) or 1 hour (n = 5 sessions; 1 session did not include wind measurements). For consistency with the rest of the angular variables, wind direction was defined as the direction towards which the wind was blowing.

Moon. We logged the moon visibility (visible/invisible) during the experiment every few minutes, synchronized to the neural-logger recordings. The moon could be invisible due to two main factors: (1) sessions started before moonrise or after moonset (i.e. the moon was below the horizon); or (2) temporary occlusions due to heavy cloud coverage. For any moon related analysis, we only used epochs where the moon stayed for at least 2 minutes in its visible/invisible state (this removed

0.66% of the data). In the majority of nights (n = 11 out of 18 nights) there was not enough time-spent in both 'with moon' and 'without moon' conditions to allow comparison; we thus compared this only in 7 nights (across 4 different bats). Moon direction in spherical coordinates was calculated using standard astronomical databases (*77*). We note that the moon did not exhibit large enough movements across the sky within a session to allow analyzing whether neurons track the moon-direction on a fine temporal scale (fig. S8E); therefore, in this study we analyzed neuronal responses either on a coarse temporal scale, namely with respect to the moon's median direction in a session (fig. S8F) – or we compared neuronal tuning with moon vs. without moon (Fig. 4).

Drone photos of the island. We used a drone (DJI Air 2S) to take aerial photos of the whole island. These images were later stitched together and geotagged using a specialized software (DroneDeploy, USA) – yielding one photo (map) with a 2-cm pixel resolution for the entire island. Prominent landmarks on the island were chosen as calibration points, where we performed static GPS measurements using our GPS loggers in order to later match the drone-photos to our GPS recordings of the bats. We used this high-resolution map to define the island shoreline (fig. S3A-B), which we then further split to the west shore and south shore (fig. S3D). In addition to a high-resolution map of the island, drone photography allowed obtaining a high-resolution elevation map of the island (fig. S3E; also known as 'digital elevation model'): This elevation map was then used to compute the bat's flight-altitude above ground, and the optic flow (see below). As the island's sandbank was slowly changing over time (on a timescale of weeks), we repeated the drone photography of the island every 2–3 days: For each neural recording session outdoors, we used the drone map and shoreline data that were taken closest in time to the recording session.

Surgery

All surgeries were conducted on Tanzania's mainland, at the Tanzania Veterinary Laboratory Agency (TVLA) in Dar es Salaam, where we established a surgery room similar to the one used at the

Weizmann Institute in Israel — including high-end air-conditioning system (HVAC), digital stereotax, surgical microscope, etc. This allowed us to perform all the surgical procedures at TVLA as described previously (*22, 78, 79*). In brief, we implanted the bats with a custom 16-tetrode microdrive (modified from ref. (*80*)), loaded with individually-moveable tetrodes, made from 4 platinum-iridium wires (17.8 μm diameter insulated wire; California Fine Wire, USA). All tetrodes were gold-plated to reduce their impedance to 0.3 MΩ at 1 kHz. The microdrive was implanted above the right dorsal presubiculum (known also as 'postsubiculum') – a key hub of the head-direction system in mammals, known to harbor head-direction cells in both rodents (*14, 15, 25*) and bats (*22*) – at the following stereotaxic coordinates: 3.3 mm lateral to the midline and 3.15 mm anterior to the transverse sinus that runs between the posterior part of the cortex and the cerebellum (*22, 73*). Bats were anesthetized using an injectable anesthesia cocktail composed of medetomidine (0.08 mg/kg), midazolam (2.5 mg/kg), fentanyl (0.025 mg/kg), and ketamine (17 mg/kg) (*81*). Additional injections were administered as needed, based on the bat's breathing and heart-rate. The craniotomy was covered with an inert silicone elastomer (Kwik-Sil), and the microdrive was attached to the skull with bone screws, using a layer of adhesive (Super-Bond C&B) followed by dental acrylic. We attached the ground wire from the microdrive to a bone-screw that touched the dura in the skull's frontal plate. Meloxicam analgesia was administered towards the end of the surgery, and for additional 5 days; we also administered dexamethasone for 2 days post-surgery, and enrofloxacin antibiotics for 7 days post-surgery.

Following surgery, the tetrodes were slowly lowered towards the dorsal presubiculum. Neuronal activity during this period was monitored using a portable wired electrophysiology system (LabLynx, Neuralynx, USA). One to two weeks after surgery, the bats were taken by boat to Latham Island, where the wireless neural recordings were conducted. While on the island, we continued to slowly advance the tetrodes down, typically by 20–80 μm daily, using the same wired-electrophysiology system (LabLynx). This daily advancement of tetrodes allowed recording new neurons every day (although it is possible that some neurons were recorded more than once). Tetrode positioning was later verified histologically (see below).

Spike sorting

Spike sorting was done as previously described (*78, 79*). We first detected candidate spikes using a voltage threshold on the filtered neural signal, and extracted 1-ms waveforms around each peak on all the 4 channels of each tetrode. We then used Plexon Offline Sorter to manually sort putative waveforms into isolated clusters, based on the relative amplitudes of the 4 channels in each tetrode. Spike sorting was done in consecutive short time windows, to allow us to account for electrode-drift. We additionally required a refractory period of 2-ms in the spike autocorrelation (e.g. Fig. 1D, right). Data from all the behavioral sessions of the same night were spike-sorted together – including the indoor flight session, outdoor flight session, and rest-period in the cage – and this was the case also in the nights when we recorded two sessions for the same bat with a ~2 hours break between them (with/without moon). In all cases, only clusters which exhibited stability in their physiological characteristics (i.e. stable waveform shape, spike autocorrelation, and inter-spike-interval histograms) were defined as the same neuron.

Inclusion criteria for analyzing neurons: In total, we recorded 462 well-isolated neurons, from 6 bats. Out of these, we further analyzed 406 neurons which passed the following four inclusion criteria: (1) the neuron fired >30 spikes during flight, (2) had >40 seconds of flight time, and (3) had enough behavioral coverage of direction (see below). (4) The tetrode track for that neuron was anatomically localized to dorsal presubiculum or retrosplenial cortex, based on the histological sections.

Histology

Histology was done as described previously (*78, 79*). At the end of the recordings on the island, the bats were transported to the mainland, to TVLA, where they were anesthetized, and electrolytic lesions were made (positive DC current of 30-μA for 15-s) to assist in reconstructing the electrode (tetrode) tracks. We then perfused the bats transcardially with the tetrodes kept *in situ* (using

phosphate buffer saline followed by 4.5% histofix), and the brains were then extracted and post-fixed in 4.5% histofix. We then shipped the brains to Israel, and later cut the brains into coronal sections (40 μm thickness), which were Nissl-stained with cresyl violet, and photographed at high resolution using a slide-scanner (VS120, Olympus) to determine the locations of the tetrode tracks. Most of the tetrode tracks were in the dorsal presubiculum, but some tracks were in the adjacent retrosplenial cortex, based on a previously defined anatomical delineation (*73*). We recorded head-direction cells in both regions (59 of 97 head-direction cells were recorded in presubiculum and 38 in retrosplenial cortex) – and since the properties of the head-direction cells from both regions were found to be similar, we pooled together the data from both of these brain regions.

Computing behavioral variables

In addition to the directly measured positional variables – the bat's horizontal XY position (based on the GPS) and the bat's Z altitude (based on the altimeter) – we computed several additional behavioral variables.

Velocity and speed. The horizontal XY position was first smoothed using a smoothing spline (Matlab's *csaps*, X and Y smoothed separately), and the first derivative of the smoothed trajectory was calculated at each point and divided by the time difference between measurements, to yield the horizontal velocity. Speed was calculated using the horizontal XY velocity (we neglected the vertical Z velocity, which was much smaller). We used a speed threshold as one of the main criteria for defining flight epochs (see below).

Heading direction. The horizontal velocity vector was used to calculate the bat's heading direction during flight (azimuth), using the inverse tangent of the X and Y velocities. We defined 0° to be north, with angle advancing clockwise (i.e. 90° = east, 180° = south, and 270° = west). We used the azimuthal heading-direction as a proxy for head-direction throughout the paper (except Fig. 2E-F and fig. S9, see below), because: (i) heading-direction was shown to be highly

correlated with head-direction in freely flying Egyptian fruit bats (*59*); (ii) heading-direction and head-direction were highly correlated in our own data in bats flying outdoors (Fig. 1R; circular-circular $\rho = 0.88$); (iii) heading-direction (using the GPS) permitted a very precise directional estimate, with a 3.3° directional accuracy (Fig. 1C) and high reliability in all sessions; and (iv) head-direction measurement (using the magnetometer) was less reliable because the magnetometer did not work properly in some of the sessions.

Pitch. Pitch (vertical angle) was computed in a similar manner to azimuth. We first calculated the vertical velocity based on the altimeter signal, and defined pitch as the inverse tangent using this vertical velocity and the horizontal speed (positive pitch was defined as flying upwards). We found that, under the conditions of these experiments on the island, the bats flew quite horizontally and exhibited a very limited range of pitch angles in-flight (fig. S5C) – and therefore we did not compute neuronal tuning to pitch, and focused our analysis of the neurons' directional tuning only on the bat's heading-direction in the horizontal plane.

Angular velocity and angular acceleration. Angular velocity was computed using the difference between two consecutive heading-direction values. Positive angular velocity was defined as turning clockwise. Angular acceleration was computed using the difference between two consecutive angular velocity values.

Radius of curvature. Radius of curvature is a standard metric for the local straightness of trajectories in space, at each point along the trajectory – where a large radius indicates a straight flight, while a small radius indicates a sharp turn. We computed the instantaneous radius of curvature using the following formula:

$$r = \frac{(x'^2 + y'^2)^{3/2}}{|y'x'' - y''x'|}$$

Where x and y denote position, x' and y' denote the 1st temporal derivatives, and x'' and y'' denote the 2nd temporal derivatives.

Altitude above ground. As explained above, we used pressure-altitude equations to extract the bat's altitude above mean sea-level at every moment (Fig. 1L, left panel). To estimate the flight altitude above ground (Fig. 1L, right panel), we subtracted from the altitude-measurement the ground-elevation at the same location – as measured from the drone-based digital elevation map (e.g., fig. S3E). These three sets of measurements (GPS logger, altimeter, drone-based elevation map) were calibrated and aligned to one unified coordinate system by measuring prominent landmarks on the island using the three systems.

Optic flow. We chose a simple definition of optic flow, which nonetheless captures the qualitative characteristics of this metric – namely, as the bat flies twice as fast, the optic flow should be twice as large, and as the bat flies twice as high, the optic flow should be half. Therefore, we defined optic flow at every moment as the ratio between the bat speed and its height (altitude) above ground:

$$Optic\ flow\ (s^{-1}) = \frac{speed}{height}$$

Context. The most prominent contextual variable in our experiments was which platform the bat took-off from. We therefore defined for each flight the 'context' as the identity of the platform from which it took off. This allowed us to assess whether starting from different spatial positions anchors the bat's reference frame to different cues – and potentially creates different directional tuning for the two start-platforms. Context was defined only for flights where the bat was released from one of the two platforms.

Behavioral segmentation

For the outdoor sessions, we split the data into two behavioral modes: Flight epochs and stationary epochs.

Flight epochs outdoors were identified based on a combination of four criteria:
(1) Flight speed >2 m/s (nevertheless, we also included up to 2 seconds of flight data at speeds between 0.5 m/s and 2 m/s – in order to capture the cases of sharp flight maneuvers, such as U-

turns, where the speed briefly dropped below 2 m/s). (2) We required a clear wingbeat-rate signal in the Z-axis of the accelerometer – evident by high power in the 6–8 Hz frequency band. (3) Occurrence of fast changes in altitude in the altimeter signal, which correspond to takeoffs and landings. (4) Flight duration ≥ 2 seconds.

Stationary epochs outdoors were defined as: (1) non-flight epochs where the speed was < 0.5 m/s, and (2) there was no clear periodic signal in the Z-axis of the accelerometer. For the analysis of head-direction tuning during stationary behavior (Fig. 2E-F, fig. S9), we only used epochs when the bat was upright (with head pitch angle < 75°), based on the accelerometer.

Indoor flights (inside the flight-tent) were identified using a modified set of criteria, as follows (we adjusted the criteria because bats tended to fly slower inside the flight-tent than during outdoor flight; the typical flight-speed indoors was < 2 m/s): (1) The speed threshold for defining flights indoors was set to > 0.3 m/s. (2) The U-turn minimal speed threshold was relaxed, to include any brief decrease in speed (up to 2-s in duration). (3) Wingbeat amplitude (defined as the magnitude of the Hilbert transform of the Z accelerometer signal, filtered between 6–10 Hz) was > 2 m/s^2. (4) Flight duration ≥ 2 s.

Calculation of area covered per night

To quantify the spatial area that the bats covered in each session (Fig. 1M, Fig. 3N-O), we defined the 'concave hull' of all the trajectories in that session. We used Matlab's *boundary* function, with the default shrinkage parameter of 0.5 (see the pink outlines in fig. S3C). We opted not to use the more common convex hull, as this metric can over-estimate the covered space, especially when the trajectories are curved and complex. For example, for the session plotted in the right panel of fig. S3C, the convex hull would artificially include a triangle above the central plateau, which the bat did not actually visit in this session.

Quantification of directional tuning curves

Directional neural tuning. One-dimensional directional (azimuthal) tuning curves were calculated throughout this study using the heading-direction, by binning the spikes and the directional behavioral data into angular bins; then dividing the per-bin spike count by the per-bin time spent, to obtain firing-rate; and then smoothing the result with a 3-bins rectangular window (with smoothing performed in a circular manner). The number of angular bins varied slightly between different analyses, to account for the different amounts of data in each analysis: We used 16 angular bins for the full directional tuning curves (based on all the data: e.g., Fig. 2C) and 12 angular bins elsewhere (where we subdivided the data; see below; e.g., Fig. 3A-bottom). A minimal time-spent of 1-s was required in each angular bin to be considered as a valid bin.

Von-Mises fit. To obtain reliable estimates of tuning-curve parameters, such as preferred direction and tuning-width, we fitted a modified von-Mises function (an analog of a Gaussian function for circular variables) to each directional tuning curve, and used the fitted function to calculate all the relevant metrics (*82, 83*). The fitted function was of the following form:

$$r(\theta) = Ae^{\kappa \cos(\theta-\alpha)} + C$$

Where $r(\theta)$ is the firing-rate r as a function of θ, the angle in radians. A, κ, α and C are the 4 parameters of the model. α, the direction which maximizes this function, was taken as the preferred direction of the tuning. We only used valid fits, which passed all of the following criteria: (1) at least half of the bins were valid (namely, had behavioral time-spent > 1 s); (2) there was no large block of consecutive missing bins (< ¼ of the total number of bins); and (3) the fitted peak was at most 1-bin away from a valid bin. Tuning curves which did not pass these criteria were discarded from further analysis. This could potentially discard whole neurons (thus decreasing the number of significant head-direction cells) or discard the neuron only from specific analyses (e.g. from some of the bisection analyses, see below).

Rayleigh vector length. We used the Rayleigh vector length (RV), a metric commonly used to classify head-direction cells, to assess the directionality of the neuron's directional tuning curve (*84*):

$$RV = \frac{\sum_{j=1}^{n} e^{-i\theta_j} r(\theta_j)}{\sum_{j=1}^{n} r(\theta_j)} \cdot \frac{\pi}{n \sin\left(\frac{\pi}{n}\right)}$$

Where θ_j is the angle in radians of the j^{th} circular bin, and $r(\theta_j)$ is the fitted von-Mises function, re-sampled using $n = 100$ bins (we resampled the fitted von-Mises function at 100 equi-spaced angles).

Tuning width. Tuning width at half height (the width at half-height between the baseline [minimum firing-rate] and the peak [maximum firing-rate]) was calculated based on the fitted von-Mises functions, using the following analytic formula:

$$width = \left| 2 \operatorname{acos}\left(\frac{\ln(\cosh(\kappa))}{\kappa} \right) \right|$$

Where *acos* is the inverse cosine function and *cosh* is the hyperbolic cosine function. Note that the width depends only on the concentration parameter κ.

Stability. We computed three measures of functional stability, all based on splitting (bisecting) the data into two equal parts, calculating directional tuning curves separately for the two halves, and computing the Pearson correlation *r* between the two curves (see Fig. 2D). We performed three types of bisections: (1) 1st half of the session vs. 2nd half of the session; (2) even minutes vs. odd minutes in-air; and (3) median of random bisections: here we performed 1,000 random bisections, where we randomly split 10-s epochs in-air into two equal groups, and took the median value of the resulting 1,000 Pearson correlation scores. This random bisection score (option no. 3) was defined as the neuron's stability score, and was used as an inclusion criterion when classifying head-direction cells (see below).

Classification of head-direction cells

Significant head-direction cells were classified as neurons which met all four of the following inclusion criteria, during flight outdoors: (1) Significant Rayleigh vector length: higher than the

95th percentile of the null distribution (spike-shuffle distribution), obtained by computing the Rayleigh vector lengths for 1,000 rigid shuffles of the spikes of the same neuron (where the spikes in-flight were rigidly and circularly shifted relative to the flight behavioral data, with the time shift drawn randomly from a uniform distribution, with a minimal shift of 20 seconds and a maximal shift of the session-duration minus 20 seconds). (2) Rayleigh vector length > 0.1. (3) Good von-Mises fit: explained variance of $R^2 > 0.7$ for the von-Mises fit – indicating clear unimodal directional tuning. (4) Stability score (see above): Pearson $r > 0.3$.

For analyzing head-direction cells during *stationary* behavior outdoors (Fig. 2E-F, fig. S9), we included those head-direction cells – as defined during flight outdoors – which also (i) had enough data during stationary periods (i.e. had a valid directional tuning-curve), and (ii) had RV > 0.1 during stationary periods. This yielded 53 neurons that were valid for this analysis.

To define head-direction cells during flight *indoors* (inside the flight-tent: fig. S19), we used a similar spike-shuffling procedure as in the outdoor condition (but with a minimal time shift of 5 seconds). In fig. S19 – comparison of tuning indoors vs. outdoors – we analyzed only cells which were significant head-direction cells either outdoors *or* indoors, as long as they had RV > 0.1 in *both* conditions – this symmetric definition allowed for unbiased comparison between directional tuning curves during flight outdoors vs. flight indoors ($n = 19$ neurons were valid for this comparison).

Spatial stability of directional tuning: bisections

We performed several types of functional bisections (see details below) wherein we split the data into two parts, computed directional tuning curves for each part, and then compared these two tuning-curves (we used here 12 angular bins to account for the reduced amount of data). Comparisons were done using five parameters (see e.g. fig. S11B-F, each panel here is based on one of these five parameters): (1) the Pearson correlation r (tuning correlation) between the two halves; (2) the difference in the preferred direction angles (ΔPreferred direction); (3) the absolute value of this difference (Abs.

Δpreferred direction); (4) the absolute normalized difference (Abs. normalized Δpreferred direction, defined as the absolute difference in preferred direction between the two halves normalized by the neuron's overall tuning-width); and (5) the difference in tuning-width (ΔWidth). To test the stability of the neurons across the bisections, each of these parameters was tested using an appropriate statistical test, such as Rayleigh test for uniformity (for ΔPreferred direction), or Wilcoxon signed-rank test against 90° (for Abs. Δpreferred direction) or against r=0 (for the tuning correlation); see details in the figure-legends and in the 'Statistics' section below. In addition, all these parameters – except ΔWidth – were also compared to a population shuffle ('cell shuffling'), where the values of each neuron were compared to the values of all *other* neurons (comparing the first half for neuron i vs. the second half for neuron j, for $i \neq j$). For each bisection, we included only neurons that in each half of the data: (i) fired at least 30 spikes, and (ii) had a valid von-Mises fit for the tuning curve (see above, subsection 'von-Mises fit', for the validity criteria). Specifically, we tested the following functional bisections (see Fig. 3A-D, and figs. S10–13):

Spatial bisection. This was bisection along the long axis of the behavioral spatial coverage. To estimate the long axis, we used principal components analysis (PCA) to project the trajectories onto their first principal component (equivalent to the most elongated axis), and bisected them perpendicular to this line. This procedure ensures that the two halves have the maximal variance in their positions (examples: Fig. 3A and fig. S10-leftmost column; population: Fig. 3B-left, and Fig. 3C-D, left boxplot in each panel).

Distance to platforms. Bisection based on distance to the closest platform (this could be *any* of the two platforms; examples: fig. S10, second column from the left). This bisection was performed on all the n = 18 night-sessions, in which the platforms had a fixed location (but not on the n = 4 daytime-sessions, as the platforms did not have fixed locations during these pilot sessions).

Distance to shore. We used the aerial map (drone photo) of the island to extract the shoreline (as shown in fig. S3A-B), and then bisected the data based on the distance to the closest shore – close to shore vs. far from shore (examples: fig. S10, third column from the left).

Closer to the West / South shore. As our bats flew mostly in the south and south-west parts of the island (see fig. S3D), we examined whether the head-direction tuning was anchored to the south or west shorelines, which are rotated about 90° relative to each other. We split the data based on the distance to the closest point in each shoreline, and allocated each time-point to one of the two shorelines based on which shoreline this point was closer to (examples: fig. S10, rightmost column; population: Fig. 3B-right, and Fig. 3C-D, right boxplot in each panel; note that unlike the other bisections, this is not strictly a 50/50% bisection of the data). We removed from this analysis 5 outlier flights: three flights where bat 1 flew mostly over the east part of the island, and two flights where bats 3 and 6 each flew a long flight over the sea (in fig. S3D these 5 flight-trajectories are marked in light color).

Non-spatial bisections. We further tested the stability of the directional tuning-curves to 8 additional functional bisections, based on the following 8 behavioral variables (all of which were defined above): speed, altitude above mean sea-level, optic flow, radius of curvature, angular velocity, angular acceleration, pitch, and context (see fig. S12). For the speed bisection, we split the data separately for each angular bin based on the median speed in that bin; this per-bin bisection was done in order to avoid biases, as the speed of the bat showed some variation with the heading-direction due to the wind. We validated that this dependency of speed on wind direction could not explain the head-direction signal that we observed (fig. S8H-I).

Moon presence/absence split. To test for the effects of celestial cues dynamics (Fig. 4), we split the data based on presence or absence of the moon. Note that this is *not* a strict bisection of the data, as moon presence/absence was not necessarily 50/50%. Some head-direction neurons were recorded in only one of the two conditions, or did not have enough data in one of the two conditions, and were consequently removed from this analysis. This yielded $n = 20$ neurons valid for this analysis, out of which 10 were recorded in the double-sessions, comparing the 'moon below the horizon' and 'with moon' conditions. The other 10 neurons were recorded when the

moon was above the horizon, but was sometimes masked under heavy cloud coverage – which also covered the stars and the Milky Way.

Spatial stability of directional tuning: map analysis

To directly quantify the stability in the head-direction tuning of a neuron across space, we binned the environment into 40×40-m spatial bins, with a sliding-window step of 5-m. For each spatial bin we computed the directional tuning-curve (using 12 angular bins), and fitted a separate von-Mises function for each per-location (per-bin) tuning curve. We used the same inclusion criteria for these per-bin fits as for the main fits – namely, for each bin's directional tuning-curve we required the same 4 inclusion criteria as described above in the section 'Classification of head-direction cells' – except that here we relaxed our R^2 threshold (explained variance of the von-Mises fit) to be $R^2 > 0.5$ (instead of $R^2 > 0.7$ as in the main analyses of directional tuning). We included in this analysis only neurons which: (i) had > 160 valid spatial bins of 5×5-m (namely > 4,000 m^2 of covered area), and (ii) fired > 100 spikes in-air. This yielded $n = 62$ neurons. The bin size of 40×40-m was chosen in order to contain enough directional coverage; we note that 40×40-m typically constitutes one-fifth of the area covered per-night [median=19%], and also that the median radius of curvature of the bats' trajectories is 14-m. We also repeated this analysis using smaller bin sizes of 30×30-m [11% of the area covered] and 20×20-m [5% of the area covered], obtaining similar results (see below).

We quantified stability over space using two indices: (1) RV_{map}: We extracted the preferred direction for each directional tuning-curve in each spatial bin, and used the Rayleigh vector length of this distribution across all the spatial bins of the map as our index (*51*). This Rayleigh vector length (RV) over the map was termed 'RV_{map}' (see examples in Fig. 3G,J, and population in Fig. 3L). (2) Median tuning correlation: For each spatial bin we computed the directional tuning-curve using the data *inside* this bin and the directional tuning-curve using the data *outside* this bin, and then computed for each bin the Pearson correlation *r* between the inside-bin tuning curve and

outside-bin tuning curve – creating a spatial map of tuning correlations (see examples in Fig. 3H,K). We then defined our second stability index as the median of the *r* values over the spatial bins of the tuning-correlation map; e.g., the median of the *r* values over the maps in Fig. 3H. This median tuning correlation value was termed the 'median correlation' (population: Fig. 3M). To evaluate the statistical significance, for each neuron, we compared these two map-uniformity indices (RV_{map}, median correlation) to the same indices computed on two types of shuffles: (i) spike-shuffles: 1,000 rigid circular shuffles of the neuron's spike-train; and (ii) cell-shuffles: where each spatial bin was randomly taken from a different neuron, and this was repeated 1,000 times. This allowed us to assess the significance of these metrics by comparing each neuron to *both* sets of its shuffles. We repeated this set of map-analyses (including the comparison to the two types of shuffles) using smaller spatial bins of 30×30-m and 20×20-m (instead of 40×40-m), and obtained similar results (Fig. 3L-M: see three shades of blue; note that all three bin sizes resulted in similar distributions). We also repeated the cell-shuffling procedure using patches of bins (i.e. taking a patch of neighboring bins from the same neuron, instead of single bins) – with patch-sizes of 3×3, 5×5 or 7×7 bins – obtaining similar results (fig. S14).

Identifying mosaic neurons

We defined 'mosaic neurons' as neurons with local directional tuning but *no* global tuning (as opposed to globally-tuned neurons, which should exhibit both local and global tuning). In fig. S15, we focused on the population of 213 cells for which we could reliably assess local tuning metrics (this is the same set of cells which were valid for the map analyses in Fig. 3E-O). We calculated a third type of map – tuning sharpness map – which is the map of the Rayleigh vector length (RV) of each local tuning curve (fig. S15D) (*51*) and took the median of these RV values as the local tuning index of each neuron (see values of this index indicated above the 3 example neurons in fig. S15D). We assessed the significance of this index using the same criteria as for the global tuning index

(which is the RV of the cell's overall tuning curve using all the data): The median local RV had to be (i) higher than 95% of the values obtained using the cell's spike-shuffles, and (ii) larger than 0.1. Only cells which passed these two criteria, but did *not* pass the criteria to be a head-direction cell, were classified as putative mosaic cells (see fig. S15E, red crescent: $n = 32$ mosaic cells).

Head-direction tuning across time

Tuning over time. We calculated the directional tuning in 15-min windows (15-min sliding window with steps of 1-min, 12 angular bins), resulting in time-by-direction firing-rate matrices (e.g., Fig. 4C). For each time point, we extracted the neuron's preferred direction (by fitting von-Mises functions), and used a circular-linear regression (*85*) to fit a slope for each neuron (slope of the preferred-direction vs. time [°/min]). These slopes are the values plotted on the *y*-axis of Fig. 5D.

Stability during novel exploration

To test the head-direction stability during exploration of novel trajectories, we used the same functional bisection approach as above, with the same inclusion criteria – using two types of history-dependent bisections:

Distance from past trajectories. For every time point (every GPS sample), we calculated the minimum of the Euclidean distances to all the in-flight samples belonging to any of the previous flights of this session; see example in Fig. 6A. We termed this minimum distance as the 'distance from past trajectories'. We then bisected the samples in each session according to their distances from past trajectories (example neurons: Fig. 6B). As this is a strict bisection (i.e. 50/50% split), all neurons could potentially be included in this analysis (as long as the two halves had enough angular coverage [enough behavioral data] and the neuron fired enough spikes in both halves). This bisection captures outlier trajectories, but does not necessarily capture specifically those instances when the bat flew over completely novel areas.

Inside / outside the flight concave hull. To capture those instances when the bat flew over completely novel areas, we used the same flight-hull (concave-hull) definition as used for the full sessions (fig. S3C, pink area), but here we (i) accumulated the history of trajectories across *all* the previous sessions, and (ii) updated the flight-hull dynamically after each flight. In other words, after the first flight of the first session, we built a behavioral flight-hull using all the data from this first flight, then after the 2nd flight we recalculated the area using flights 1–2, and so on. Thus, for example, for flight no. 7 of session no. 3, we created an updated hull using all the trajectories from sessions 1 and 2 as well as the first 6 flights of session no. 3. We did *not* restart the updating process between sessions: namely, in later sessions we used all the bat's trajectories which happened in previous sessions. Using this process, we could assess for every time-point (every GPS sample) whether it was found inside the relevant flight-hull (built from all the bat's history up to this flight), or outside it (see Fig. 6D for an example flight bisected in this way). Notably, this process does not guarantee a strict bisection, namely the data is not necessarily split into 50/50% halves, as flights in later sessions have a smaller chance to go outside of the hull. However, for the cells which met the inclusion criteria for this analysis (n = 47 cells) – namely, cells that had enough behavioral coverage and enough spikes in each split – we could compare the head-direction tuning of the same neuron in familiar places vs. places that the bat had never visited before (example neurons: Fig. 6E).

Decoding analysis

We decoded the bat's direction from the activity of multiple simultaneously-recorded neurons, using a standard Bayesian maximum likelihood decoder (*78, 86, 87*). The decoder maximizes the following log-likelihood function:

$$A(\theta|\boldsymbol{n}) = \sum_{i=1}^{N} n_i \log\big(\tau\, r_i(\theta)\big) - \sum_{i=1}^{N} \tau\, r_i(\theta)$$

Where τ is the integration window (time-bin), N is the number of neurons, $\boldsymbol{n}$ is a vector of spike counts per neuron in each time-bin ($\boldsymbol{n}$ is a vector of length N), and $r_i(\theta)$ is the directional tuning-curve of neuron i as a function of direction θ. The decoding was performed on non-overlapping 1-second time-bins (τ = 1-s; we found that the decoding results did not change substantially when changing τ between τ = 0.1-s and 10-s: fig. S16A). We used 10-fold cross-validation for the decoding: Namely, the tuning curves were built from 90% of the data (train data), and then the decoding was performed on the spike counts from the other 10% of the data (test data) – repeating 10 times until the entire session was tested. In every time-bin, the decoded angle was taken as the angle which maximized the log-likelihood function. We included in this analysis only sessions where we recorded ≥ 10 neurons, out of which ≥ 5 neurons were significant head-direction cells (n = 10 sessions; Fig. 2I-J). To assess the decoder's performance, we compared the decoding errors to those obtained by using the same decoding scheme (with 10-fold cross-validation) on each neuron's 1,000 rigid spike-shuffles (Fig. 2J, shuffles).

In addition, we performed a cross-decoding analysis, where we bisected our data based on the various behavioral and environmental bisections, trained the decoder on one half and tested it on the other half, and vice versa. We included in this analysis only recording sessions which had enough neurons (as described above) and at least 3 minutes of flight in each condition. This resulted in one bisection which had only 1 valid session ('West/South shore), one bisection with n = 2 sessions (moon present/absent), one bisection with n = 4 sessions ('context'), and 10 bisections (all the rest) with n = 5 sessions. The results of this cross-decoding analysis are plotted in fig. 16C-D (moon bisection) and fig. S13B (12 spatial and non-spatial bisections).

UMAP dimensionality reduction

To perform dimensionality reduction of the population activity of ensembles of head-direction cells, we did the following. Spike counts of simultaneously recorded head-direction cells were calculated in 200-ms bins, and smoothed using a Gaussian kernel with $\sigma = 400$ ms, to produce a vector of firing-rate over time for each neuron. Time bins in which no cell had fired were discarded, and the firing-rate of each cell was mean-subtracted. These data were then used as the input to the nonlinear dimensionality reduction algorithm UMAP (*88*), using Python's *umap-learn* library, with the following parameters: 'n_components' = 3, 'metric' = 'cosine', 'n_neighbors' = 50, 'min_dist' = 0.4. We applied the algorithm separately for two behavioral modes: flight data (Fig. 2K), and stationary non-flight data (fig. S9F). Stationary data were defined as non-flight moments when the movement-speed was < 0.5 m/s, and the *Z*-acceleration signal was > 8 m/s^2 (upright).

Dynamics across days of the head-direction tuning

Since tetrode recordings do not allow tracking the same neurons over multiple days, we analyzed separately the cells recorded on each night, and then compared the results across-nights – in order to characterize the dynamics of the head-direction tuning across nights (Fig. 5). We analyzed here only neurons recorded during the night sessions (and not during the pilot daytime sessions), yielding $n = 86$ neurons which could potentially be analyzed. We examined the stability of the head-direction tuning in several ways.

First, we examined changes to the head-direction tuning during the first 10 minutes of each recording – and then compared across nights this short-term stability (stability within 10-min). The same was done for the last 10 minutes of each recording. Specifically, for the first 10 minutes, we used the same bisection approach as used for the spatial bisections, and computed separate tuning-curves using data from the first 5 min of recording and the next 5 min (that is, we compared minutes 0–5 vs. minutes 5–10); and similarly for the last 10 minutes (we compared the penultimate

5 minutes vs. the last 5 minutes). As with other bisections, each individual tuning curve had to pass all the inclusion criteria (enough behavioral coverage and enough spikes in each of the 5 minutes), resulting in $n = 62$ and $n = 45$ neurons valid for the comparisons for the first 10 minutes and the last 10 minutes, respectively. These neurons spanned 6 nights of outdoor flight. This analysis is shown in Fig. 5C.

Second, we analyzed the within-session change in preferred-direction (see above, under 'head-direction tuning across time') by comparing the neural slopes (change in preferred-direction vs. time [°/min]) across recording nights ($n = 77$ neurons). This analysis is shown in Fig. 5D.

Third, to further examine the evolution of spatial stability across nights, we examined how our map-uniformity index (median correlation, Fig. 3M) changes across nights ($n = 60$ neurons, using the inclusion criteria for the map analysis, as defined above). This last analysis is shown in Fig. 5E.

Magnetic field manipulation in the flight-tunnel

For this experiment (fig. S20), we conducted behavioral measurements and electrophysiological tetrode recordings of single neurons in the dorsal hippocampus area CA1 (and a few neurons from CA3) from two additional Egyptian fruit bats that were flying in a 180-meter long flight tunnel – at the Weizmann Institute of Science (not on the island). We used a 16-tetrode microdrive and wireless neural logger to perform the recordings – using procedures similar to our previous studies in the flight-tunnel (*78, 79*). We localized the bat's position in the tunnel using an ultra-wideband radio-frequency based localization system, yielding 5-cm precision. Echolocation click-rates were recorded using an on-head ultrasonic microphone, as done previously (*78*). The main differences from our previous studies of bats flying in the tunnel was that, here, we placed Helmholtz coils in the tunnel (fig. S20A, blue frames). This allowed us to turn a magnetic field on or off via a remote controller (custom made by the University of Oldenburg workshop) that was placed near the experimenter at the entrance to the tunnel. The coils were used in the Helmholtz-

coil configuration and consisted of two identical, calibrated, double-wounded coils (a coil pair from the 4-Merritt coils that were custom built at the university of Oldenburg and described previously in ref. (*89*)). The coils were powered by a constant current power supply with a ripple current < 0.0001 A (BOP 50-2M, Kepco Inc., USA). In the magnet-on condition, the current in the two sets of windings within each coil ran in parallel, producing a change in the magnetic field, which we calibrated to be slightly larger than the Earth's magnetic field, and which was directed 160° from north (in the horizontal plane) at the center of the coil. Magnetic-field calibration was performed using a high-quality hand-held magnetometer (FVM400 Vector Magnetometer, MEDA, USA). We verified the magnetic field in every flight-trial using an on-head magnetometer that was part of the neural-logger on the bat's head. The coil produced a highly localized magnetic perturbation (see fig. S20B for the on-head magnetometer measurements). In the magnet-off condition, the same current flowed in the two coils – thus controlling for potential minor acoustic, visual, or heat stimuli produced by the coils – but the current flowed anti-parallel in the two sets of windings within each coil, thus canceling out the two magnetic fields, and producing zero net magnetic field change.

We switched pseudo-randomly between magnet-on and magnet-off conditions every ~5–10 trials (flights). As is common in linear track hippocampal experiments, we analyzed the two flight directions separately (*78, 79*). We included in the analysis only sessions × directions in which the bat flew through the magnetic coil at least 10 times in each of the conditions (magnet-on, magnet-off). We then compared changes in flight-speed and echolocation click-rate in the magnet-on vs. magnet-off conditions (fig. S20C-D), as these behavioral variables, and especially the echolocation click-rate, are known to indicate bats' sensory attention (*78*).

We also computed firing-rate maps for each neuron separately for each flight direction, and used spatial information and a spike-shuffling procedure to identify significant place-cells; and we identified individual place-fields, which were detected as prominent, stable and significantly-tuned

peaks in the firing-rate maps – all as done in our previous studies of place-cells in this flight-tunnel (*78, 79*). To look for changes in firing-rate maps around the magnet location, we computed for each neuron the *z*-score of the difference in firing rates between magnet-on and magnet-off trials within a zone of ±15 meters around the magnetic coil. We included only cells that emitted spikes within this zone in either the magnet-on or magnet-off conditions – this yielded $n = 301$ cells × directions, from which $n = 228$ cells × directions were significant place-cells (fig. S20F, left). To further test for significant changes in the firing-rates of place cells in a localized area around the magnet, in magnet-on vs. magnet-off conditions, we conducted the following analysis (fig. S20H). We used all the cells × directions that (i) were significant place-cells in that direction, including having at least one significant place-field; and (ii) emitted spikes within a zone of ±2 meters around the magnetic coil, in either the magnet-on or magnet-off conditions – this yielded $n = 103$ cells × directions. In each of these neurons we performed a *t*-test to compare the firing-rates of the neuron in magnet-on trials vs. magnet-off trials; the firing-rates were computed within ±2 meters around the magnet. Cells × directions with P-value < 0.05 in the *t*-test were classified as responding significantly to the magnetic manipulation. We found that only 1.9% of the cells × directions ($n = 2$ of 103) were classified as significant – which is not greater than chance according to a binomial test at the 0.05 critical level (binomial test: $P = 0.97$).

Statistics

We used shuffling procedures to assess statistical significance. In all the manuscript, "spike-shuffles" refers to the rigid circular shuffle of spike-trains as defined above (and which was primarily used to assess the significance of head-direction tuning curves); and "cell-shuffles" refers to calculating an effect across neurons (i.e. comparing neuron i with neuron j for all neurons $i \neq j$). We used standard nonparametric tests for non-circular variables: Wilcoxon signed-rank test for one-sample tests, Wilcoxon rank-sum test for two-sample tests, and Kolmogorov-Smirnov test for comparing between

two distributions. For tests of circular variables, we used Rayleigh test for uniformity (a significant *P*-value indicates that the data is unimodal and non-uniform) and 2-sample Kuiper's test, which is similar to the Kolmogorov-Smirnov test, but is cyclically invariant, and hence suitable for comparing between two distributions of circular variables (*84*). We used the 1-sample Kuiper's test in the single case where we tested for uniformity without assuming unimodality (Fig. 2G). For correlations, we used the Pearson correlation for non-circular variables, Spearman correlation for non-circular variables that were distributed non-normally, circular-linear correlation when one variable was circular and another linear, and circular-circular correlation when both variables were circular (*84*). All circular statistics were computed using Matlab's circular statistics toolbox (*90*), except for circular-linear regression, which was computed using Matlab's FMAToolbox (*91*). Corrections for multiple comparisons were applied when relevant using the Bonferroni correction, and in one specific analysis (fig. S15I) we used the Benjamini-Hochberg FDR procedure (*92*). For further details, see above in the appropriate analysis sections.

Supplementary Results

The head-direction neural compass is unlikely to be anchored by magneto-sensation

One potential alternative explanation for the stable head-direction tuning is that head-direction cells are aligned by the Earth's magnetic field, akin to a magnetic compass (*8, 39*). Although there is no compelling evidence in the literature for magnetic compass sensing in any non-migratory bat species, we nevertheless tested this hypothesis explicitly in two experiments.

First, for 4 of the 6 bats we added another experimental session on the island: Flight inside a flight-tent (fig. S19A; tent size: 5.0 × 3.5 m). These indoor sessions were conducted just before the main outdoor sessions, allowing us to track the *same* neurons across both sessions. We provided illumination inside the tent, which greatly limited the bats' ability to see the outside environment (which was dark) from within the tent. This allowed us to record head-direction cells in two flight conditions which had practically no overlap in the visual cues available to the bats. We reasoned that if we find functional stability of the head-direction cells across these two distinct conditions, this would suggest the usage of a global, non-visual sensory directional cue, such as a magnetic compass. However, we found that head-direction cells exhibited very different directional tuning indoors vs. outdoors (examples: fig. S19B; population: fig. S19D: Rayleigh test for uniformity, $P = 0.38$; Kuiper's test vs. shuffles, $P = 0.42$; fig. S19E: Wilcoxon signed-rank test vs. 0, $P = 0.40$; Kolmogorov-Smirnov test vs. shuffles, $P = 0.30$).

Second, to more directly test whether Egyptian fruit bats can sense magnetic fields, we conducted a separate controlled experiment at the Weizmann Institute, in search for behavioral and neuronal responses to magnetic manipulations. We trained bats ($n = 2$) to fly in a 180-meter long tunnel, inside which we placed magnetic coils that can create controlled localized magnetic fields (fig. S20A-B; Methods). The bats did not show differences in flight-speed (fig. S20C) or in echolocation click-rate (fig. S20D) between the magnet-on and magnet-off trials. Because a lack of behavioral response to the magnetic manipulation does not entail that it was not perceived by the bat,

we also conducted neural recordings during this manipulation. We focused on recording hippocampal CA1 place-cells, because these neurons are known to be sensitive to environmental changes (*93-96*). However, we did not find any difference in place-cells' firing near the coils in the magnet-on vs. magnet-off conditions (examples: fig. S20E; population: fig. S20F left panel, and fig. S20G-H; Methods). The lack of neuronal responses to the magnetic perturbation contrasts with the typically strong responses of CA1 place-cells to environmental changes in cue-manipulation experiments (*93-96*).

Overall, our results argue against the use of a magnetic compass by these bats: (1) We observed dynamics of directional tuning across nights (Fig. 5) – even though the Earth's magnetic field was constantly present from the first moment. (2) The rotation of the directional tuning indoors vs. outdoors (fig. S19) is also inconsistent with a magnetic compass – because the Earth's magnetic field is identical indoors and outdoors. (3) The coil experiment (fig. S20) did not provide any evidence for magnetic sensing in this bat species. This implies that the highly stable head-direction signal that we recorded outdoors on the island is unlikely to depend on the Earth's magnetic field.

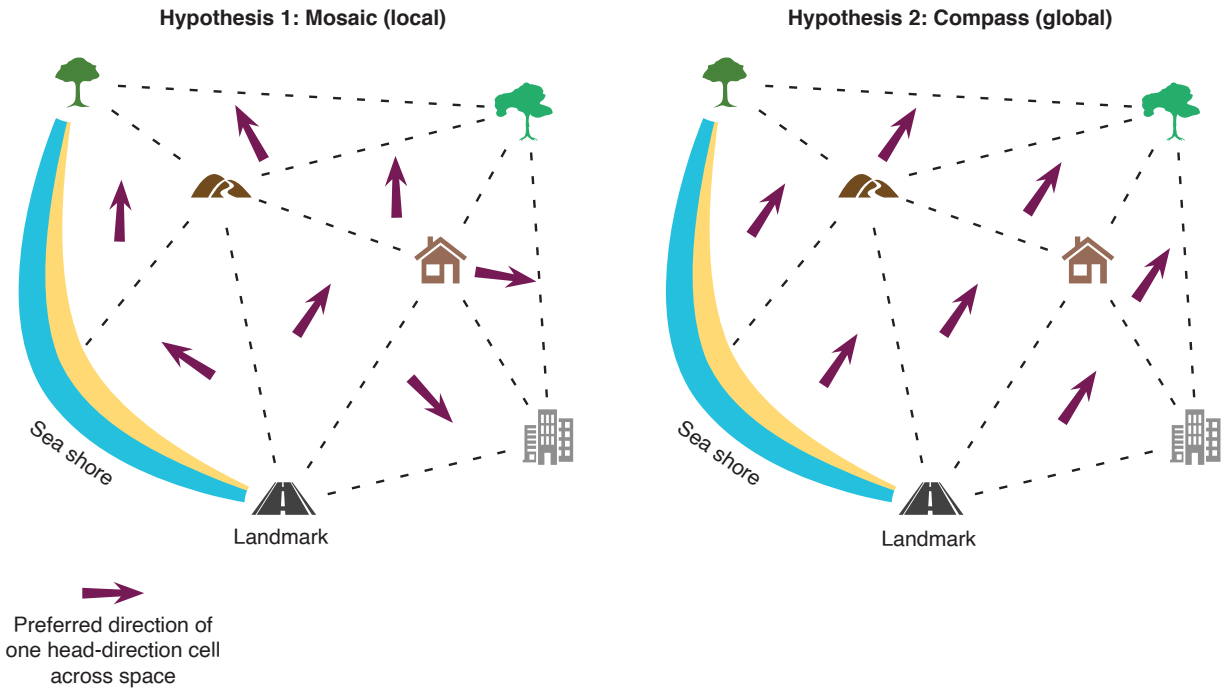

fig. S1: Two hypotheses for the directional coding of head-direction cells in natural environments outdoors. Left, hypothesis 1: Mosaic representation (local) – head-direction cells are dominated by local cues, and therefore the tuning of a given head-direction cell rotates when the animal is moving over large geographical spaces and across multiple regions, and uses different sets of landmarks in each region (see randomly-oriented arrows, depicting the hypothetical directional tuning of *one* neuron across space). We note that a mosaic arrangement does *not* necessarily imply sharp transitions between spatial domains, as illustrated here; instead, the transitions might be gradual. Right, hypothesis 2: Compass representation (global) – head-direction cells maintain a stable global directional tuning across the space that is relevant for the animal. Under this hypothesis, a given neuron shows the same preferred-direction at all spatial locations (see parallel arrows).

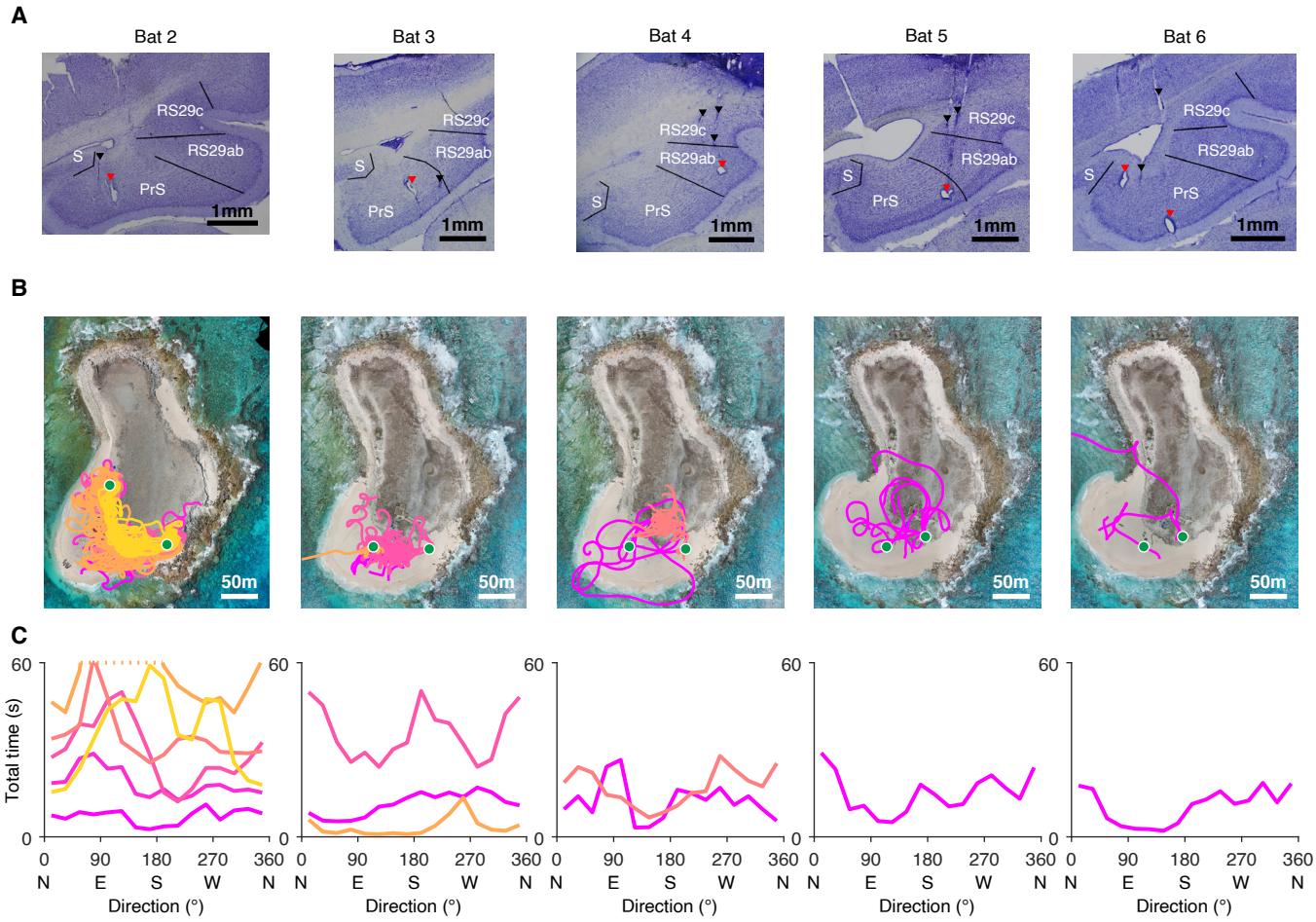

fig. S2: Histology and trajectories of all bats. Columns in **A-C**, individual bats. **(A)** Representative coronal slices from five bats which were used in this study (bats 2–6). Bat 1 is plotted in Fig. 1E. Black arrowheads mark tetrode tracks on the way down to the dorsal presubiculum or retrosplenial cortex, and red arrowheads mark electrolytic lesions in the dorsal presubiculum or retrosplenial cortex. PrS, presubiculum; RS, retrosplenial cortex; S, subiculum. Scale bar, 1 mm. **(B)** Drone photos of the island, overlayed with each bat's flight trajectories. Photos were selected based on the dates of each bat's recording sessions (for each bat we chose here the drone photo that was taken on the closest date to the majority of recording nights of that bat). Different colors represent individual sessions (bat 2: n = 6 sessions, bat 3: n = 3 sessions, bat 4: n = 2 sessions, bats 5 and 6: n = 1 session each). Green dots, platform locations. Scale bar, 50 m. **(C)** Angular coverage for each experimental session of bats 2–6 (each line represents one session, and shows the total time spent in-air in each directional bin [16 bins]; y-axis for bat 2 was clipped at 60-s, for display purposes). Same colors as in **B**. Bat 1 is plotted in Fig. 1G,P.

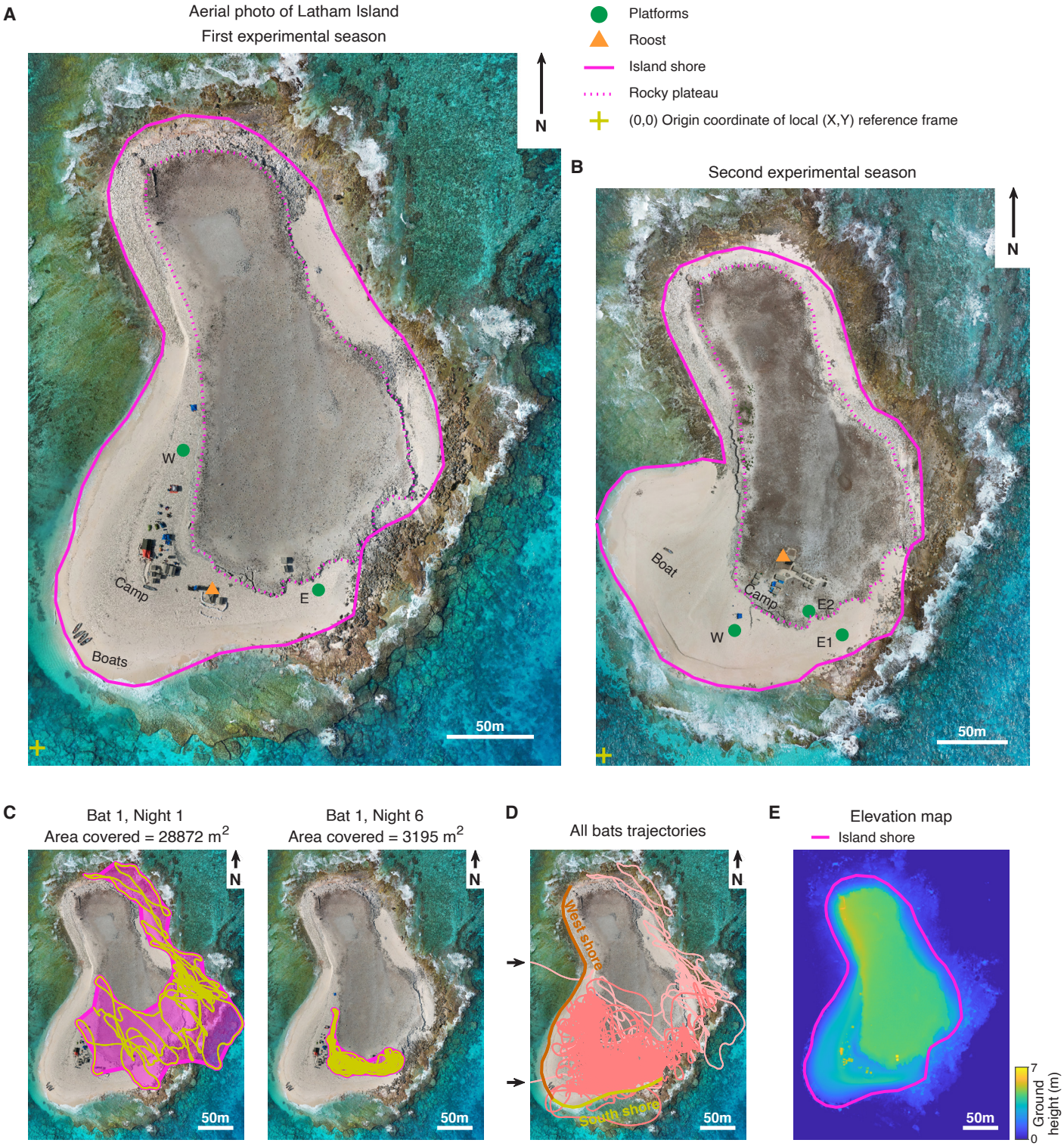

fig. S3: Detailed geography of Latham Island. This figure shows drone photos of the island; all scale bars are 50 m. See Fig. 1H and fig. S4A for ground-level photos of the island. **(A)** Drone photo of Latham Island, taken in the first experimental season (March 2023). Pink curves denote the island shore (solid line) and the rocky plateau (dotted line). Green dots, platform locations ('W', west platform; 'E', east platform). Orange triangle, bats' roost. Yellow cross at bottom-left, origin coordinate (0,0) for the local (X,Y) reference frame; 'N', north. **(B)** Same as **A**, for the second experimental season (March 2024). The east platform was moved from its initial position (E1) to a new position (E2) in the middle of the experimental season. **(C)** Drone photos of the island, overlayed with the trajectories of bat 1 (yellow curves) on night 1 (left) and night 6 (right), and the corresponding flight-hull (concave-hull; pink); the area of the hull is indicated (area covered by the bat in each session). **(D)** Drone photo of the island, overlayed with all the trajectories of all the six bats (peach); the west-shore and south-shore of the island are marked by thick orange and yellow curves, respectively. The flight trajectories are colored in peach shade – except 5 outlier flight-trajectories that are colored in light-peach shade; these 5 flights comprised 3 flights concentrated along the east shore, and 2 flights above the water (marked by horizontal arrows): these 5 flights were not used in the analysis of directional tuning near the west/south shore (main Fig. 3C, right boxplot) – but were used in all other analyses. **(E)** Digital elevation map (digital elevation model) of the island, constructed from the drone photos taken in the first experimental season, overlayed with the island shoreline in pink. The elevation Z-origin (0 meters) is the sea level (see color-scale). Note that this elevation map captures also the elevation of the tents (yellow spots).

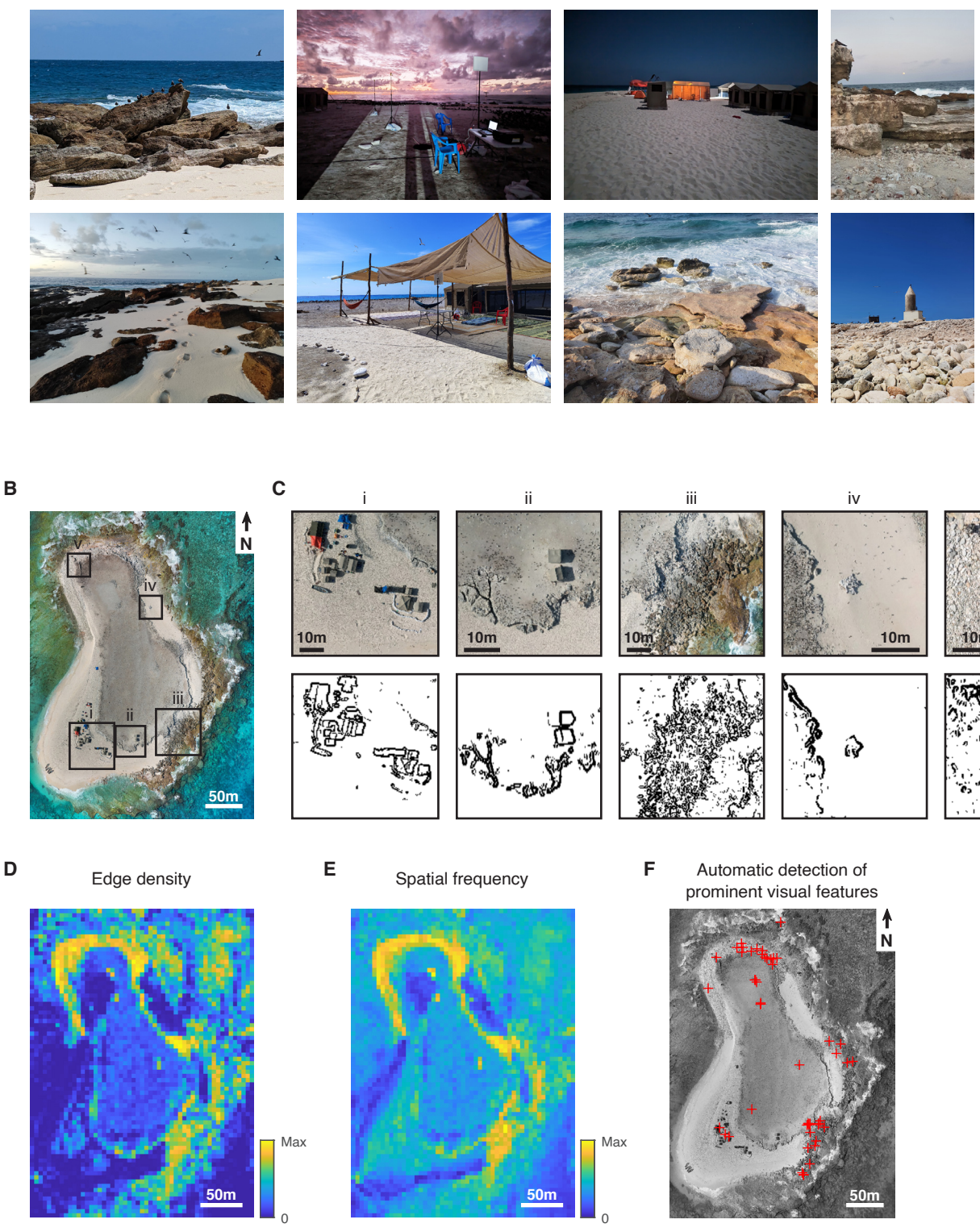

fig. S4: Visual richness of the island's natural environment. Figure legend on the next page

fig. S4: Visual richness of the island's natural environment. **(A)** Eight photos taken on the island during the two experimental seasons, depicting some of the landmarks that the bats may have used for navigation: both natural landmarks and human-made landmarks. See additional four photos in main Fig. 1H. It is of course quite possible that the bats used other landmarks than shown here – and that different bats used different landmarks; the purpose of showing these photos is to illustrate the high visual richness on the island, which included many more landmarks in addition to the ones shown here. Photo credits in this study: S. Palgi, C. Cohen, N. Ulanovsky. **(B-C)** Areas with high abundance of landmarks. **(B)** Drone photo of the island, with 5 squares marking regions with high numbers of visual landmarks (tents, unique rock formations, ruins, etc). **(C)** Top row: Zoom-in on the regions marked in **B**. Bottom row: the output of an edge-detection algorithm used on the photo. Note the high number of edges, signifying visual richness. **(D)** Average density of edges, calculated in 5×5-meter bins. **(E)** Same as **D**, for spatial frequency, which is a measure of overall structure in the image (*97*). **(F)** Automatic feature detection using the SURF algorithm (*98*), a computer-vision algorithm which captures prominent objects in an image. Shown is a grayscale version of the drone photo, which was used as input to the algorithm, together with the top 50 points which this algorithm found (red crosses): these points correspond to potential points of interest or landmarks in the real world. Note that this is an underestimation of the rich visual information available to animals navigating such spaces. As suggested in the discussion section, we propose that the bats likely used some of the landmarks on the island as well as the overall geometrical shape of the island, in order to navigate and to anchor their global neural compass.

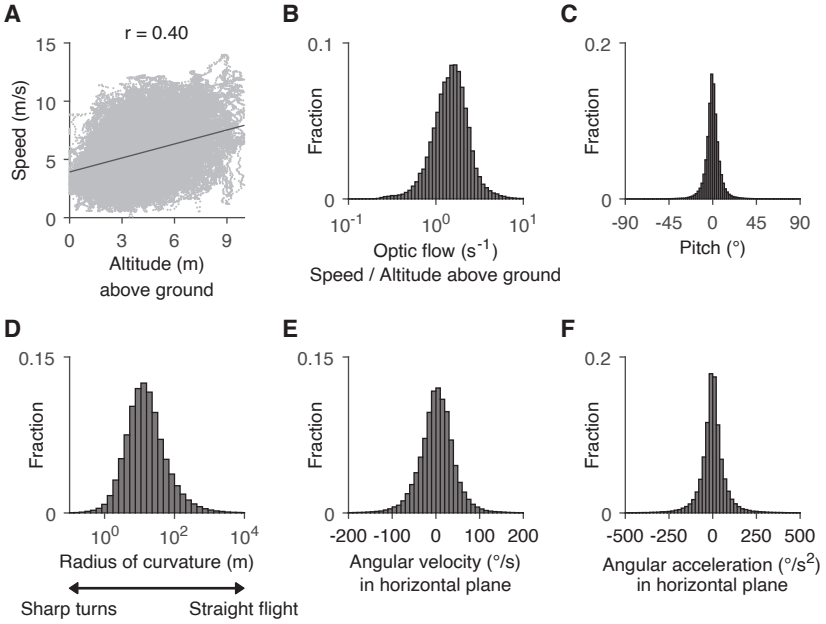

fig. S5: Distributions of behavioral variables. Data pooled over all the behavioral sessions in all bats (n = 22 sessions from 6 bats; Methods; in 20 of these 22 sessions, we recorded significant head-direction cells). **(A)** Scatter plot of the bat speed vs. its altitude above ground (light-gray dots), with a least-squares regression line (dark-gray). Speed and altitude were correlated (r = 0.40, $P < 10^{-300}$): the bats were flying faster at higher altitudes. **(B)** Histogram of optic flow, defined as the speed divided by the altitude above ground (Methods). The x-axis is in log-scale. **(C)** Histogram of the bats' pitch (vertical) angle during flight. Positive values correspond to flying upward. The range of pitch angles in this experiment was limited, hence in this study we focused on the neurons' azimuthal (horizontal) directional coding. **(D)** Histogram of the radius of curvature of the flight-trajectories: a local measure of the straightness of a trajectory, calculated at each point along the trajectory (Methods); larger radius corresponds to straighter flight. The x-axis is in log-scale. **(E)** Histogram of the bats' angular velocity in the horizontal plane. Positive values correspond to turning clockwise. **(F)** Histogram of the bats' angular acceleration in the horizontal plane.

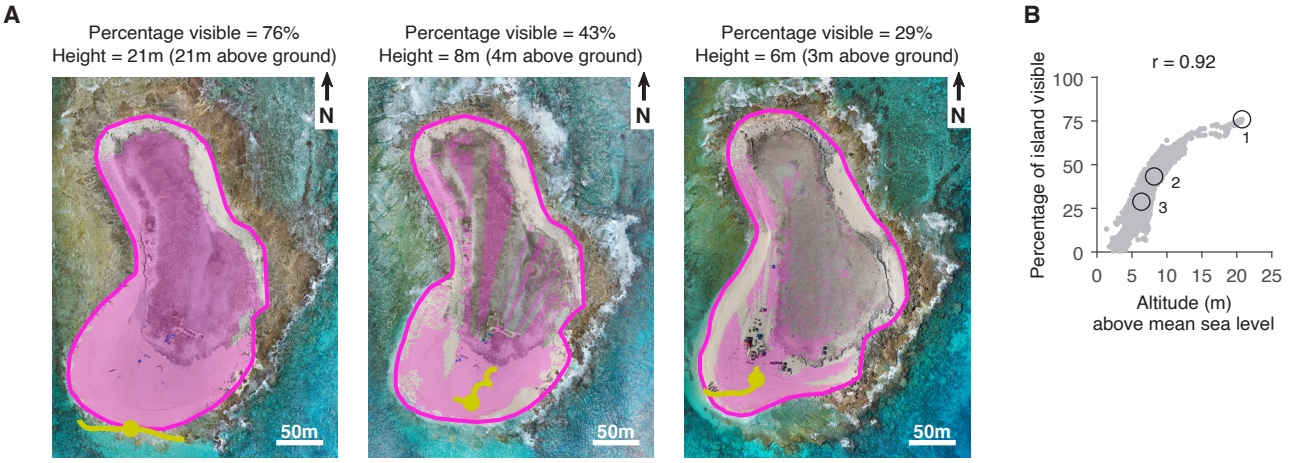

fig. S6: Bats could see only a fraction of the island at any given moment. Line-of-sight analysis, conducted using the drone-based digital elevation map (e.g., fig. S3E) and the bats' trajectories, quantifying the percentage of the island visible to the bats at any given moment. The percentage of island visible is shown in main Fig. 1N; here we show examples and additional quantification. The percentage visible was calculated using Matlab's function *viewshed*, and was defined as the fraction of visible pixels, using only pixels located within the island's borders. This calculation uses the full XYZ position of the observer (the bat), and the XYZ structure of the environment (the ground), and calculates which pixels in the map are occluded by other objects (cliffs, tents, boulders, etc.). For simplicity, we did not consider occlusions due to the Earth's curvature (as they are negligible at this range), and also did not consider occlusions by the bat's own head due to limited visual angle (as this species of bats has a very wide visual field of ~270°). Under the conditions of our experiments, these bats could in principle see all the way to the other side of the island. Therefore, we did not limit our calculation to the area of the island covered by the bats – as they could potentially see (and use landmarks) beyond this area, as long as there were no occlusions. We calculated the line of sight during flight every 1 second. **(A)** Three example flights demonstrating different degrees of occlusion. In each plot, 20 seconds of flight are shown in yellow lines, overlaid on a photo of the island (for each example we show the photo taken closest to the date of that recording). Yellow dots denote the focal point for each example: these were the points in the flight that had the highest visibility (highest percentage-visible of the island area). Height above mean sea-level and above ground are indicated, and refer to the bat's altitude at the yellow dot. Pink lines denote the island's border, and pink shading denotes the areas that the bat could see from its current location and altitude, according to the line-of-sight calculation. Left: high-altitude flight (21 m above ground) on the border of the island, yielding high visibility (76% of the island was visible). Middle and right: flights at lower altitudes, and/or near the camp, yielding lower visibility due to occlusions (43% and 29% of the island was visible, respectively). Note in the middle plot the pink-colored "sun-ray" pattern of visibility, which is created by the tall tents that occluded large portions of the island located behind them; and note in the right plot the occlusion created by the southern cliff of the rocky plateau. Note also that shown here are the points of *highest* visibility in these three flights: the visibility was even lower in all the other time-points in these flights. **(B)** Scatter plot of the percentage of the island visible at each point vs. the altitude above ground. These variables were correlated (Pearson $r = 0.92$, $P < 10^{-300}$; $n = 8{,}252$ samples [1-s windows]): as the bats flew higher, they could see larger portions of the island. Circles denote the 3 flights shown in **A**.

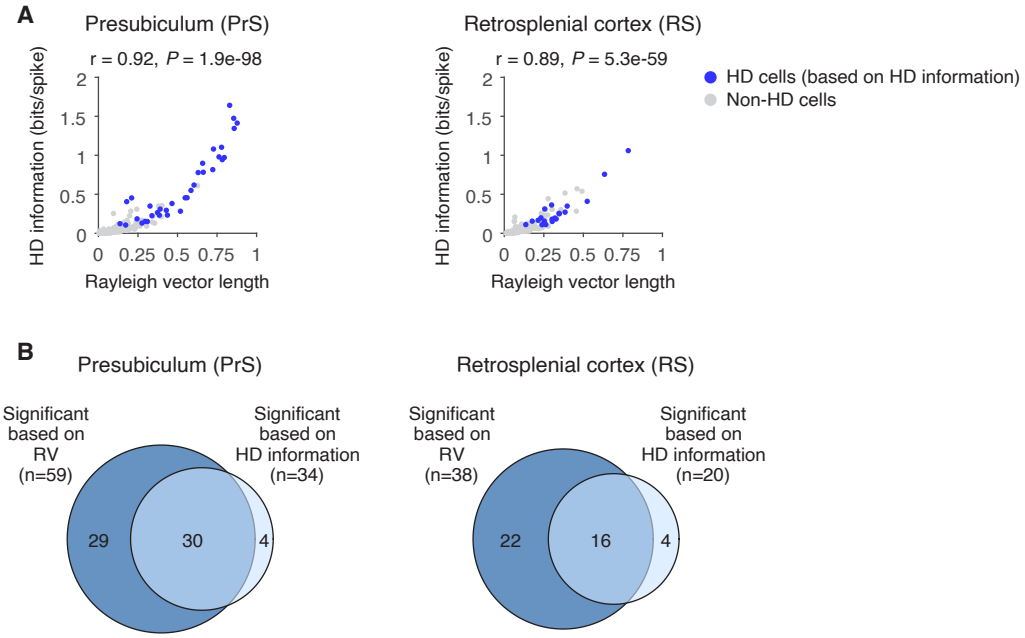

fig. S7: Identifying significant head-direction cells. **(A-B)** An alternative criterion for identifying significant head-direction cells, using their head-direction (HD) information content (*20*), instead of the Rayleigh vector length that was used throughout this study. The HD information, I, is defined as: $I\left(\frac{\text{bits}}{\text{spike}}\right) = \sum p_i(\frac{r_i}{\bar{r}}) \log_2(\frac{r_i}{\bar{r}})$, where r_i is the firing rate of the cell in the i^{th} directional bin, p_i is the probability of the bat's head-direction to be in this bin, and $\bar{r}$ is the mean firing-rate of the cell. **(A)** Population scatters, showing HD information vs. Rayleigh vector length for presubiculum cells (left panel), and retrosplenial cortex cells (right panel). Blue dots, head-direction cells identified using this alternative criterion (we required significant HD information compared to shuffles and HD information ≥ 0.1 bits/spike). Gray dots, non-significant cells according to this criterion. HD information and Rayleigh vector length were highly correlated (Pearson correlations are indicated). **(B)** Venn diagrams for the two brain areas, showing significant head-direction cells based on two alternative definitions: Using Rayleigh vector length (RV) and using HD information.

We note that based on the RV definition, which is the definition used throughout this study, we did not find major differences between the two brain areas: The percentage of head-direction cells was similar between the two areas (presubiculum: 25%, retrosplenial cortex: 22%; χ^2 test: $P = 0.62$), and the RV of their directional tuning was also quite similar (Wilcoxon rank-sum test: $P = 0.14$).

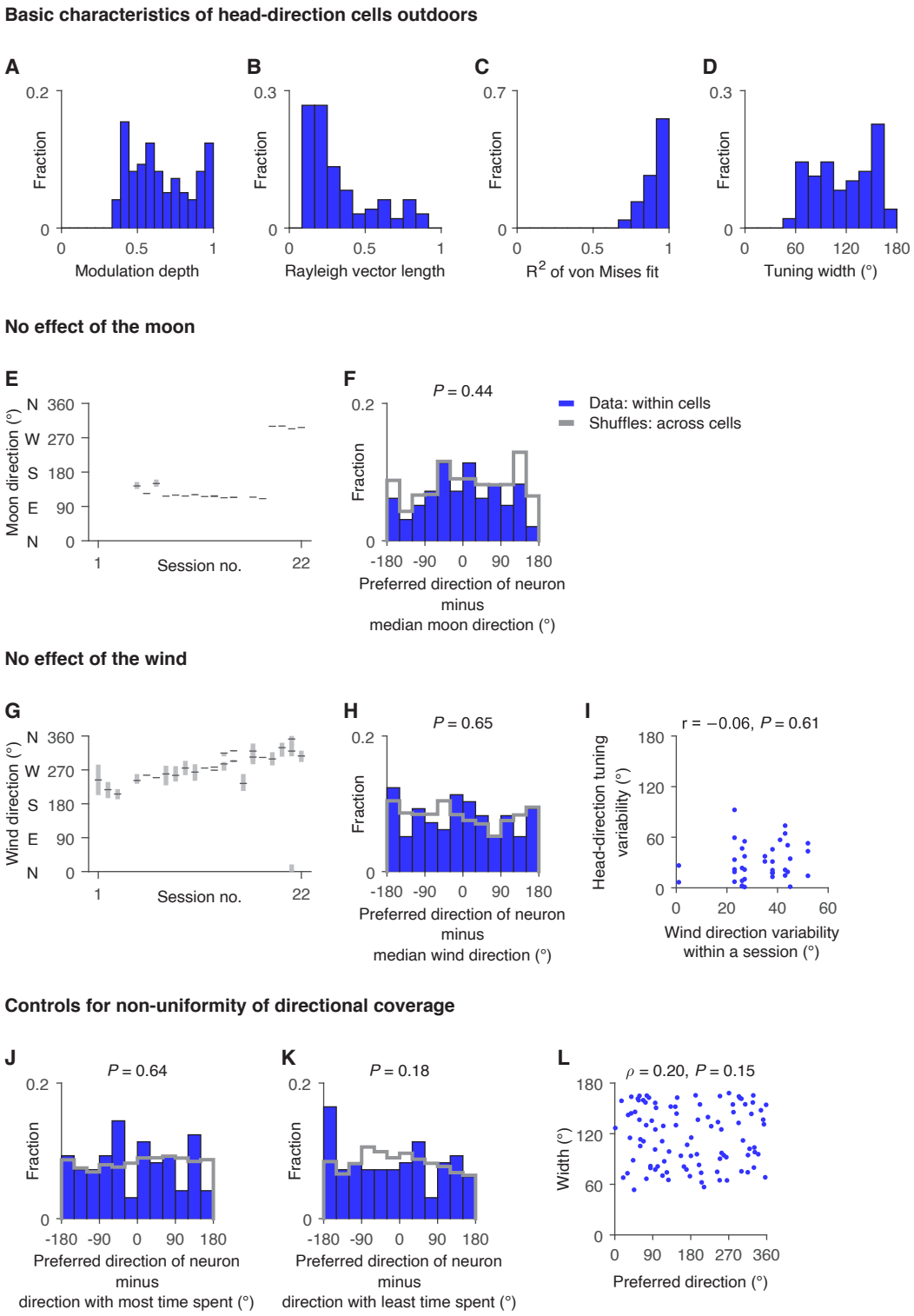

fig. S8: Characteristics of head-direction cells, and controls for the head-direction tuning. Figure legend on the next page

fig. S8: Characteristics of head-direction cells, and controls for the head-direction tuning. (A-D) Basic characteristics of head-direction cells outdoors (*n* = 97 neurons). **(A)** Histogram of modulation depth, which quantifies the relative depth of the tuning curve $r(\theta)$. Modulation depth (MD) was calculated based on the fitted von-Mises functions, using the following formula: $MD = \frac{\max(r(\theta)) - \min(r(\theta))}{\max(r(\theta))}$ (MD of 1 corresponds to zero baseline firing). **(B)** Histogram of Rayleigh vector length. **(C)** Histogram of goodness-of-fit (R^2) of the von-Mises fit to the neurons' directional tuning-curves (see Methods). High values denote symmetric unimodal tuning. **(D)** Histogram of tuning width at half-height. **(E-F)** No effect of the direction of the moon. **(E)** Range of the moon direction during the experiment. Black lines: the median direction of the moon in each session, as calculated from astronomical databases (Methods). Gray bars: full angular range of the moon during each outdoor recording session; note that most of the gray bars are too small to see, because the moon moved very little during the recording session. Sessions 1–15 are from the 1st year of experiments on the island, and sessions 16–22 are from the 2nd year. Only epochs when the moon was visible are plotted (when the moon was above the horizon, and without cloud coverage; *n* = 17 sessions out of the total of 22 sessions from 6 bats; the differences in the median moon direction across sessions are due to different dates and recording hours). **(F)** Distribution of the differences between each cell's preferred direction and the median moon direction in that session (blue: data [within-cell comparison]; gray: shuffles across cells [the preferred direction of cell *i* minus the moon direction for cell *j*, for all cells $i \neq j$]). There was no over-representation of the moon direction across the population of head-direction cells (Kuiper's test comparing the distributions of the data vs. the shuffles: *P* = 0.44; *n* = 79 head-direction cells which were recorded with the moon visible above the horizon). **(G-I)** No effect of the direction of the wind. **(G)** Same as **E**, for the direction of the wind – where the wind direction was measured using a portable weather station. Shown are data for all sessions, except one session for which we did not have wind measurements (*n* = 21 out of the total of 22 sessions; *n* = 6 bats). Note that in some sessions the wind changed its direction quite substantially within the session (see the vertical gray bars). The 5 sessions with two black lines denote the 5 nights where we performed both a with-moon and without-moon experiment (Methods); here we plotted the wind-directions separately for both cases. **(H)** Same as **F**, for the differences between each cell's preferred direction and the median wind direction in that session. There was no over-representation of the wind direction across the population of head-direction cells (Kuiper's test for data vs. shuffles: *P* = 0.65; *n* = 95 head-direction cells for which wind measurements were available). **(I)** Scatter plot of the variability of the head-direction tuning (absolute difference between the preferred direction in the 1st and 2nd halves of the session) vs. the wind direction variability (range of the wind directions measured in each session). There was no correlation between wind directional variability and neural-tuning directional variability (Pearson *r* = –0.06, *P* = 0.61). **(J-K)** Controls for non-uniform behavioral directional coverage. **(J)** Distribution of differences between each cell's preferred direction and the direction with *most* time spent in that session (the center of the directional bin in which the bat spent the longest flight-time). No significant difference was found between the data (blue) and the shuffles (gray, cell-shuffles [across cells]; Kuiper's test for data vs. shuffles: *P* = 0.64; *n* = 97 head-direction cells). **(K)** Same as **J**, for the differences between the cell's preferred direction and the direction with *least* time spent (Kuiper's test for data vs. shuffles: *P* = 0.18; *n* = 97 head-direction cells). The uniform distributions in **J** and **K**, which were not different from the cell-shuffles, suggest that the head-direction tuning could not be explained by non-uniform behavioral directional coverage. **(L)** Scatter plot of each neuron's tuning width vs. its preferred direction. No significant correlation was found between the tuning width and the preferred direction (circular-linear correlation: ρ = 0.20, *P* = 0.15; *n* = 97 head-direction cells).

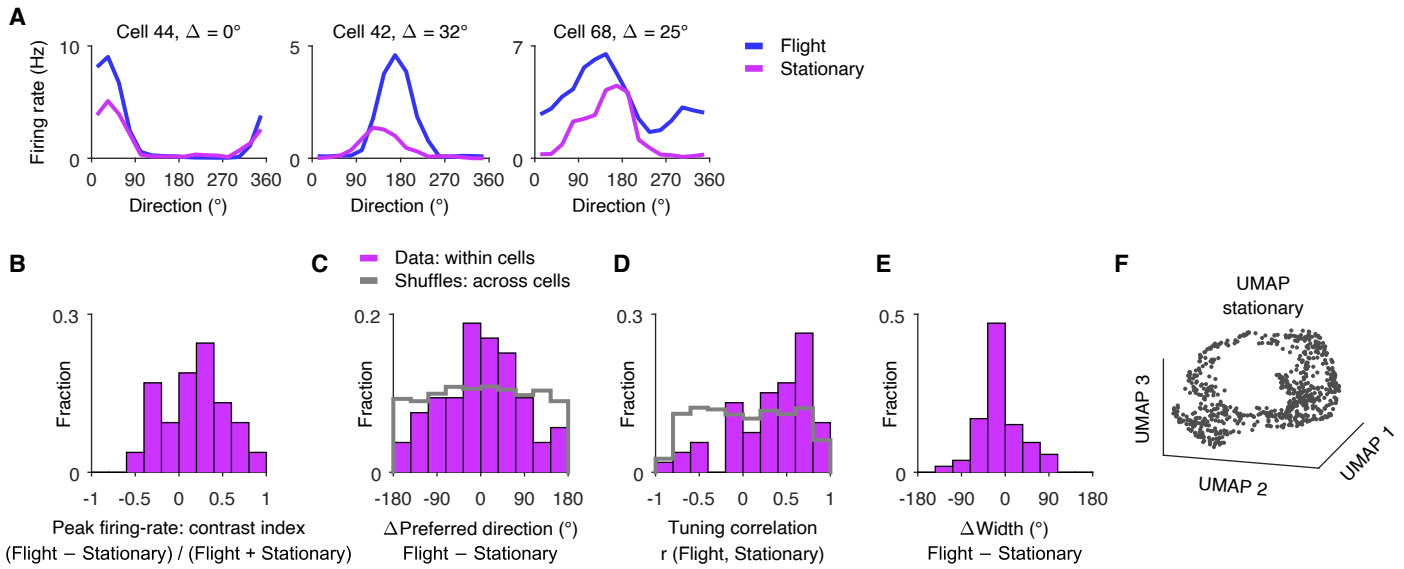

fig. S9: Head-direction tuning during stationary periods outdoors was similar to the tuning during flight outdoors. Here we focused on the subset of head-direction cells identified during flight, which also showed some directional tuning during stationary periods between flights (n = 53 cells with enough data in both conditions, and a Rayleigh vector length > 0.1 during stationary epochs; Methods). **(A)** Three example neurons. For each neuron, shown are its directional tuning-curves during flight (blue) and stationary non-flight (purple); Δ, the absolute Δpreferred direction between the two curves. Cell 44 is shown also in Fig. 2E, and is plotted here again for completeness. **(B)** Population histogram of the contrast index for the peak firing-rate of the tuning in flight vs. stationary ($\frac{\text{Flight} - \text{Stationary}}{\text{Flight} + \text{Stationary}}$). Peak firing-rate was higher in flight than during stationary epochs (Wilcoxon sign-rank test vs. 0: P = 0.0005), as was shown also in laboratory-based experiments (*22, 25*). **(C)** Histogram of ΔPreferred direction, calculated within cells (data: purple) and across cells (cell-shuffles: gray). Same histogram as Fig. 2F, plotted here again for completeness. The differences in preferred direction were distributed with a peak around 0° (Rayleigh test for uniformity: P = 0.0004), and were significantly different compared to shuffles (Kuiper's test, data vs. shuffles: P = 0.017). **(D)** Tuning correlation between the tuning curves in-flight and during stationary periods. The tuning correlations were significantly different from random remapping (Wilcoxon signed-rank test vs. 0: P = 3.2×10^{-5}) and from the shuffles (Kolmogorov-Smirnov test, data vs. shuffles: P = 9.7×10^{-5}). **(E)** Histogram of ΔWidth (flight minus stationary). Tuning width was slightly narrower during flight compared to stationary (Wilcoxon signed-rank test vs. 0°: P = 0.037; median difference = 11°). **(F)** UMAP dimensionality-reduction of the neuronal population activity from a single experimental session, taken from stationary non-flight epochs (same session and cells as in Fig. 2K). Each dot corresponds to a single point in time (200-ms bins). The neural activity lied on a low-dimensional manifold forming a ring-like structure – qualitatively similar to the in-flight data (Fig. 2K).

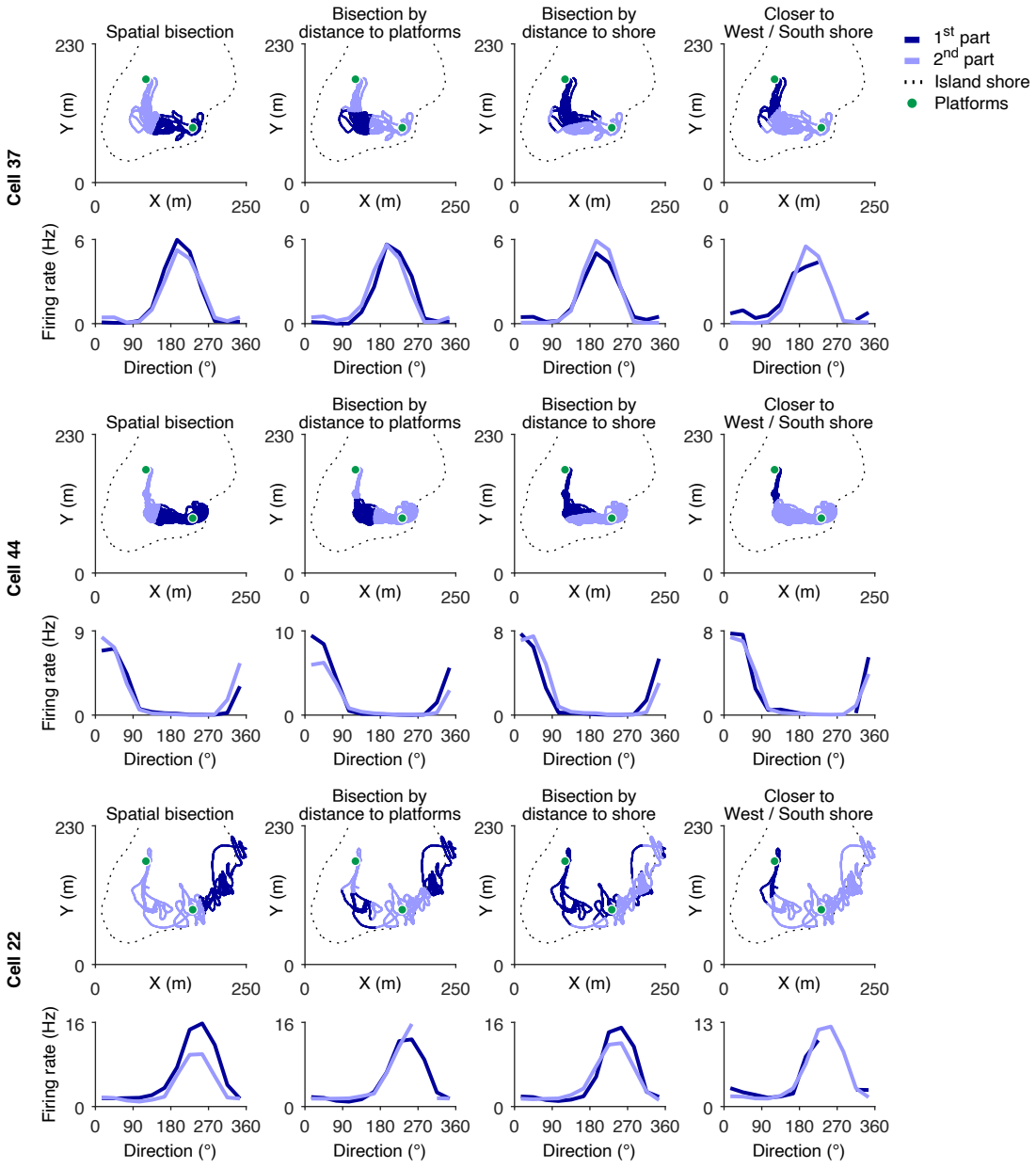

fig. S10: Spatial bisections – example neurons. Three example neurons. Data plotted in a grid of 3 neurons (rows) × 4 bisections (columns). Two rows are shown for each neuron. The top row of panels for each neuron shows the bat trajectories, plotted in light-blue and dark-blue according to the relevant bisection: spatial bisection (column 1), distance to the closest platform (column 2), distance to the closest shore (column 3), closer to west/south shore (column 4). Locations of the platforms (green dots) and the island shore (black dotted line) are also plotted. The bottom row of panels for each neuron shows the directional tuning-curves, computed separately for each half of the data, in each bisection.

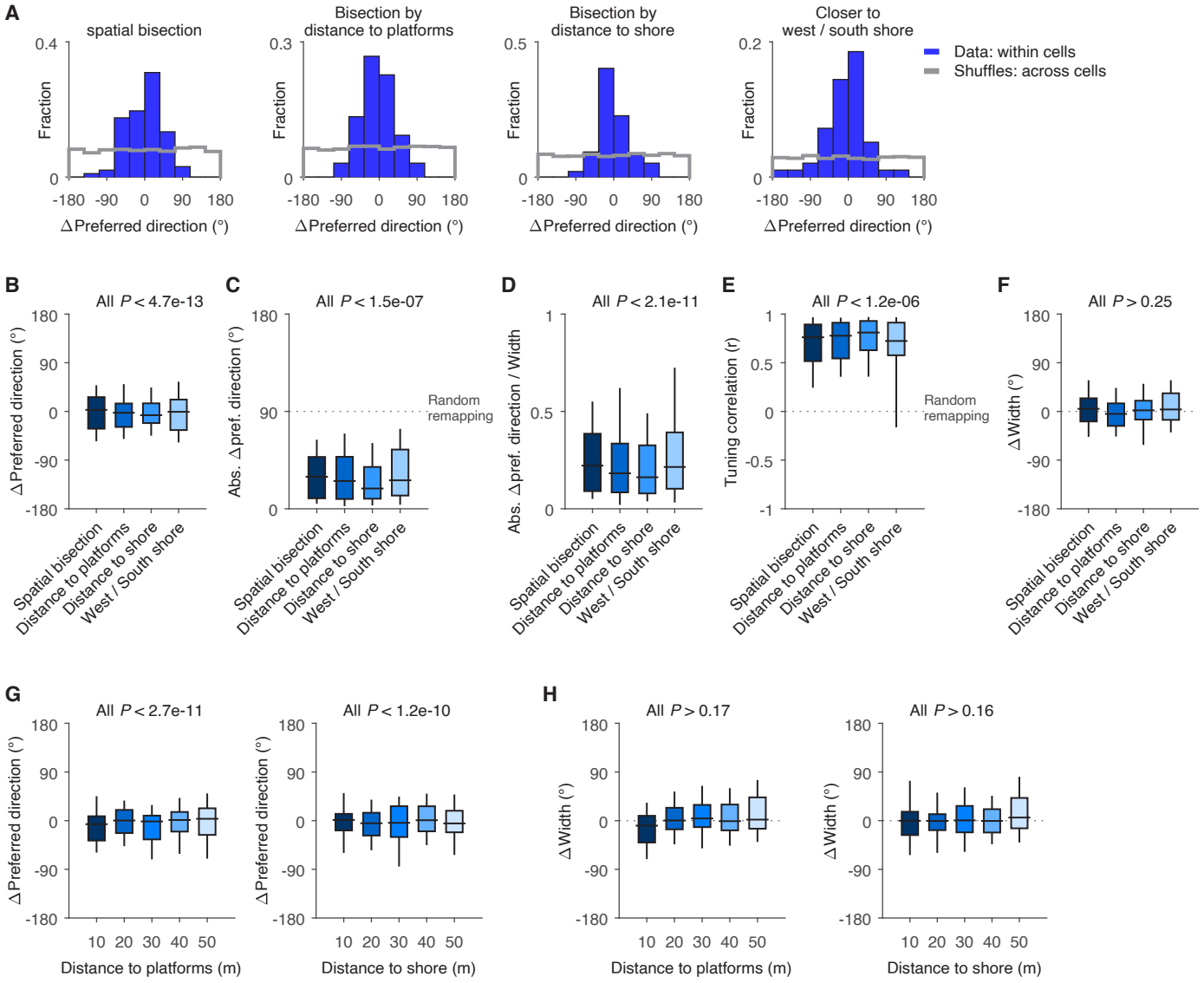

fig. S11: Spatial bisections – population. **(A)** Population histograms of ΔPreferred direction for the four spatial bisections (blue; see Methods). The leftmost and rightmost panels are the same data plotted in Fig. 3C as boxplots. Cell-shuffles are plotted in gray. **(B)** Difference in preferred direction between the two halves (similar to Fig. 3C; Rayleigh test for uniformity: all $P < 4.7\times10^{-13}$). **(C)** Absolute value of ΔPreferred direction (similar to Fig. 3D; Wilcoxon signed-rank test vs. 90°: all $P < 1.5\times10^{-7}$). **(D)** Absolute value of ΔPreferred direction, normalized by the tuning-width of the neuron (Kolmogorov-Smirnov test vs. shuffles: all $P < 2.1\times10^{-11}$). **(E)** Tuning correlation (Pearson r) between the two halves (Wilcoxon signed-rank test vs. 0: all $P < 1.2\times10^{-6}$). **(F)** Difference in tuning width between the two halves (ΔWidth; Wilcoxon sign-rank test vs. 0°: all $P > 0.25$). All P-values in panels **B-F** were Bonferroni corrected for the $n = 4$ comparisons. Boxplots in each panel, from left to right: $n = 85$, 76, 85 and 50 cells with enough data in each half. **(G-H)** Parametrized bisections. We repeated the bisection analysis by gradually increasing the distance thresholds (using fixed thresholds in meters), and found that the head-direction tuning was robust to the choice of thresholds – namely, even when comparing flights which were very close to the shore or to the platforms, there was no systematic difference in the preferred direction or in the tuning width. Plotted are population boxplots of (**G**) preferred direction differences, and (**H**) tuning-width differences, calculated by applying a series of fixed threshold (in meters) to the behavioral data (note that these are not strict bisections, as they did not divide the data into two equal parts). **(G)** Preferred direction differences as a function of distance to platforms (left; Rayleigh test for uniformity: all $P < 2.7\times10^{-11}$) and as a function of distance to shore (right; all $P < 1.2\times10^{-10}$). **(H)** Same as **G**, for tuning-width differences (left: Wilcoxon sign-rank test against 0°: all $P > 0.17$; right: all $P > 0.16$). All P-values were Bonferroni corrected for the number of distance-bins ($n = 5$). In all boxplots, horizontal lines denote medians, boxes denote 25–75th percentiles, and whiskers denote 10–90th percentiles. Similar P-values were obtained when comparing to cell-shuffles.

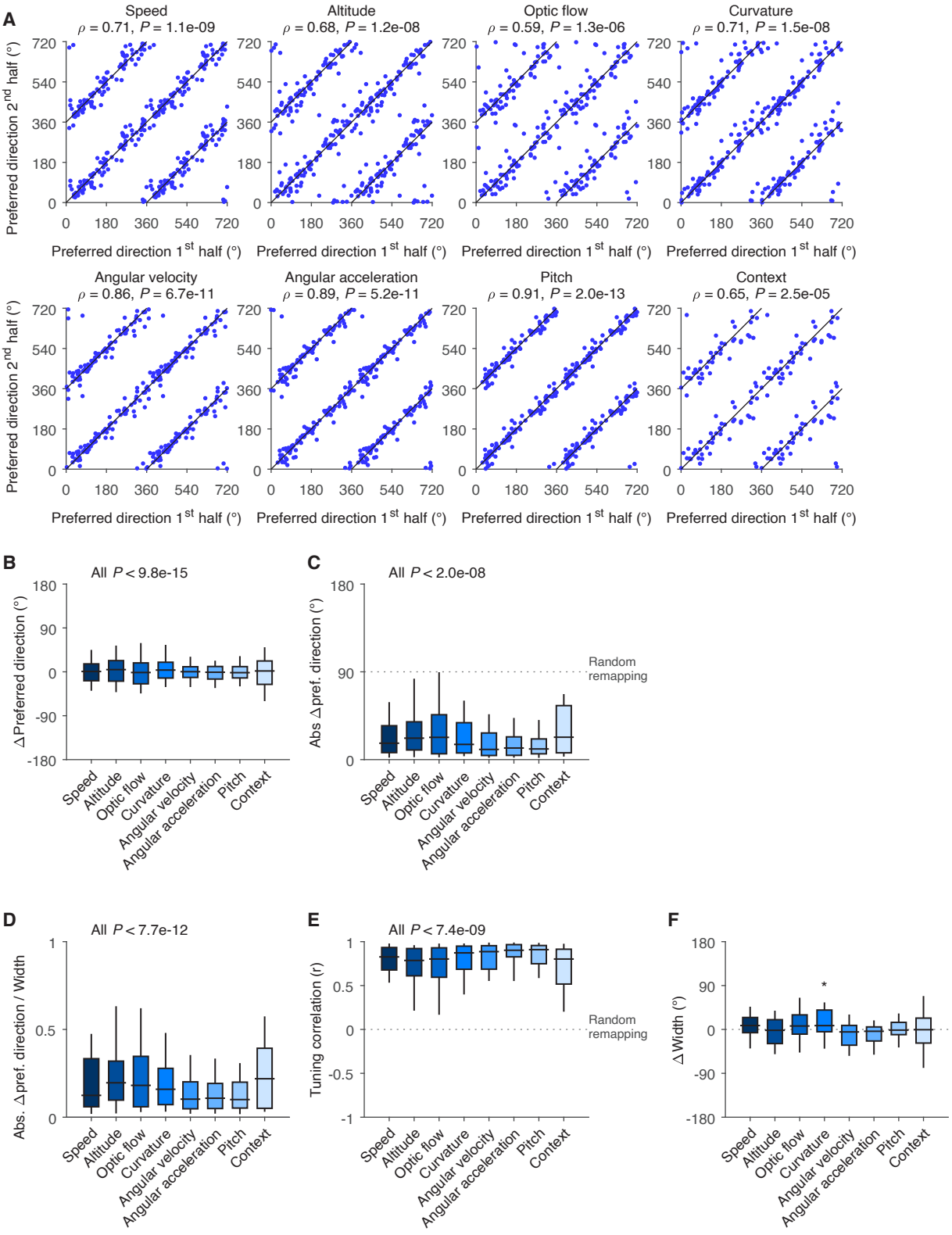

fig. S12: Non-spatial bisections. **(A)** Population scatter plots of the preferred direction of each neuron in the 2nd half vs. the preferred direction in the 1st half of the data, for eight non-spatial bisections. In each scatter, the data are plotted twice on each axis, from 0–360° and 360–720°, for display purposes; black lines are identity-lines. The 8 bisections are – from left to right, top to bottom: Speed (n = 87 cells), Altitude above mean sea-level (n = 85), Optic flow (n = 78), Radius of curvature (n = 81), Angular velocity (n = 82), Angular acceleration (n = 80), Pitch angle (n = 86) and Context (n = 47). Numbers of neurons in each bisection denote the head-direction cells that contained enough data in both halves of the bisection, and thus were valid for this analysis. Circular-circular correlation coefficients and P-values are indicated above each scatter plot. **(B-F)** Same as fig. S11B-F, for the 8 non-spatial bisections. In each panel, the P-values were computed as in fig. S11B-F, and were Bonferroni corrected for the number of tests (n = 8). We note that similar P-values were obtained when comparing to cell-shuffles. **(B)** Difference in preferred direction for each neuron between the 1st half and 2nd half of the bisection, plotted separately for each of the 8 non-spatial bisections. **(C)** Absolute difference in preferred direction. **(D)** Absolute difference in preferred direction, normalized by each cell's overall tuning width. **(E)** Tuning correlation (Pearson r) between the 1st half and 2nd half. **(F)** Differences in tuning width between the 1st half and 2nd half. In each boxplot, horizontal lines denote medians, boxes denote 25–75th percentiles, and whiskers denote 10–90th percentiles.

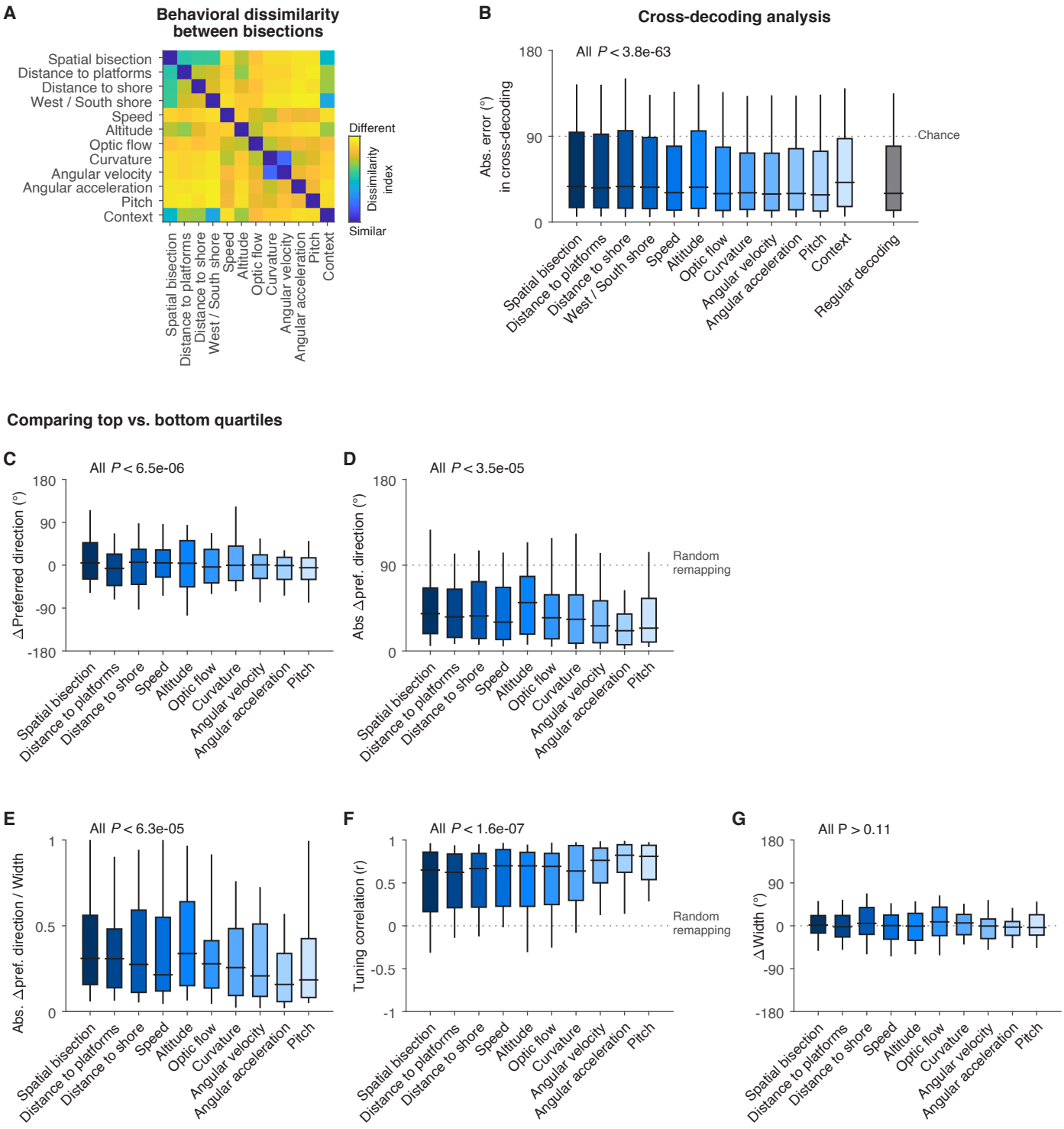

fig. S13: Controls for the bisections analysis. Figure legend on the next page

fig. S13: Controls for the bisections analysis. **(A)** Behavioral dissimilarity between bisections. Dissimilarity index between all pairs of bisections was defined as follows: $\min(Hamming(i,j), 1 - Hamming(i,j))$, where Hamming(i, j) is the Hamming distance (proportion of discordant pairs) between bisection i (a vector of zeros and ones corresponding to the allocation of each behavioral sample to one of the two halves of bisection i) and bisection j (similar vector for bisection j). This index ranges from 0 (the two bisections are identical: blue color) to 0.5 (the two bisections are maximally different from each other: yellow color). Most bisection pairs were very different from each other, with one notable exception (radius of curvature and angular velocity: note the blue color in this particular bin). **(B)** Cross-decoding analysis for all the 12 bisections (4 spatial bisections and 8 non-spatial bisections). We used a Bayesian decoder as in Fig. 2I-J, but trained it on one half of the data – defined separately for each of the bisections – and tested it using the other half (repeating for both halves: a two-fold cross-validation). We only used sessions and bisections where there were > 3 minutes of flight data in each condition (each half). Decoding errors were highly significantly smaller than chance (Wilcoxon sign-rank test: all P values < 3.8×10^{-63}, Bonferroni corrected [n = 12]). Absolute decoding errors using the regular decoder are plotted in gray for comparison. **(C-G)** Here we repeated the bisections analysis (Fig. 3C-D, fig. S11B-F), using the two extreme quartiles of the data (top 25% vs. bottom 25%) instead of halves. The results remain the same using this more conservative comparison. This analysis was applicable for 10 of the 12 bisections we tested – for which the relevant behavioral variable was continuous and not discrete (the remaining bisections were 'closer to West/South shore' and 'Context', which are binary categories). **(C)** Difference in preferred direction (Rayleigh test for uniformity: all P < 6.5×10^{-6}). **(D)** Absolute difference in preferred direction (Wilcoxon signed-rank test vs. 90°: all P < 3.5×10^{-5}). **(E)** Absolute difference in preferred direction, normalized by each cell's overall tuning width (Kolmogorov-Smirnov test for data vs. shuffles: all P < 6.3×10^{-5}). **(F)** Tuning correlation (Pearson r; Wilcoxon signed-rank test vs. 0: all P < 1.6×10^{-7}). **(G)** Difference in tuning width (Wilcoxon sign-rank test against 0°: all P > 0.11). All the P-values in **C**-**G** were Bonferroni corrected for the number of comparisons (n = 10); we note that similar P-values were obtained when comparing to cell-shuffles.

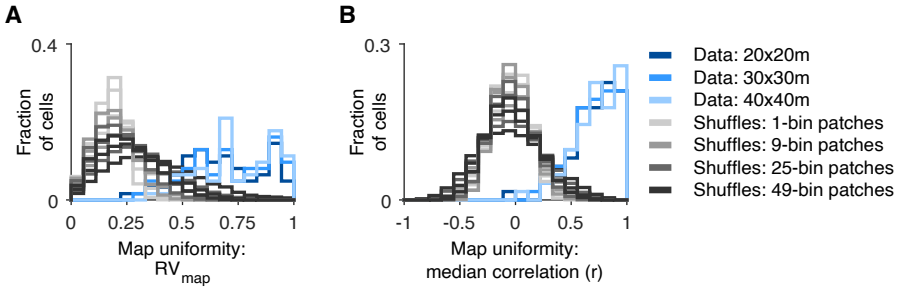

fig. S14: Spatial stability of head-direction cells was robust to shuffling procedures and bin size. (A-B) Cell-shuffling procedure for quantifying the spatial stability of head-direction tuning. Shown are histograms of **(A)** RV_{map} and **(B)** median correlation, same as in Fig. 3L-M. Here we modified the cell-shuffling procedure by randomly sampling patches of spatially neighboring bins from the same neuron, instead of the single-bin based shuffling used in Fig. 3L-M. We used four different patch sizes of 1, 9, 25 and 49 bins, with three spatial bin sizes (20×20-m, 30×30-m and 40×40-m) yielding 12 combinations, i.e. 12 shuffling distributions. This cell-shuffling represents a null hypothesis in which the directional tuning is stable within a certain spatial domain (regions in fig. S1, left). We used different patch-sizes to account for multiple possible sizes of these spatial domains. We obtained the following results – RV_{map}: 50–76% significant cells (compared to the 95th percentiles of *both* shuffles: spike shuffles and cell shuffles); median tuning correlation: 81–82% significant cells (again compared to *both* shuffles; range computed across the 12 combinations of bin-sizes × patch-sizes).

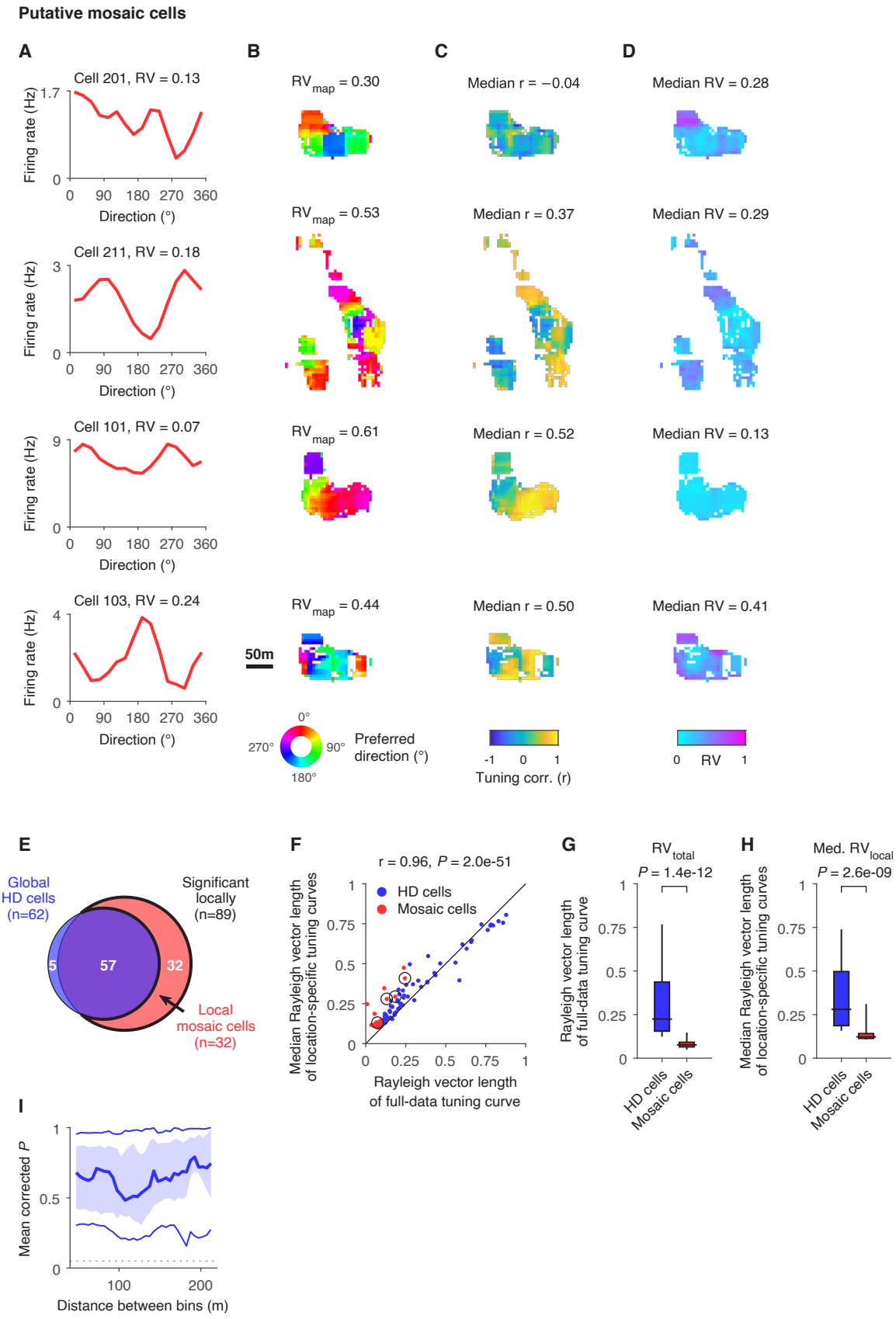

fig. S15: Searching for 'Mosaic' neurons. Figure legend on the next page

fig. S15: Searching for 'Mosaic' neurons. **(A-D)** Four putative 'mosaic cells' (rows), identified using the following criteria: significant local head-direction (HD) tuning, and no global HD tuning. Shown are (**A**) directional tuning curves, **(B)** preferred-direction maps, (**C**) tuning-correlation maps, and (**D**) tuning-sharpness maps. Indicated above each neuron are the global tuning sharpness index (RV, see **A**), local tuning sharpness index (median RV, see **D**), and the two spatial stability indices (RV_{map} and median tuning correlation [median *r*], see **B** and **C**). The scale bar (50 m) is common to all the maps of all these cells. **(E)** Venn diagram showing significant global HD cells (*n* = 62 cells, blue circle), cells with significant local tuning (*n* = 89 cells, red circle), and putative mosaic cells – neurons with local tuning but without global tuning (*n* = 32 cells, red crescent). There was no significant difference in cell classification between the two brain areas, presubiculum and retrosplenial cortex (χ^2 = 1.3, *P* = 0.52). **(F-H)** quantification of global and local tuning sharpness. **(F)** Local tuning sharpness (median RV of the local tuning curves: *y*-axis) vs. global tuning sharpness (RV of overall tuning curve: *x*-axis), for HD cells (blue) and mosaic cells (red). Black circles mark the four example cells plotted in **A-D**, which are among the cells with the strongest local tuning. **(G)** RV of overall tuning curve (*x*-axis of **F**) for the two cell populations: global HD cells (*n* = 62) and local mosaic cells (*n* = 32). **(H)** Same as **G**, for the local tuning sharpness (*y*-axis of **F**). HD cells showed sharper global and local tuning compared to mosaic cells (Wilcoxon rank-sum test; global tuning sharpness [panel **G**]: $P = 1.4\times10^{-12}$; local tuning sharpness [panel **H**]: $P = 2.6\times10^{-9}$). Horizontal lines in boxplots denote medians, boxes denote 25–75th percentiles, and whiskers denote 10–90th percentiles. **(I)** Results of a permutation test between pairs of spatial bins, plotted as a function of the distance between the bins. The purpose of this analysis is to test whether spatial bins of the same neuron show a significant difference in their local preferred-direction. Shown is the *P*-value (corrected for false discovery rate [FDR]) for the hypothesis that the difference in preferred direction between two spatial bins is larger than their inherent spiking variability. We only tested non-overlapping spatial bins (40×40-m), and averaged the *P*-values of each neuron across all bin-pairs with the same distance. Thick line denotes population median, shaded area denotes 25–75th percentiles, and thin lines denote 10–90th percentiles (only distances with ≥10 neurons are shown). The dashed line denotes the significance threshold of α=0.05. Note that there were no neurons, at any distance, which had a mean corrected *P*-value below the significance threshold of 5%; moreover, only 6% of the individual *P*-values were significant – which is only slightly above the false discovery rate of 5%. This suggests that there are no significant systematic changes in preferred direction across space.

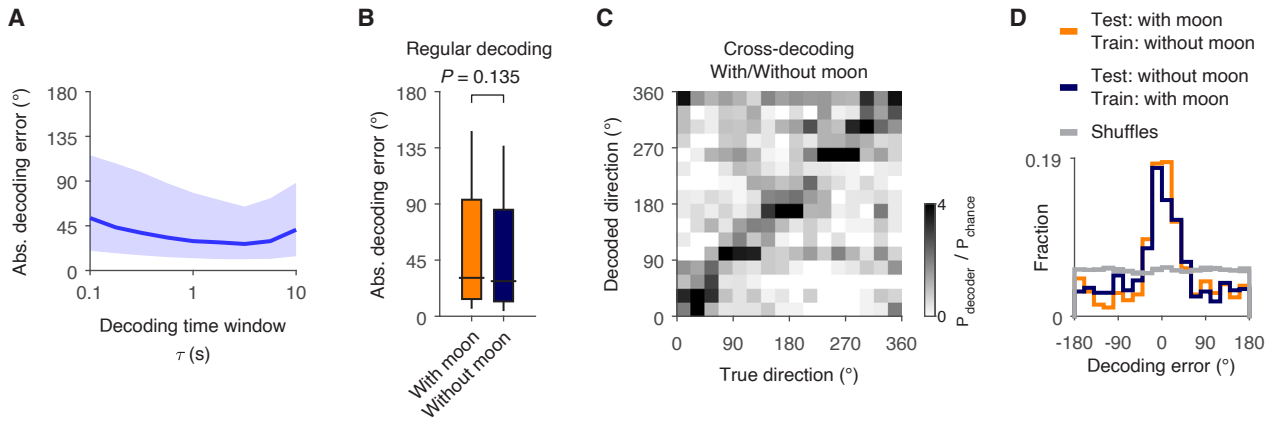

fig. S16: Decoding. **(A)** Absolute decoding error as a function of the decoding time-window τ (Methods; note the *x*-axis here is logarithmic). Blue line: median decoding error; shaded area: 25–75th percentiles. The decoding performance was robust to the choice of the time-window τ over a wide set of values; we used τ of 1-s in all the decoding analyses throughout this study. **(B-D)** No effect of the moon's presence on decoding accuracy. Data from 2 sessions which included enough time in both the 'with moon' and 'without moon' conditions, in addition to the other inclusion-criteria for decoding (Methods). **(B)** Absolute directional decoding error with-moon and without-moon (n = 1,245 decoding time windows). Decoding error was similar in both conditions (Wilcoxon signed-rank test on 20 pairs of independent cross-validation blocks: P = 0.135; Δmedian decoding error = 2.6°). Horizontal lines in boxplots denote medians, boxes denote 25–75th percentiles, whiskers denote 10–90th percentiles. **(C-D)** Cross-decoding analysis (similar to fig. S13B). The decoder was trained on the with-moon epochs and tested on the without-moon epochs, or vice versa. **(C)** Confusion matrix (pooled over sessions and the two conditions): Probability of decoded direction (*y*-axis) for each true direction (*x*-axis), normalized by the uniform chance probability $P_{chance} = 1/n_{bins}$ (see color-bar). **(D)** Histograms of cross-decoding errors, plotted separately for training with moon and testing without moon, or vice versa. Note the narrow distribution of the decoding errors in the data (Rayleigh test of uniformity for the two histograms: $P = 6.2\times10^{-53}$ and $P = 2.2\times10^{-48}$). Gray, cross-decoding using rigid spike-shuffles. Decoding errors were similar across conditions, suggesting that the head-direction code does not depend on moon condition. Median absolute cross-decoding error: with moon: 31° (orange), without moon: 38° (dark blue). Wilcoxon rank-sum test between the two test conditions (comparing the absolute errors): P = 0.29.

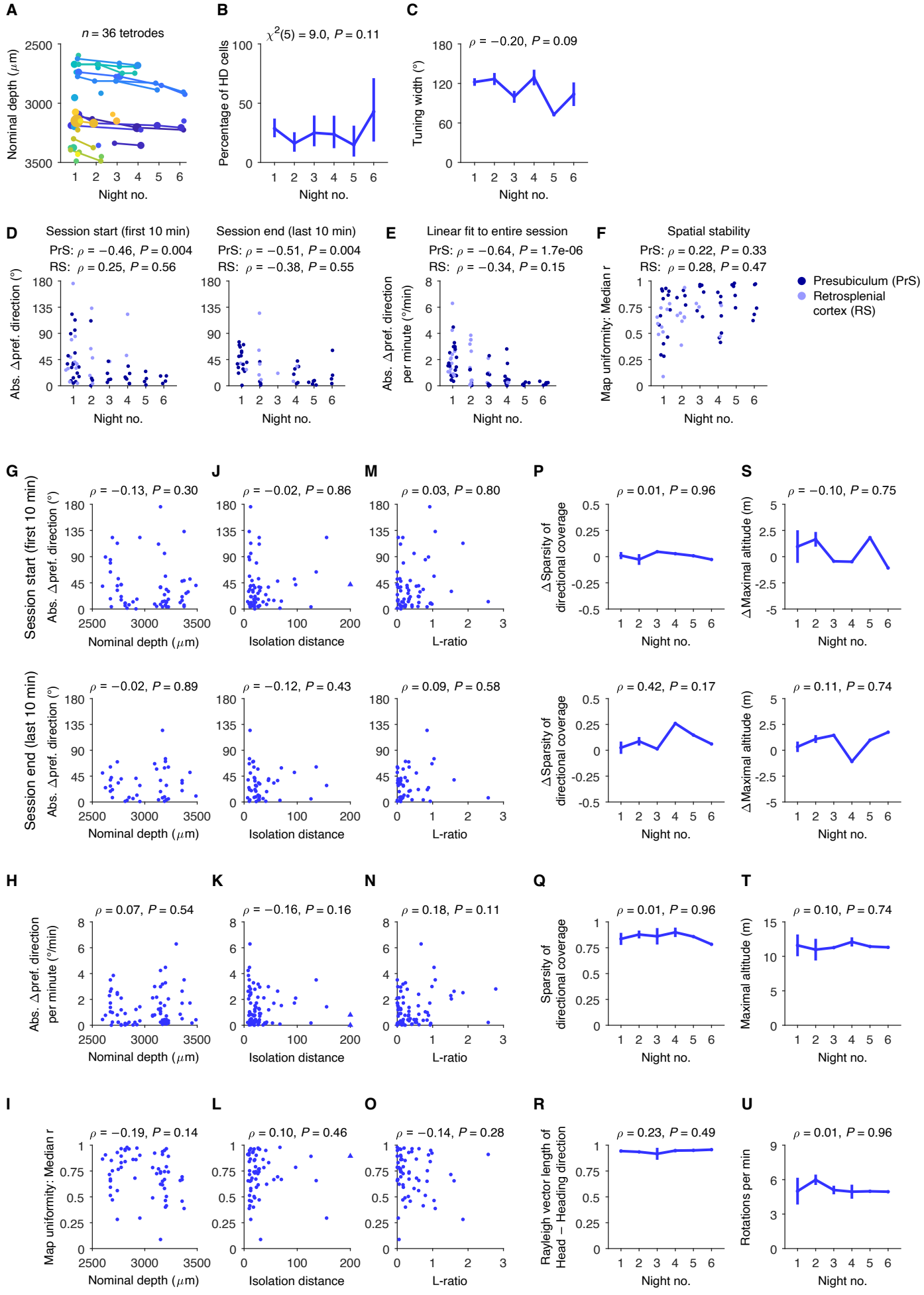

fig. S17: Dynamics of head-direction coding across nights: controls for brain region, spike-sorting quality, and behavior. Figure legend on the next page

fig. S17: Dynamics of head-direction coding across nights: controls for brain region, spike-sorting quality, and behavior. This figure shows several controls for the dynamics of head-direction tuning that were analyzed in Figure 5. **(A-I)** Anatomical controls. **(A)** Nominal recording depth of each tetrode on each night (depth relative to the brain surface). The data come from 36 individual tetrodes (colors), which were moved slowly between recording sessions on the island. Dot sizes represent the number of recorded head-direction cells on each tetrode (1–5 cells per night). The slow movement of the tetrodes (20 – 80 μm daily) allowed recording new neurons every night, but ensured that we did not move between different anatomical brain areas within the 6 nights of recordings. **(B)** Mean and confidence intervals for the percentage of head-direction cells (HD cells) across nights. For each night, we fitted a binomial distribution to the proportion of head-direction cells and calculated the 95% confidence interval. There was no significant difference in the proportion of head-direction cells across nights (Chi-squared test: χ^2 (5) = 9.0, *P* = 0.11) – again, suggesting that we did not move between anatomical brain areas. **(C)** Tuning width per neuron, plotted across nights (mean ± SEM). There was no correlation between tuning width and night number (ρ = –0.20, *P* = 0.09). **(D)** Left: absolute Δpreferred direction in the first 10 minutes vs. the night number (same as main Fig. 5C), plotted separately for neurons from presubiculum (PrS; *n* = 41 neurons, dark-blue) and neurons from retrosplenial cortex (RS; *n* = 21 neurons, light-blue). Right: same for the last 10 minutes (*n* = 35 and 10 neurons for PrS and RS, respectively). **(E)** Similar to **D**, for the slope of within-session linear fit to the preferred direction (Δpreferred direction per minute over the entire session, same as Fig. 5D; *n* = 49 and 28 neurons for PrS and RS, respectively). **(F)** Similar to **D**, for median tuning correlation (spatial stability, same as Fig. 5E; *n* = 40 and 20 neurons for PrS and RS, respectively). The trends in main Fig. 5C-E remained also when separating the two brain regions – although some of the correlations, especially in RS, were non-significant due to the lower number of neurons after the separation. **(G-I)** Scatter plots of neural dynamics vs. recording-depth. In each panel, the stability metrics which appear in main Fig. 5C-E (*y*-axis) are plotted against the neurons' recording-depth (*x*-axis). **(G)** Top panel: absolute change in preferred-direction of each neuron during the first 10 minutes of recording (same as main Fig. 5C-left) vs. its nominal recording depth. Bottom panel: same, for the last 10 minutes (same as Fig. 5C-right). There was no correlation between recording depth and neural dynamics (session start: ρ = –0.13, *P* = 0.30; session end: ρ = –0.02, *P* = 0.89). **(H)** Absolute Δpreferred direction per minute (as Fig. 5D) vs. recording-depth (ρ = 0.07, *P* = 0.54). **(I)** Median tuning correlation (spatial stability, as Fig. 5E) vs. recording-depth (ρ = –0.19, *P* = 0.14). Together, panels **A-I** suggest that the head-direction cells that we recorded came from similar brain regions across nights, without dramatic changes in recording-depth over nights, and that the observed neural dynamics across nights (Fig. 5) could not be explained by changes in anatomical properties across nights. **(J-O)** Controls for spike-sorting quality across nights. Shown are scatter plots of neural dynamics vs. two standard metrics for spike-sorting quality (*99*) – isolation distance (**J-L**) and L-ratio (**M-O**). **(J)** absolute change in preferred-direction of each neuron during the first 10 minutes of recording (top panel) or the last 10 minutes (bottom panel). Isolation distance did not correlate significantly with the neural dynamics (session start: ρ = –0.02, *P* = 0.86; session end: ρ = –0.12, *P* = 0.43). **(K)** Absolute Δpreferred direction per minute vs. isolation distance (ρ = –0.16, *P* = 0.16). **(L)** Median tuning correlation vs. isolation distance (ρ = 0.10, *P* = 0.46). The blue triangles in **J-L** denote neurons with isolation distance > 200 (plotted at 200 for display purposes only). **(M)** Same as **J**, for L-ratio (session start: ρ = 0.03, *P* = 0.80; session end: ρ = 0.09, *P* = 0.58). **(N)** Same as **K**, for L-ratio (ρ = 0.18, *P* = 0.11). **(O)** Same as **L**, for L-ratio (ρ = –0.14, *P* = 0.28). **(P-U)** Controls for differences in behavior across nights. Error bars, mean ± SEM. **(P)** Difference in sparsity of the directional coverage (ΔSparsity; difference between the first 5 minutes and the next 5 minutes), plotted across nights, for the session start (first 10 min, top panel) and session end (last 10 min, bottom panel). Sparsity is defined as: $sparsity = \frac{\langle T_i \rangle^2}{\langle T_i^2 \rangle}$, where T_i is the fraction of time-spent at each direction-bin. **(Q)** Sparsity of directional coverage for the entire session, plotted across nights. **(R)** Rayleigh vector length (RV) of head-direction minus heading-direction, plotted across nights (we included here all the night sessions with valid magnetometer measurements: *n* = 11 sessions). **(S)** Same as **P**, for the difference in the maximal altitude at which the bat flew. **(T)** Bat's maximal altitude in the entire session, plotted across nights. **(U)** Number of rotations per minute across nights (turning maneuvers are the main source of head-direction versus heading-direction mismatch in Egyptian fruit bats). Overall, panels **P-U** show that there was no systematic change in these four behavioral parameters (sparsity of directional coverage, maximal altitude, RV of head-direction minus heading-direction, and rotations per minute) as a function of the night-number – suggesting that changes in behavior across nights could *not* explain the neural dynamics observed in main Fig. 5 (directional coverage – session start: ρ = 0.01, *P* = 0.96; session end: ρ = 0.42, *P* = 0.17; entire session: ρ = 0.01, *P* = 0.96; maximal altitude – session start: ρ = –0.10, *P* = 0.75; session end: ρ = 0.11, *P* = 0.74; entire session: ρ = 0.10, *P* = 0.74; RV of head-direction minus heading-direction – ρ = 0.23, *P* = 0.49; rotations per minute – ρ = 0.01, *P* = 0.96).

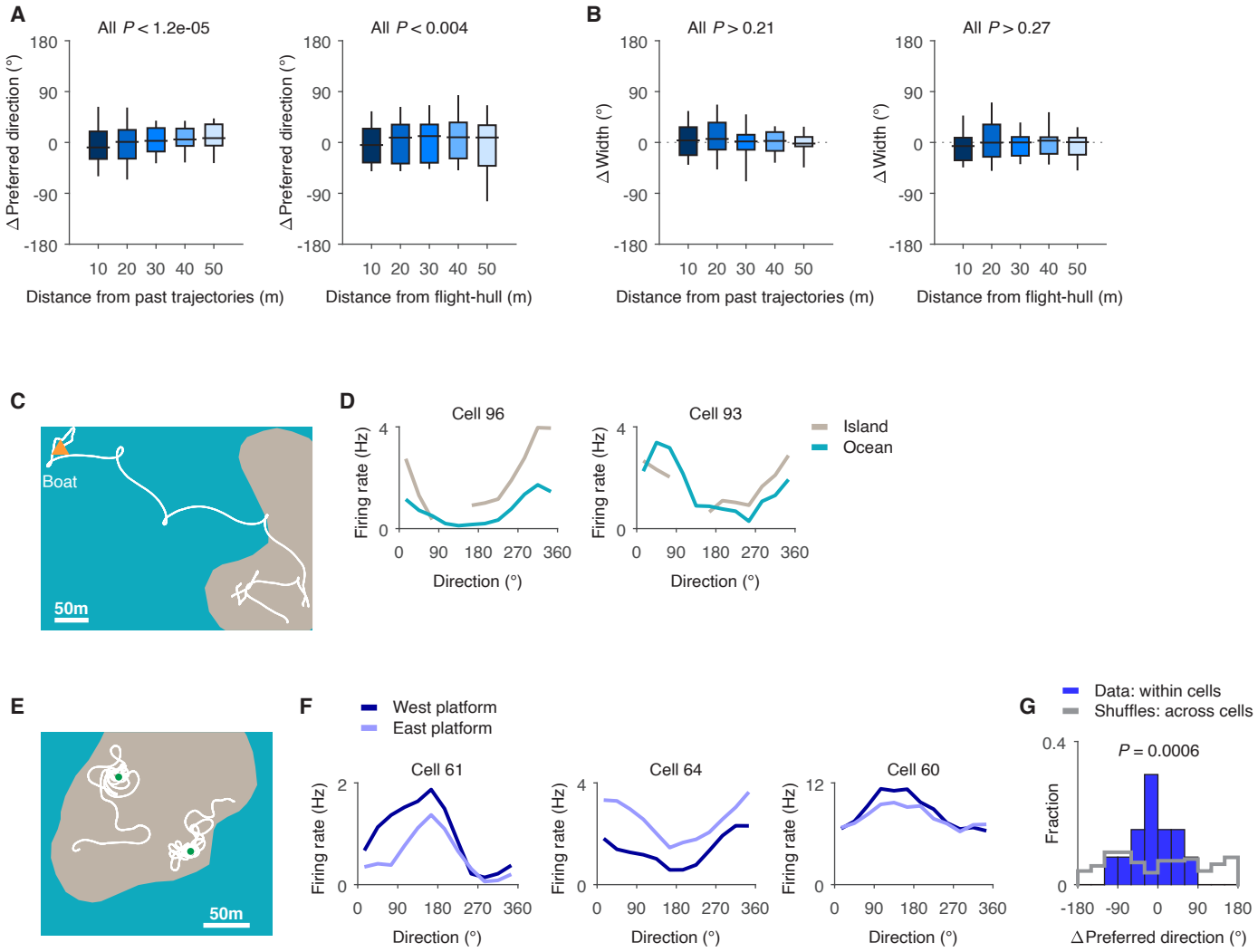

fig. S18: Head-direction tuning during novel trajectories. Figure legend on the next page

fig. S18: Head-direction tuning during novel trajectories. **(A-B)** Parametrization of bisections based on novel trajectories (Fig. 6), similar to the analysis in fig. S11G-H. Plotted are population boxplots of (**A**) preferred direction differences and (**B**) tuning-width differences, calculated by applying a series of fixed threshold (in meters) to the behavioral data (note that these are not strict bisections, as they did not divide the data into two equal parts). In both panels **A** and **B**, the left plot shows the distance from past trajectories (as in Fig. 6A-C) and the right plot shows the distance from the flight-hull (as in Fig. 6D-F). These plots show that the stability of the head-direction tuning was robust to the choice of thresholds, both for the distance from past trajectories (left panel in **A** and left panel in **B**) and for the distance from the behavioral flight-hull (right panel in **A** and right panel in **B**) – namely, even when comparing flights which were far from the bat's previous exploration history, there was no systematic difference in the preferred direction (**A**) or in the tuning width (**B**). **(A)** Preferred direction differences. Left panel: distance from past trajectories (Rayleigh test for uniformity: all $P < 1.2\times10^{-5}$). Right panel: distance from flight-hull (concave hull; Rayleigh test for uniformity: all $P < 0.004$). **(B)** Same as **A**, for tuning-width differences (left: Wilcoxon sign-rank test against 0°: all $P > 0.21$; right: all $P > 0.27$). All the *P*-values were Bonferroni corrected for the number of distance-bins ($n = 5$). We hypothesize that the stable directional tuning in locally-unfamiliar areas could be achieved by continuously updating the bat's cognitive map based on the nearby visible landmarks, or via path integration – integrating the bat's own motion. Such mechanisms can fill-in the directional information during short periods of flight over unfamiliar areas. **(C-D)** Analysis of neurons recorded during long trajectories above the sea. **(C)** One example trajectory of a bat flying above the sea (white), plotted over the island silhouette (gray) and the ocean (teal color). Orange triangle denotes the small boat which picked up the bat from the water surface and brought it back to the island. Scale bar, 50 m. **(D)** Two example neurons, with directional tuning-curves split by flying above land vs. above the ocean. This is not a strict bisection (the two parts are non-equal). These examples demonstrate that the head-direction tuning is maintained even in extreme situations when the bat flies with little visual landmarks, at night over the ocean. **(E-F)** Analysis of early sessions in bat 2. On the first 3 nights of this bat on the island, it only exhibited local flights around each platform – never flying between the two platforms. We therefore had to passively carry the bat between the two areas. **(E)** Trajectories of bat 2 in the first night outdoors (white), plotted over the island silhouette (gray). Green dots denote the two platforms, where the bat was released – and often landed. **(F)** Three example neurons, split by the flight's context – whether the bat started from one platform or the other. **(G)** Population histogram of the difference in preferred direction, for all the head-direction cells from the first 3 nights of bat no. 2 ($n = 13$ cells). The differences concentrated around 0° (Rayleigh test for uniformity: $P = 0.0006$), showing high stability between the two areas of the island – even though this bat never actively flew between these two platforms during the first 3 nights, and never connected the two areas. This anecdote contrasts with what was found in rodents, where active movement was crucial for stable head-direction tuning in two enclosures (*29*) – and it suggests that the bat likely used the shared landmarks between these two sub-regions, e.g. the landmarks visible from both sub-regions, thus creating a global representation of head-direction.

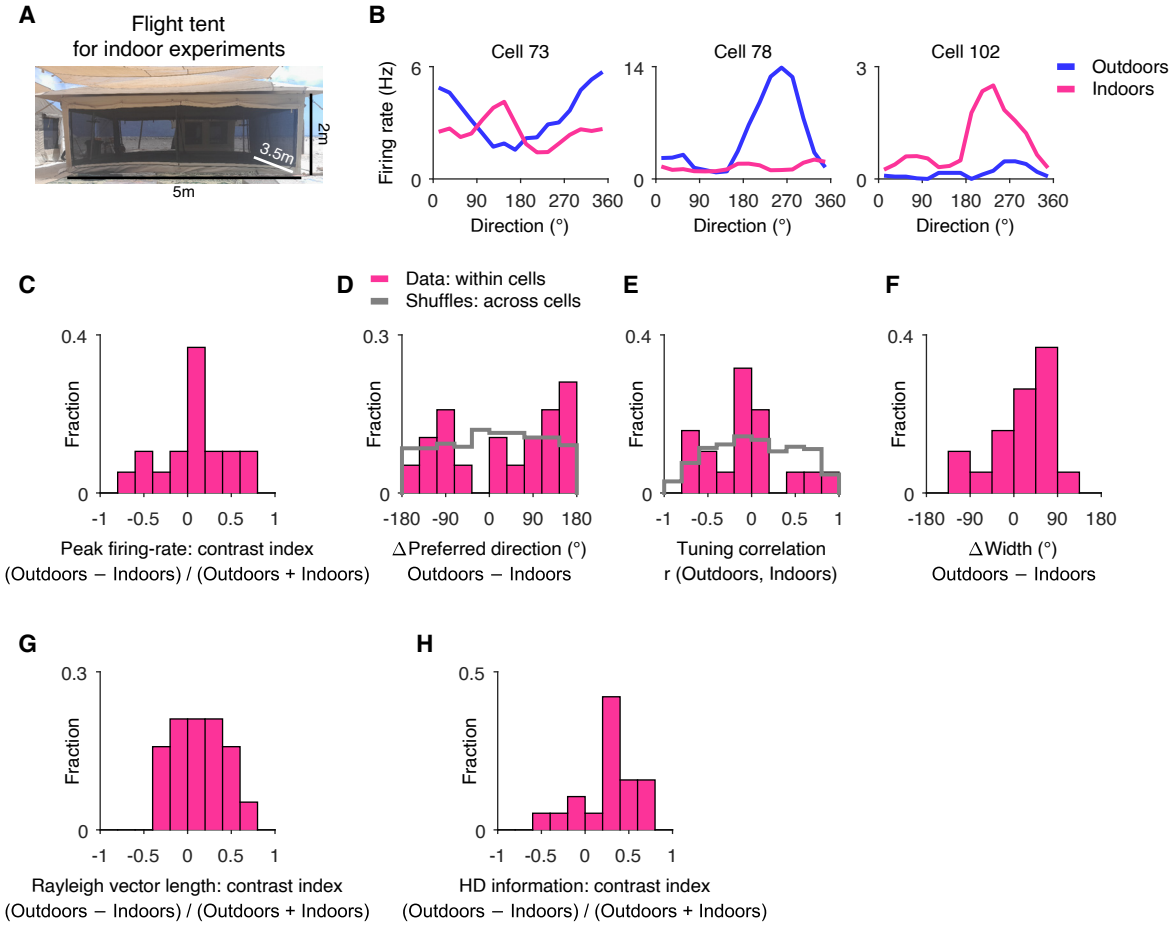

fig. S19: Random remapping between head-direction tuning during flight outdoors and flight indoors. **(A)** Photo of the flight tent, where the indoor sessions were conducted (size of tent: 5.0 × 3.5 m, height 2.0 m at the corners [higher at the center]). This tent contained two platforms at the corners, and several landmarks inside. **(B)** Three example neurons, showing directional tuning-curves for outdoor flight (blue) vs. indoor flight (pink). These neurons exhibited very different head-direction tuning curves indoors vs. outdoors, and sometimes even completely shut down in one of the conditions (two rightmost examples). **(C-F)** Population comparisons of indoor flight vs. outdoor flight (*n* = 19 cells, see Methods for inclusion criteria). **(C)** Histogram of peak firing-rate contrast index for outdoors vs. indoors ($\frac{\text{Outdoors} - \text{Indoors}}{\text{Outdoors} + \text{Indoors}}$). There was no significant systematic change in peak firing-rate at the population level (Wilcoxon sign-rank test vs. 0: $P = 0.26$). **(D)** Histogram of ΔPreferred direction (outdoors minus indoors), calculated for the data (pink: comparison within cells) and for cell-shuffles (gray: across cells). Differences in preferred-direction between outdoor and indoor flight in the real data were not significantly different from uniformity or from the cell-shuffles, indicating a random remapping between the two conditions (Rayleigh test for uniformity: $P = 0.38$; Kuiper's test, data vs. shuffles: $P = 0.42$). **(E)** Tuning correlation between the tuning-curves outdoors and indoors. Here again, differences in tuning were not significantly different from random remapping (Wilcoxon signed-rank test vs. 0: $P = 0.40$; Kolmogorov-Smirnov test, data vs. shuffles: $P = 0.30$). **(F)** Histogram of ΔWidth (outdoors minus indoors). No significant difference was found between outdoor and indoor flight (Wilcoxon signed-rank test vs. 0°: $P = 0.14$). Taken together, these results indicate that the recorded neurons did *not* exhibit stable tuning between indoor and outdoor flight, suggesting that bats did not have access to a global directional cue which existed in both conditions – e.g. a magnetic compass. **(G-H)** Contrast index of the tuning quality outdoors vs. indoors, using **(G)** Rayleigh vector length and **(H)** HD information; the contrast-index was calculated similar to **C**. HD information was significantly higher in outdoor vs. indoor flight (panel **H**: Wilcoxon signed-rank test vs. 0: $P = 0.009$), and a similar trend was evident using Rayleigh vector length (panel **G**: Wilcoxon signed-rank test vs. 0: $P = 0.077$).

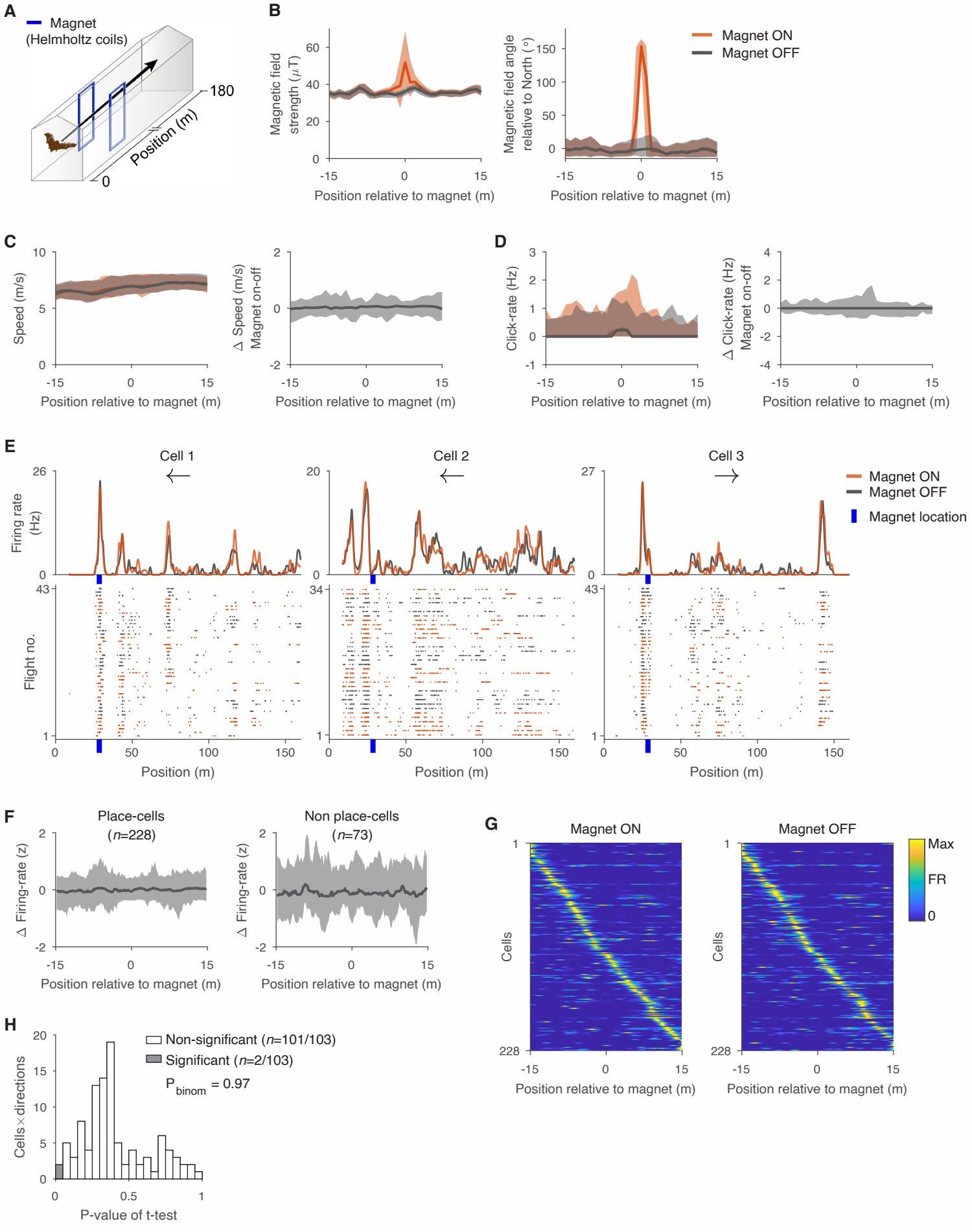

fig. S20: Lack of behavioral and neuronal responses to a magnetic-field perturbation in Egyptian fruit bats.
Figure legend on the next page

fig. S20: Lack of behavioral and neuronal responses to a magnetic-field perturbation in Egyptian fruit bats. Data from 2 bats, collected at the flight-tunnel at the Weizmann Institute. **(A)** Illustration of the setup: 180-m long flight-tunnel, with Helmholtz coils (blue) located 28.5 m from the tunnel entrance; schematic drawn not to scale. **(B)** Magnetic field as a function of position around the magnetic-coil location (1-m bins); the magnetic field was measured using the on-board magnetometer (which is part of the neural logger) – plotted here separately for magnet-on trials (orange) and magnet-off trials (black). Lines denote medians (n = 55 sessions × directions, from 2 bats), and shading denotes 10–90th percentiles. Left: Magnetic field strength (μT). Right: Magnetic field angle (°) relative to north (positive angle denotes clockwise rotation of the magnetic field). Note the spatially-localized changes in the magnetic field as the bat was flying through the magnet in the 'magnet on' trials. **(C-D)** No behavioral responses to the magnetic manipulation. Same colors as in **B**. **(C)** Left: Flight speed as a function of position around the magnetic-coil location. Right: Difference in flight speed between the magnet-on and magnet-off condition. **(D)** Same as **C**, for echolocation click-rate. There was no effect of the magnetic field on the bats' flight-speed or echolocation click-rate. **(E)** Examples of firing-rate maps and raster plots for three hippocampal CA1 place-cells (we analyzed separately the two flight directions). For each neuron × direction – Top: firing-rate maps calculated separately for magnet-on (orange) and magnet-off (gray); Bottom: raster plots of spike positions (x-axis) for different flights (y-axis); the position of the magnetic-coils is indicated as a blue vertical line below the x-axis. Arrows denote the flight direction. These cells did not show changes in their firing-rate around the magnet location for magnet-on vs. magnet-off trials – even though we chose here examples with prominent place-fields near the coils. **(F)** Neuronal population analysis. Z-scored difference in neuronal firing-rate between magnet-on and magnet-off trials as a function of position around the magnetic-coil location (0.2-m bins), for all the place-cells (left, n = 228 cells × directions) and non place-cells (right, n = 73 cells × directions). We included in this analysis all the cells × directions which emitted spikes in either the magnet-on or magnet-off conditions within a zone of ±15 meters around the Helmholtz coils, and which had ≥ 10 flights in this area in both magnet-on and magnet-off conditions (Methods). **(G)** Firing-rate maps for all the place cells (n = 228), plotted separately for magnet-on trials (left) and magnet-off trials (right) – normalized for each map by its peak firing-rate, and sorted based on the location of the maximal firing-rate in *all* flights (namely, the sorting is the same on the left and on the right). Note the similarity in the tuning curves in the population of place cells between the magnet-on and magnet-off conditions (compare left and right panels) – indicating lack of effect by the magnetic manipulation. FR, firing rate. **(H)** Statistical testing showing no effect of the magnetic manipulation on place-cell firing. Plotted is the distribution of P-values of a t-test between firing-rates of place cells in magnet-on vs. magnet-off trials (the firing-rate in each trial was computed inside a ±2-m area centered around the magnetic-coil); plotted separately for place-cells with non-significant difference (white; P-value ≥ 0.05; n = 101/103 cells × directions) and for place-cells with significant response to the change in the magnetic field (gray; P-value < 0.05; n = 2/103 cells × directions). We included in this analysis all the 103 cells × directions that were significant place cells and emitted spikes in either the magnet-on or magnet-off conditions within a zone of ±2 meters around the Helmholtz coils, and also had ≥ 10 passes in this area in both magnet-on and magnet-off conditions (Methods). Only 1.9% of the cells × directions were significant (n = 2/103), which is not greater than expected by chance at a significance threshold of α = 0.05 (Binomial test: P = 0.97). This argues that the tiny fraction of cells with differential responses to the magnetic field (2/103) do *not* constitute a genuine response to the magnetic manipulation.

References and Notes

1. R. Kays, M. C. Crofoot, W. Jetz, M. Wikelski, Terrestrial animal tracking as an eye on life and planet. *Science* **348**, aaa2478 (2015). doi:10.1126/science.aaa2478 Medline

2. H. G. Wallraff, *Avian Navigation: Pigeon Homing as a Paradigm* (Springer, 2005).

3. R. Wehner, *Desert Navigator: The Journey of an Ant* (Harvard Univ. Press, 2020).

4. A. Tsoar, R. Nathan, Y. Bartan, A. Vyssotski, G. Dell'Omo, N. Ulanovsky, Large-scale navigational map in a mammal. *Proc. Natl. Acad. Sci. U.S.A.* **108**, E718–E724 (2011). doi:10.1073/pnas.1107365108 Medline

5. A. Goldshtein, X. Chen, E. Amichai, A. Boonman, L. Harten, O. Yinon, Y. Orchan, R. Nathan, S. Toledo, I. D. Couzin, Y. Yovel, Acoustic cognitive map-based navigation in echolocating bats. *Science* **386**, 561–567 (2024). doi:10.1126/science.adn6269 Medline

6. O. Lindecke, A. Elksne, R. A. Holland, G. Pētersons, C. C. Voigt, Experienced migratory bats integrate the sun's position at dusk for navigation at night. *Curr. Biol.* **29**, 1369–1373.e3 (2019). doi:10.1016/j.cub.2019.03.002 Medline

7. S. Engels, N.-L. Schneider, N. Lefeldt, C. M. Hein, M. Zapka, A. Michalik, D. Elbers, A. Kittel, P. J. Hore, H. Mouritsen, Anthropogenic electromagnetic noise disrupts magnetic compass orientation in a migratory bird. *Nature* **509**, 353–356 (2014). doi:10.1038/nature13290 Medline

8. W. Wiltschko, R. Wiltschko, Magnetic compass of European robins. *Science* **176**, 62–64 (1972). doi:10.1126/science.176.4030.62 Medline

9. M. Zapka, D. Heyers, C. M. Hein, S. Engels, N.-L. Schneider, J. Hans, S. Weiler, D. Dreyer, D. Kishkinev, J. M. Wild, H. Mouritsen, Visual but not trigeminal mediation of magnetic compass information in a migratory bird. *Nature* **461**, 1274–1277 (2009). doi:10.1038/nature08528 Medline

10. J. O'Keefe, J. Dostrovsky, The hippocampus as a spatial map. Preliminary evidence from unit activity in the freely-moving rat. *Brain Res.* **34**, 171–175 (1971). doi:10.1016/0006-8993(71)90358-1 Medline

11. J. O'Keefe, Place units in the hippocampus of the freely moving rat. *Exp. Neurol.* **51**, 78–109 (1976). doi:10.1016/0014-4886(76)90055-8 Medline

12. M. Fyhn, S. Molden, M. P. Witter, E. I. Moser, M.-B. Moser, Spatial representation in the entorhinal cortex. *Science* **305**, 1258–1264 (2004). doi:10.1126/science.1099901 Medline

13. T. Hafting, M. Fyhn, S. Molden, M.-B. Moser, E. I. Moser, Microstructure of a spatial map in the entorhinal cortex. *Nature* **436**, 801–806 (2005). doi:10.1038/nature03721 Medline

14. J. B. Ranck Jr., "Head direction cells in the deep cell layer of dorsal presubiculum in freely moving rats" in *Electrical Activity of the Archicortex*, G. Buzsáki, C. H. Vanderwolf, Eds. (Akademiai Kiado, 1985), pp. 217–220.

15. J. S. Taube, R. U. Muller, J. B. Ranck Jr., Head-direction cells recorded from the postsubiculum in freely moving rats. I. Description and quantitative analysis. *J. Neurosci.* **10**, 420–435 (1990). doi:10.1523/JNEUROSCI.10-02-00420.1990 Medline

16. J. S. Taube, R. U. Muller, J. B. Ranck Jr., Head-direction cells recorded from the postsubiculum in freely moving rats. II. Effects of environmental manipulations. *J. Neurosci.* **10**, 436–447 (1990). doi:10.1523/JNEUROSCI.10-02-00436.1990 Medline

17. D. Yoganarasimha, X. Yu, J. J. Knierim, Head direction cell representations maintain internal coherence during conflicting proximal and distal cue rotations: Comparison with hippocampal place cells. *J. Neurosci.* **26**, 622–631 (2006). doi:10.1523/JNEUROSCI.3885-05.2006 Medline

18. M. P. Brandon, A. R. Bogaard, N. W. Schultheiss, M. E. Hasselmo, Segregation of cortical head direction cell assemblies on alternating theta cycles. *Nat. Neurosci.* **16**, 739–748 (2013). doi:10.1038/nn.3383 Medline

19. L. M. Giocomo, T. Stensola, T. Bonnevie, T. Van Cauter, M.-B. Moser, E. I. Moser, Topography of head direction cells in medial entorhinal cortex. *Curr. Biol.* **24**, 252–262 (2014). doi:10.1016/j.cub.2013.12.002 Medline

20. A. Peyrache, M. M. Lacroix, P. C. Petersen, G. Buzsáki, Internally organized mechanisms of the head direction sense. *Nat. Neurosci.* **18**, 569–575 (2015). doi:10.1038/nn.3968 Medline

21. D. E. Angelaki, J. Ng, A. M. Abrego, H. X. Cham, E. K. Asprodini, J. D. Dickman, J. Laurens, A gravity-based three-dimensional compass in the mouse brain. *Nat. Commun.* **11**, 1855 (2020). doi:10.1038/s41467-020-15566-5 Medline

22. A. Finkelstein, D. Derdikman, A. Rubin, J. N. Foerster, L. Las, N. Ulanovsky, Three-dimensional head-direction coding in the bat brain. *Nature* **517**, 159–164 (2015). doi:10.1038/nature14031 Medline

23. N. Ulanovsky, *Natural Neuroscience: Toward a Systems Neuroscience of Natural Behaviors* (MIT Press, 2025).

24. T. Wolbers, J. M. Wiener, Challenges for identifying the neural mechanisms that support spatial navigation: The impact of spatial scale. *Front. Hum. Neurosci.* **8**, 571 (2014). doi:10.3389/fnhum.2014.00571 Medline

25. J. S. Taube, The head direction signal: Origins and sensory-motor integration. *Annu. Rev. Neurosci.* **30**, 181–207 (2007). doi:10.1146/annurev.neuro.29.051605.112854 Medline

26. E. I. Moser, M.-B. Moser, B. L. McNaughton, Spatial representation in the hippocampal formation: A history. *Nat. Neurosci.* **20**, 1448–1464 (2017). doi:10.1038/nn.4653 Medline

27. M. B. Zugaro, A. Berthoz, S. I. Wiener, Background, but not foreground, spatial cues are taken as references for head direction responses by rat anterodorsal thalamus neurons. *J. Neurosci.* **21**, RC154 (2001). doi:10.1523/JNEUROSCI.21-14-j0001.2001 Medline

28. J. P. Goodridge, J. S. Taube, Preferential use of the landmark navigational system by head direction cells in rats. *Behav. Neurosci.* **109**, 49–61 (1995). doi:10.1037/0735-7044.109.1.49 Medline

29. R. W. Stackman, E. J. Golob, J. P. Bassett, J. S. Taube, Passive transport disrupts directional path integration by rat head direction cells. *J. Neurophysiol.* **90**, 2862–2874 (2003). doi:10.1152/jn.00346.2003 Medline

30. P. A. Dudchenko, L. E. Zinyuk, The formation of cognitive maps of adjacent environments: Evidence from the head direction cell system. *Behav. Neurosci.* **119**, 1511–1523 (2005). doi:10.1037/0735-7044.119.6.1511 Medline

31. J. S. Taube, H. L. Burton, Head direction cell activity monitored in a novel environment and during a cue conflict situation. *J. Neurophysiol.* **74**, 1953–1971 (1995). doi:10.1152/jn.1995.74.5.1953 Medline

32. R. M. Yoder, B. J. Clark, J. E. Brown, M. V. Lamia, S. Valerio, M. E. Shinder, J. S. Taube, Both visual and idiothetic cues contribute to head direction cell stability during navigation along complex routes. *J. Neurophysiol.* **105**, 2989–3001 (2011). doi:10.1152/jn.01041.2010 Medline

33. A. E. Smith, E. R. Wood, P. A. Dudchenko, The stimulus control of local enclosures and barriers over head direction and place cell spatial firing. *Brain Behav.* **11**, e02070 (2021). doi:10.1002/brb3.2070 Medline

34. K. J. Jeffery, The mosaic structure of the mammalian cognitive map. *Learn. Behav.* **52**, 19–34 (2024). doi:10.3758/s13420-023-00618-9 Medline

35. T. W. Cronin, S. Johnsen, N. J. Marshall, E. J. Warrant, "Visual orientation and navigation" in *Visual Ecology* (Princeton Univ. Press, 2014), pp. 289–312.

36. J. L. Gould, Sensory bases of navigation. *Curr. Biol.* **8**, R731–R738 (1998). doi:10.1016/S0960-9822(98)70461-0 Medline

37. A. Rozhok, *Orientation and Navigation in Vertebrates* (Springer, 2008).

38. B. el Jundi, E. J. Warrant, M. J. Byrne, L. Khaldy, E. Baird, J. Smolka, M. Dacke, Neural coding underlying the cue preference for celestial orientation. *Proc. Natl. Acad. Sci. U.S.A.* **112**, 11395–11400 (2015). doi:10.1073/pnas.1501272112 Medline

39. H. Mouritsen, Long-distance navigation and magnetoreception in migratory animals. *Nature* **558**, 50–59 (2018). doi:10.1038/s41586-018-0176-1 Medline

40. J. E. Huth, *The Lost Art of Finding Our Way* (Harvard Univ. Press, 2013).

41. D. Dreyer, A. Adden, H. Chen, B. Frost, H. Mouritsen, J. Xu, K. Green, M. Whitehouse, J. Chahl, J. Wallace, G. Hu, J. Foster, S. Heinze, E. Warrant, Bogong moths use a stellar compass for long-distance navigation at night. *Nature* **643**, 994–1000 (2025). doi:10.1038/s41586-025-09135-3 Medline

42. Materials and methods are available as supplementary materials.

43. P. A. LaChance, M. E. Hasselmo, Distinct codes for environment structure and symmetry in postrhinal and retrosplenial cortices. *Nat. Commun.* **15**, 8025 (2024). doi:10.1038/s41467-024-52315-4 Medline

44. A. S. Alexander, L. C. Carstensen, J. R. Hinman, F. Raudies, G. W. Chapman, M. E. Hasselmo, Egocentric boundary vector tuning of the retrosplenial cortex. *Sci. Adv.* **6**, eaaz2322 (2020). doi:10.1126/sciadv.aaz2322 Medline

45. P.-Y. Jacob, G. Casali, L. Spieser, H. Page, D. Overington, K. Jeffery, An independent, landmark-dominated head-direction signal in dysgranular retrosplenial cortex. *Nat. Neurosci.* **20**, 173–175 (2017). doi:10.1038/nn.4465 Medline

46. C. N. Boccara, F. Sargolini, V. H. Thoresen, T. Solstad, M. P. Witter, E. I. Moser, M.-B. Moser, Grid cells in pre- and parasubiculum. *Nat. Neurosci.* **13**, 987–994 (2010). doi:10.1038/nn.2602 Medline

47. R. Chaudhuri, B. Gerçek, B. Pandey, A. Peyrache, I. Fiete, The intrinsic attractor manifold and population dynamics of a canonical cognitive circuit across waking and sleep. *Nat. Neurosci.* **22**, 1512–1520 (2019). doi:10.1038/s41593-019-0460-x Medline

48. A. Rubin, L. Sheintuch, N. Brande-Eilat, O. Pinchasof, Y. Rechavi, N. Geva, Y. Ziv, Revealing neural correlates of behavior without behavioral measurements. *Nat. Commun.* **10**, 4745 (2019). doi:10.1038/s41467-019-12724-2 Medline

49. Z. Ajabi, A. T. Keinath, X.-X. Wei, M. P. Brandon, Population dynamics of head-direction neurons during drift and reorientation. *Nature* **615**, 892–899 (2023). doi:10.1038/s41586-023-05813-2 Medline

50. J. D. Seelig, V. Jayaraman, Neural dynamics for landmark orientation and angular path integration. *Nature* **521**, 186–191 (2015). doi:10.1038/nature14446 Medline

51. A. Rubin, M. M. Yartsev, N. Ulanovsky, Encoding of head direction by hippocampal place cells in bats. *J. Neurosci.* **34**, 1067–1080 (2014). doi:10.1523/JNEUROSCI.5393-12.2014 Medline

52. S. Danilovich, Y. Yovel, Integrating vision and echolocation for navigation and perception in bats. *Sci. Adv.* **5**, eaaw6503 (2019). doi:10.1126/sciadv.aaw6503 Medline

53. G. G. Kwiecinski, T. A. Griffiths, Rousettus egyptiacus. *Mamm. Species* **199**, 1–9 (1999). doi:10.2307/3504411

54. L. Las, N. Ulanovsky, Bats. *Nat. Methods* **21**, 1135–1137 (2024). doi:10.1038/s41592-024-02330-6 Medline

55. S. B. Childs, E. R. Buchler, Perception of simulated stars by *Eptesicus fuscus* (Vespertilionidae): A potential navigational mechanism. *Anim. Behav.* **29**, 1028–1035 (1981). doi:10.1016/S0003-3472(81)80056-5

56. H. Mouritsen, O. N. Larsen, Migrating songbirds tested in computer-controlled Emlen funnels use stellar cues for a time-independent compass. *J. Exp. Biol.* **204**, 3855–3865 (2001). doi:10.1242/jeb.204.22.3855 Medline

57. M. Dacke, E. Baird, M. Byrne, C. H. Scholtz, E. J. Warrant, Dung beetles use the Milky Way for orientation. *Curr. Biol.* **23**, 298–300 (2013). doi:10.1016/j.cub.2012.12.034 Medline

58. F. Raudies, M. P. Brandon, G. W. Chapman, M. E. Hasselmo, Head direction is coded more strongly than movement direction in a population of entorhinal neurons. *Brain Res.* **1621**, 355–367 (2015). doi:10.1016/j.brainres.2014.10.053 Medline

59. Y. Yovel, M. Geva-Sagiv, N. Ulanovsky, Click-based echolocation in bats: Not so primitive after all. *J. Comp. Physiol. A Neuroethol. Sens. Neural Behav. Physiol.* **197**, 515–530 (2011). doi:10.1007/s00359-011-0639-4 Medline

60. A. S. Etienne, K. J. Jeffery, Path integration in mammals. *Hippocampus* **14**, 180–192 (2004). doi:10.1002/hipo.10173 Medline

61. A. Cheung, S. Zhang, C. Stricker, M. V. Srinivasan, Animal navigation: The difficulty of moving in a straight line. *Biol. Cybern.* **97**, 47–61 (2007). doi:10.1007/s00422-007-0158-0 Medline

62. M. Geva-Sagiv, L. Las, Y. Yovel, N. Ulanovsky, Spatial cognition in bats and rats: From sensory acquisition to multiscale maps and navigation. *Nat. Rev. Neurosci.* **16**, 94–108 (2015). doi:10.1038/nrn3888 Medline

63. M. R. Loewen, "Laboratory measurements of the sound generated by breaking waves," thesis, Massachusetts Institute of Technology and Woods Hole Oceanographic Institution (1991).

64. G. Koay, R. S. Heffner, H. E. Heffner, Hearing in a megachiropteran fruit bat (*Rousettus aegyptiacus*). *J. Comp. Psychol.* **112**, 371–382 (1998). doi:10.1037/0735-7036.112.4.371 Medline

65. J. Zeil, Visual navigation: Properties, acquisition and use of views. *J. Comp. Physiol. A Neuroethol. Sens. Neural Behav. Physiol.* **209**, 499–514 (2023). doi:10.1007/s00359-022-01599-2 Medline

66. K. Asumbisa, A. Peyrache, S. Trenholm, Flexible cue anchoring strategies enable stable head direction coding in both sighted and blind animals. *Nat. Commun.* **13**, 5483 (2022). doi:10.1038/s41467-022-33204-0 Medline

67. J. P. Goodridge, P. A. Dudchenko, K. A. Worboys, E. J. Golob, J. S. Taube, Cue control and head direction cells. *Behav. Neurosci.* **112**, 749–761 (1998). doi:10.1037/0735-7044.112.4.749 Medline

68. R. S. Heffner, G. Koay, H. E. Heffner, Sound localization in an Old-World fruit bat (*Rousettus aegyptiacus*): Acuity, use of binaural cues, and relationship to vision. *J. Comp. Psychol.* **113**, 297–306 (1999). doi:10.1037/0735-7036.113.3.297 Medline

69. A. Bicanski, N. Burgess, Environmental anchoring of head direction in a computational model of retrosplenial cortex. *J. Neurosci.* **36**, 11601–11618 (2016). doi:10.1523/JNEUROSCI.0516-16.2016 Medline

70. Y. Yan, N. Burgess, A. Bicanski, A model of head direction and landmark coding in complex environments. *PLOS Comput. Biol.* **17**, e1009434 (2021). doi:10.1371/journal.pcbi.1009434 Medline

71. J. J. Knierim, H. S. Kudrimoti, B. L. McNaughton, Place cells, head direction cells, and the learning of landmark stability. *J. Neurosci.* **15**, 1648–1659 (1995). doi:10.1523/JNEUROSCI.15-03-01648.1995 Medline

72. R. Knight, C. E. Piette, H. Page, D. Walters, E. Marozzi, M. Nardini, S. Stringer, K. J. Jeffery, Weighted cue integration in the rodent head direction system. *Philos. Trans. R. Soc. London Ser. B* **369**, 20120512 (2013). doi:10.1098/rstb.2012.0512 Medline

73. R. Eilam-Altstädter, L. Las, M. P. Witter, N. Ulanovsky, *Stereotaxic Brain Atlas of the Egyptian Fruit Bat* (Academic Press, 2021).

74. S. Palgi, S. Ray, S. R. Maimon, Y. Waserman, L. Ben-Ari, T. Eliav, A. Tuval, C. Cohen, J. D. Keyyu, A. I. Ali, H. Mouritsen, L. Las, N. Ulanovsky, Data for: Head-direction cells

as a neural compass in bats navigating outdoors on a remote oceanic island, Zenodo (2025); https://doi.org/10.5281/zenodo.15646845.

75. K. Shoemake, Animating rotation with quaternion curves. *Comput. Graph. (ACM)* **19**, 245–254 (1985). doi:10.1145/325165.325242

76. NOAA-NCEI Geomagnetic Modeling Team, British Geological Survey, World Magnetic Model 2020 (2019); https://doi.org/10.25921/11v3-da71.

77. D. Koblick, Lunar azimuth and altitude estimation algorithm, MATLAB Central File Exchange (2010); https://www.mathworks.com/matlabcentral/fileexchange/22992-lunar-azimuth-and-altitude-estimation-algorithm.

78. A. Sarel, S. Palgi, D. Blum, J. Aljadeff, L. Las, N. Ulanovsky, Natural switches in behaviour rapidly modulate hippocampal coding. *Nature* **609**, 119–127 (2022). doi:10.1038/s41586-022-05112-2 Medline

79. T. Eliav, S. R. Maimon, J. Aljadeff, M. Tsodyks, G. Ginosar, L. Las, N. Ulanovsky, Multiscale representation of very large environments in the hippocampus of flying bats. *Science* **372**, eabg4020 (2021). doi:10.1126/science.abg4020 Medline

80. J. Voigts, J. P. Newman, M. A. Wilson, M. T. Harnett, An easy-to-assemble, robust, and lightweight drive implant for chronic tetrode recordings in freely moving animals. *J. Neural Eng.* **17**, 026044 (2020). doi:10.1088/1741-2552/ab77f9 Medline

81. A. Tuval, L. Las, Y. Shilo-Benjamini, Evaluation of injectable anaesthesia with five medetomidine-midazolam based combinations in Egyptian fruit bats (*Rousettus aegyptiacus*). *Lab. Anim.* **52**, 515–525 (2018). doi:10.1177/0023677218756456 Medline

82. A. Sarel, A. Finkelstein, L. Las, N. Ulanovsky, Vectorial representation of spatial goals in the hippocampus of bats. *Science* **355**, 176–180 (2017). doi:10.1126/science.aak9589 Medline

83. K. Zhang, Representation of spatial orientation by the intrinsic dynamics of the head-direction cell ensemble: A theory. *J. Neurosci.* **16**, 2112–2126 (1996). doi:10.1523/JNEUROSCI.16-06-02112.1996 Medline

84. J. H. Zar, *Biostatistical Analysis* (Prentice Hall, ed. 4, 1999).

85. R. Kempter, C. Leibold, G. Buzsáki, K. Diba, R. Schmidt, Quantifying circular-linear associations: Hippocampal phase precession. *J. Neurosci. Methods* **207**, 113–124 (2012). doi:10.1016/j.jneumeth.2012.03.007 Medline

86. K. Zhang, I. Ginzburg, B. L. McNaughton, T. J. Sejnowski, Interpreting neuronal population activity by reconstruction: Unified framework with application to hippocampal place cells. *J. Neurophysiol.* **79**, 1017–1044 (1998). doi:10.1152/jn.1998.79.2.1017 Medline

87. A. Johnson, K. Seeland, A. D. Redish, Reconstruction of the postsubiculum head direction signal from neural ensembles. *Hippocampus* **15**, 86–96 (2005). doi:10.1002/hipo.20033 Medline

88. L. McInnes, J. Healy, J. Melville, UMAP: Uniform manifold approximation and projection for dimension reduction. arXiv:1802.03426v3 [stat.ML] (2018).

89. S. Schwarze, N.-L. Schneider, T. Reichl, D. Dreyer, N. Lefeldt, S. Engels, N. Baker, P. J. Hore, H. Mouritsen, Weak broadband electromagnetic fields are more disruptive to magnetic compass orientation in a night-migratory songbird (*Erithacus rubecula*) than strong narrow-band fields. *Front. Behav. Neurosci.* **10**, 55 (2016). doi:10.3389/fnbeh.2016.00055 Medline

90. P. Berens, CircStat: A MATLAB toolbox for circular statistics. *J. Stat. Softw.* **31**, 1–21 (2009). doi:10.18637/jss.v031.i10

91. M. Zugaro, FMAToolbox (2012); https://fmatoolbox.sourceforge.net/.

92. Y. Benjamini, Y. Hochberg, Controlling the false discovery rate: A practical and powerful approach to multiple testing. *J. R. Stat. Soc. Series B Stat. Methodol.* **57**, 289–300 (1995). doi:10.1111/j.2517-6161.1995.tb02031.x

93. K. M. Gothard, W. E. Skaggs, B. L. McNaughton, Dynamics of mismatch correction in the hippocampal ensemble code for space: Interaction between path integration and environmental cues. *J. Neurosci.* **16**, 8027–8040 (1996). doi:10.1523/JNEUROSCI.16-24-08027.1996 Medline

94. I. Lee, D. Yoganarasimha, G. Rao, J. J. Knierim, Comparison of population coherence of place cells in hippocampal subfields CA1 and CA3. *Nature* **430**, 456–459 (2004). doi:10.1038/nature02739 Medline

95. J. Shin, H.-W. Lee, S.-W. Jin, I. Lee, Subtle visual change in a virtual environment induces heterogeneous remapping systematically in CA1, but not CA3. *Cell Rep.* **41**, 111823 (2022). doi:10.1016/j.celrep.2022.111823 Medline

96. S. Leutgeb, J. K. Leutgeb, C. A. Barnes, E. I. Moser, B. L. McNaughton, M.-B. Moser, Independent codes for spatial and episodic memory in hippocampal neuronal ensembles. *Science* **309**, 619–623 (2005). doi:10.1126/science.1114037 Medline

97. A. M. Eskicioglu, P. S. Fisher, Image quality measures and their performance. *IEEE Trans. Commun.* **43**, 2959–2965 (1995). doi:10.1109/26.477498

98. H. Bay, A. Ess, T. Tuytelaars, L. Van Gool, Speeded-up robust features (SURF). *Comput. Vis. Image Underst.* **110**, 346–359 (2008). doi:10.1016/j.cviu.2007.09.014

99. N. Schmitzer-Torbert, J. Jackson, D. Henze, K. Harris, A. D. Redish, Quantitative measures of cluster quality for use in extracellular recordings. *Neuroscience* **131**, 1–11 (2005). doi:10.1016/j.neuroscience.2004.09.066 Medline